UNIVERSITY OF SOUTHAMPTON

FACULTY OF NATURAL AND ENVIRONMENTAL SCIENCES

Chemistry

Optimised Detectors for Integration of NMR with Microfluidic Devices

by

Graeme R. Finch

Thesis for the degree of Doctor of Philosophy

February 2017

UNIVERSITY OF SOUTHAMPTON

ABSTRACT

FACULTY OF NATURAL AND ENVIRONMENTAL SCIENCES

Chemistry

Doctor of Philosophy

OPTIMISED DETECTORS FOR INTEGRATION OF NMR WITH MICROFLUIDIC DEVICES

by Graeme R. Finch

An optimised nuclear magnetic resonance (NMR) detector design has been developed to allow in situ NMR observation of sub mM concentrations of sample within a 2 μl sample volume on a microfluidic chip.

The detector is a new design of double micro-stripline detector that is compatible with functional lab-on-a-chip devices. The design has been optimised using finite element analysis taking into account both the shape of the sample chamber and the resonator.

The sensitivity of this detector compares favourably with other micro-NMR systems. The ability to observe low concentrations allows direct analysis of cell metabolomics on a chip within 20 minutes of experiment time.

The detector has been adapted to resonate at 2 frequencies. This opens the possibility of heteronuclear NMR experiments without compromising the sensitivity of the probe. The sensitivity is sufficient to demonstrate the ability to study changes in the structure of proteins when binding to a substrate.

Also explored in this work is another detector design the inductively coupled planar microcoil. Finite element analysis has allowed accurate simulation of these microcoils.

Contents

List of Figures

List of Tables

Declaration of Authorship

I, Graeme R. Finch , declare that the thesis entitled *Optimised Detectors for Integration of NMR with Microfluidic Devices* and the work presented in the thesis are both my own, and have been generated by me as the result of my own original research. I confirm that:

- this work was done wholly or mainly while in candidature for a research degree at this University;
- where any part of this thesis has previously been submitted for a degree or any other qualification at this University or any other institution, this has been clearly stated;
- where I have consulted the published work of others, this is always clearly attributed;
- where I have quoted from the work of others, the source is always given. With the exception of such quotations, this thesis is entirely my own work;
- I have acknowledged all main sources of help;
- where the thesis is based on work done by myself jointly with others, I have made clear exactly what was done by others and what I have contributed myself;
- parts of this work have been published as:[10]

Signed:.....

Date:.....

Acknowledgements

I would like to express my special appreciation to my supervisor Professor Marcel Utz. For your advice and knowledge that have helped me grow personally and academically through this time. For your encouragement in taking me as a chemistry student through the technicalities of building NMR probes.

I would like to thank the University of Southampton and the iMR CDT for funding this opportunity, without which I would not have been able to undertake it. Thanks as well to the iMR CDT for providing a background to other areas of magnetic resonance.

I would like to thank my secondary supervisor and Masters project supervisor Professor Malcolm Levitt. For inspiring an enthusiasm for NMR as an undergraduate and encouraging me to take on a PhD.

Thanks of course to my research group. To Dr Ali Yilmaz and Cara Vallance who have helped me with the experimental work that has made this thesis possible, especially with their work on microfluidic chips and cell culture respectively. Also to Dr Ali Smith, Herb Ryan, Stuart Elliott, and Billy Hale.

Thanks to the members of the magnetic resonance department who started their PhD at the same time as me and have been on this journey with me. Dr Gabriele Stevanato, Dr Richard Bounds and Zenawi Welderufael.

And of course a special thanks to my friends, family and girlfriend who have supported me along the way.

Chapter 1

Introduction

1.1 Goal

The aim of this work is to develop optimised Nuclear magnetic resonance (NMR) detectors that are compatible with planar microfluidic devices. This will enable in situ observation of sub-mM concentrations of sample on a removable microfluidic chip.

1.2 Motivation

By combining microfluidic devices with NMR spectroscopy, the samples within the device can be measured directly without disturbing or destroying the sample. This means that samples can be studied over a period of time. Cellular processes produce a range of metabolites which can give an insight into how the cell is behaving.[11] By monitoring the metabolites produced over a period of time it is possible to see how the cells respond to different stimuli, for example addition of a drug molecule. It is important that the detector is sensitive so that the sub-mM concentrations often found in these systems can be observed in a few minutes of experiment time.

Sensitive detection methods have many other uses other than just microfluidics. Increasing sensitivity can reduce experiment time or mean that experiments require smaller samples. This can be especially useful in cases where sample size is limited, for expensive samples such as isotopically labelled compounds.

1.3 Microfluidic Technology

Microfluidic technology utilises small sample volumes to offer precise control and manipulation of liquids on a μl scale. These devices are making rapid advances in enabling novel approaches to life science research,[12] medical diagnostics,[13] and forensic investigations,[14] by offering a convenient platform for integrating complex biochemical functionality in a compact and expendable package. On the one hand, various biochemical assays based on protein and nucleic acid detection have been integrated with sample preparation to provide point-of-care diagnostic capabilities.[15] At the same time, microfluidic systems offer the ability to create complex artificial environments for the culture of biological systems including cells,[16,17] tissues,[18] and small organisms,[19] with exquisite control over the conditions. One of the most striking examples is the development of organ-on-chip systems based on controlled differentiation of induced pluripotent stem cells.[20]

1.4 NMR

NMR spectroscopy is one of the most versatile and sophisticated techniques for the study of condensed matter. It can provide information on the structure of molecules, as well as the quantities present. However, NMR measurements rely on exposing samples to large and extremely homogeneous magnetic fields, and typically require at least tens, and typically hundreds of μl of sample to be filled into a standard sample container commonly a cylindrical sample tube of 5 mm or 10 mm diameter. Our aim is to enable high-resolution NMR spectroscopy to be used to study samples in situ in microfluidic devices, without the need to remove them from the chip. Ideally, this approach would provide NMR spectra of similar quality, in both sensitivity and resolution, to that typically achieved in the standard configuration.

In principle, NMR spectroscopy would complement microfluidic systems very well, enabling non-destructive and non-invasive observation of metabolic processes in real time and in situ.

However, integration of microfluidic systems with NMR spectroscopy presents a number of challenges. Conventional liquid-state NMR spectroscopy is mostly done in 5 mm sample tubes, on probe volumes between 200 and 800 μl. By contrast, microfluidic

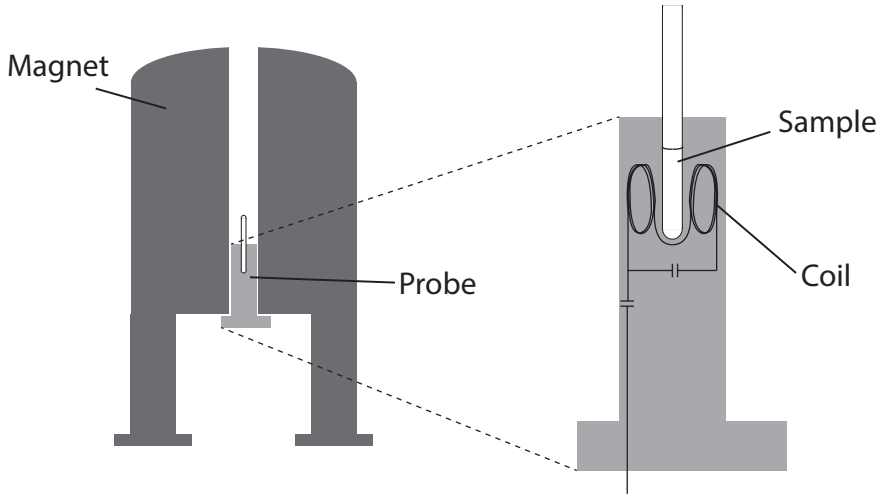

Figure 1.1: Diagram showing the positioning of the probe within the magnet

lab-on-a-chip (LoC) devices are extended planar networks of channels and chambers. While the overall size of such LoC devices is similar (several cm) to that of conventional NMR detection coils, the volumes contained in their channels are on a μl scale. Simply inserting an LoC device into a standard probe therefore leads to very low filling factors, and correspondingly poor sensitivity.

A possible alternative to NMR is Electron Paramagnetic Resonance (EPR) spectroscopy. This uses similar techniques to NMR but excites electron spins instead of nuclear spins. This has potential to be more sensitive than NMR but requires an unpaired electron so is usually used for studying metal complexes or organic radicals. The purpose of this probe is primarily studying organic molecules where all electrons are paired so EPR wouldn't be useful for this purpose.

1.4.1 The probe

The NMR probe is used to position the sample in the desired location within the bore of the NMR magnet. In a conventional setup the sample sits within a coil used to excite the sample and detect the nuclear spins as in Fig 1.1. The probe acts simultaneously as a sample holder, activator of spin excitation, and NMR signal detector. The aim of this work is to develop a probe with a detector that is compatible with planar microfluidic devices, and that has sufficient sensitivity to detect sub-mM concentrations in a μl sample volume within a few minutes of experiment time.

1.4.2 Spectral resolution

NMR spectroscopy is able to differentiate very small differences in chemical environments. Information can be interpreted as to the functional groups present in a molecule, as well as the neighbouring substituents. In order to determine these differences the linewidths of the spectral peaks must be very narrow, to the order of 1 Hz or below. This corresponds to 3 parts per billion in a 300 MHz system. These small differences are observable in NMR because the interaction between the nuclear magnetic moments and their surroundings are extremely weak. To achieve these narrow linewidths the magnetic field has to be very homogeneous. Magnetic field homogeneity within the static magnetic field is achieved using a collection of shim coils, adjusted to cancel out magnetic field inhomogeneities. Inhomogeneities will be caused by objects placed in the magnetic field, particularly where there are large magnetic susceptibility differences. The geometry of the detector will have to take this into account so as not to reduce the spectral resolution.

Chapter 2

NMR and Sensitivity

2.1 Introduction

Microfluidic devices operate at small sample volumes, often of the order of 1 μl. In many cases this means that the number of spins present in the sample will be 10^2 to 10^3 times fewer than in a conventional NMR setup. For a 1 mM concentration of sample in a 2 μl volume this corresponds to 2 nmol, whereas the same concentration in 500 μl would contain 500 nmol, a factor of 250 difference. To get the same signal intensity from the smaller sample would take 62500 times longer than the larger sample making the experiment impractical. Methods of increasing the sensitivity of the NMR experiment are required. This section will introduce what happens during the NMR experiment, explore the factors that determine sensitivity in NMR, and look at how these can be overcome to form sensitive NMR detection techniques.

2.2 Magnetisation

In atoms where the spins of the protons and neutrons within the nucleus are not paired, the overall spin of the nucleus generates a magnetic dipole. The magnitude of this dipole is the nuclear magnetic moment. When the sample is placed in a strong static magnetic field (B_0), the net distribution of spin orientations aligns with the field. The nuclear magnetic moment can align with the external magnetic field B_0 in $2S + 1$ different ways, where S is the nuclear spin. For example, ^{1}H has a spin, $S = 1/2$ so can align

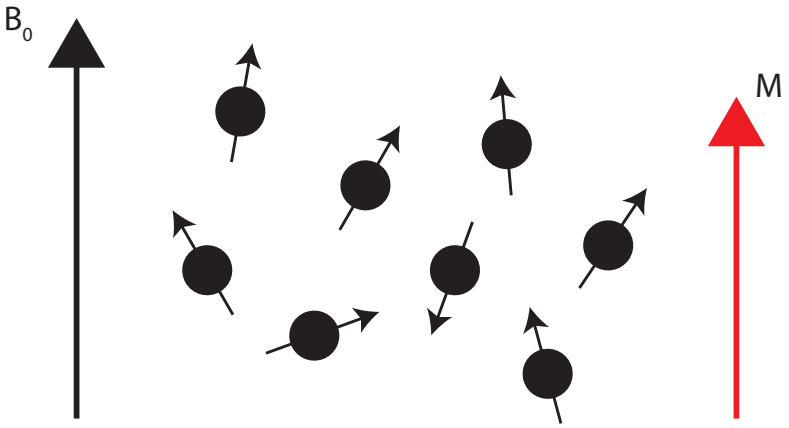

Figure 2.1: Nuclear spins will point in different directions but the overall magnetisation (M) will align with the static magnetic field (B_0)

with B_0 in 2 directions, either reinforcing or opposing B_0. Over a sample volume these individual magnetic moments combine to give a density of magnetic moments known as the magnetisation M (Figure 2.1). The total magnetisation is determined by the difference in population of the two energy levels, and it is this magnetisation that is quantified by NMR.

Magnetisation is dependent on the separation of the two energy levels (proportional to B_0) and the amount of energy present to allow transition between the two levels (proportional to the temperature of the sample, T). This relationship is shown by the Boltzmann equilibrium law:[8]

$$M = N\frac{\gamma^2 s(s+1)\hbar}{3k_B T}B \tag{2.1}$$

N is the spin density of nuclei within the sample, γ is the gyromagnetic ratio, $\hbar$ is Planck's constant divided by 2π, k_B is Boltzmann's constant, and T is the sample temperature.

The gyromagnetic ratio (γ) is an intrinsic property of the particular atomic species. It is related to both the magnetic moment (μ) and spin (S) by the following formula:

$$\mu = \gamma S \tag{2.2}$$

At room temperature the energy required for a nuclear magnetic quantum transition is approximately 10^{-25} J at a field of 11 T, around 4 orders of magnitude less than the available thermal energy.[5] This means that the net magnetisation will be very small, and so a large number of spins is needed to give a discernible signal.

From Equation 2.1 it can be seen that magnetisation can be increased by increasing the number of spins in the sample, decreasing the sample temperature, increasing the external magnetic field, or by increasing γ.

2.3 Precession

It is possible do detect the magnetisation of a single spin using magnetic resonance force microscopy.[21] However, to maximise sensitivity when detecting the nuclear magnetisation, a resonance approach is used.[22,23] This method utilises the variation in the magnetic field when the magnetisation is shifted from it's equilibrium position. Manipulation of the magnetisation is achieved by passing a current through the detecting coil. This generates a magnetic field B_1 that is perpendicular to the static magnetic field. The angle by which the magnetisation is rotated (θ) in a period of time (τ) can be calculated by Equation 2.3.[8]

$$\theta = \gamma(\frac{B_1}{2})\tau \tag{2.3}$$

After altering the position of the magnetisation, the magnetisation then precesses around the static magnetic field (Fig. 2.2). The angular frequency of precession (ω) can be calculated by:

$$\omega = -\gamma\ B_0 \tag{2.4}$$

γ is the gyromagnetic ratio and B_0 is the static magnetic field.

The frequency of precession is dependent on the gyromagnetic ratio of the nucleus being studied but also the static magnetic field. However, there are some small differences that are dependent on the local environment that the nucleus experiences. These differences

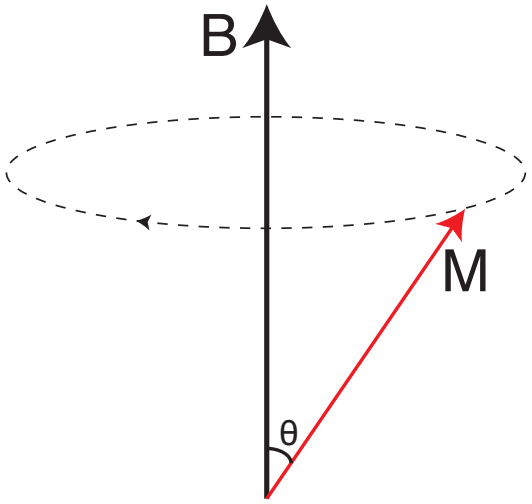

Figure 2.2: Precession of nuclear magnetisation (M) around the static magnetic field (B) after altering the magnetisation from its equilibrium position

cause separate peaks in the NMR spectrum, which gives useful information into the molecules present in the sample. Some of the key features are discussed in the following sections.

2.3.1 Chemical Shift

While the B_0 magnetic field is homogeneous on a macroscopic scale, on a microscopic scale there are small fluctuations. The distribution of electrons surrounding the nucleus can oppose or enhance the B_0 magnetic field. This is known as nuclear shielding. Nuclear shielding causes a shift in the magnetic field experienced by a nucleus and is characteristic of the local chemical environment. Due to the relatively small chemical shifts experienced compared to the usual Larmor frequencies in hundreds of MHz, they are usually reported in a parts per million (ppm) scale relative to a reference frequency. This also has the advantage of being independent of magnetic field strength used in the experiment as Larmor frequency and chemical shift frequency both scale equally with B_0, leaving the ppm value unchanged.

Chemical shifts can give information on the local secondary structure of molecules. The electron distribution is affected by the local geometry and so clues can be discovered into features such as nearby nuclei, bond lengths, and angles between bonds.

2.3.2 Spin-spin coupling

Another factor that causes changes in the nuclear precession frequency is the local magnetic fields caused by the nuclei themselves. These influence the energies of nearby nuclei in a effect known as spin-spin coupling. These couplings can be split into J-couplings and dipolar couplings.

Dipolar coupling arises because each nuclear spin generates a small magnetic field, this will influence other nuclear spins in the vicinity. This interaction is mutual and the first nucleus will be equally influenced by the second. This coupling occurs through space and are used extensively in solid state NMR. In the liquid state, dipolar couplings average out to zero because of rotation in the molecules.

J-coupling is seen between nuclear spins that are linked through chemical bonds. It arises from hyperfine interactions between nuclei and local electrons. This means that J-coupling can be observed in isotropic liquids. The magnetic fields of two nuclei can either oppose or reinforce each other which will cause splitting in the spectral peaks. From this information the number of nearby NMR-active nuclei can be determined and also more information into the connectivity in the molecules. J-coupling is also used in the design of NMR experiments for the purpose of magnetisation transfer via these couplings.

2.4 Detection

As is expressed in the Maxwell-Faraday equation (Eq. 2.5), a changing magnetic field is always accompanied by an electric field:

$$\nabla \times \mathbf{E} = -\frac{\partial \mathbf{B}}{\partial t} \tag{2.5}$$

As the magnetisation precesses back to the equilibrium position the magnetic field is altered. If a conductor is present, such as a wire or coil, an electromotive force (emf) will be generated. Equations 2.4 and 2.5 demonstrate that a greater static magnetic field

strength will improve sensitivity. ω is proportional to B_0, so as B_0 increases ω will increase. A faster frequency of rotation will increase the speed at which the magnetisation changes ($\frac{\partial \mathbf{B}}{\partial t}$) and so generate a larger emf.

Following the radio-frequency excitation there is a time where the spins are allowed to precess. Due to small variations in the microscopic magnetic fields, the precession of the individual magnetic dipoles gradually gets out of phase. The time period over which this occurs is the transverse relaxation (T_2). As precession occurs the magnetisation relaxes back to the thermal equilibrium position, aligned with B_0. The decay constant for this relaxation time is known as T_1.

Assuming that at equilibrium the magnetisation is aligned with the z axis (M_z), then at a time t after the excitation pulse the sample magnetisation has the following form:

$$M_y = -M_0 \cos(\omega_0 t) \exp\{-t/T_2\} \tag{2.6}$$

$$M_x = -M_0 \sin(\omega_0 t) \exp\{-t/T_2\} \tag{2.7}$$

$$M_z = M_{z,eq} - M_{z,eq} \exp\{-t/T_1\} \tag{2.8}$$

Where M_0 i the magnetisation immediately after the pulse, $M_{z,eq}$ is the magnetisation at equilibrium, T_1 is the longitudinal relaxation constant, and T_2 is the transverse relaxation constant.

The oscillating magnetic field generates an electric field, creating an oscillating electric current in the coil. The generated voltage is the NMR signal or free induction decay (FID).

The NMR signal is then amplified by a preamplifier, which scales up the very small signal to a more useful voltage. The signal is oscillating at very high frequency, typically hundreds of MHz and this must be reduced in order to convert the signal into a digital form. A quadrature receiver converts the signal to a lower frequency by comparing it with a reference frequency ω_{ref} to generate a new signal called the relative Larmor frequency (Ω_0):

$$\Omega_0 = \omega_0 - \omega_{ref} \tag{2.9}$$

From the quadrature receiver there are 2 output signals, a real and imaginary component. These two signals are digitised using an analogue-to-digital converter (ADC).

The NMR signal for a single frequency can be expressed as:

$$s(t) \sim \exp\{(\mathrm{i}\Omega_0 - \frac{1}{T_2})t\} \tag{2.10}$$

However, NMR spectra tend to have multiple signals. The overall NMR signal of a standard sample is made up of a complicated mixture of individual signals, not just one frequency.

A more general form for the NMR signal would therefore be:

$$s(t) = \sum_l s_l(t) \tag{2.11}$$

where

$$s_l(t) = a_l \exp\{(\mathrm{i}\Omega_l - T_{2,l})t\} \tag{2.12}$$

This gives a combination of many different components (s_l), where each component has an amplitude (a_l), frequency (Ω_l), and transverse relaxation rate constant (T_2).

2.5 The NMR Spectrum

Deciphering these signals is achieved using a Fourier transform. This converts the signal as a function of time into a spectrum as a function of frequency. The Fourier Transform is defined as follows:

$$S(\Omega) = \int_0^\infty s(t) \exp\{-\mathrm{i}\Omega t\} \, \mathrm{d}t \tag{2.13}$$

This is hugely beneficial as it means that the individual components of the signal are easily visible as separate peaks on the spectrum.

2.6 NMR experiments

The process described so far is that of a simple pulse acquire NMR spectrum. This gives a one dimensional spectrum of the sample. Using different sequences of pulses the nuclear spins (and the resulting spectra) can be manipulated. This section describes some of the experimental techniques used in this work.

2.6.1 Water Suppression

Liquid state NMR spectroscopy uses a variety of solvents for sample preparation depending on the sample required. In biological systems the solution is water based. Water has a concentration of approximately 55.5 M and two ^{1}H nuclei per molecule. This results in an extremely large peak at around 4.6 ppm compared to peaks of metabolites around 1 mM. It is useful to try and remove this peak from the spectrum so that any peaks in this region can be observed. Using a deuterated solvent such as D_2O will reduce the size of the solvent peak but to remove it completely a solvent suppression scheme is needed.

Water suppression involves a low power pulse at the frequency of the solvent nucleus before the NMR experiment begins. This pulse excites the water proton signal so that during the actual NMR experiment no signal can accumulate and be measured.

2.6.2 Heteronuclear Single Quantum Coherence (HSQC) Spectroscopy

The HSQC experiment[24] detects protons connected to an NMR-active heteronucleus such as ^{13}C. This is achieved by transfer of magnetisation using an Insensitive Nuclei Enhanced by Polarisation Transfer (INEPT) pulse sequence.[25] Magnetisation is transferred from ^{1}H, a sensitive nucleus with high gyromagnetic ratio, to ^{13}C, a nucleus with lower sensitivity and a lower gyromagnetic ratio. The transfer is achieved through the J-couplings between the two nuclei. There is then an evolution period during which the frequency of the ^{13}C nuclei is altered to the ^{13}C chemical shift. This magnetisation is then transferred back to the ^{1}H nuclei by a second INEPT sequence and the magnetisation is then detected.

The HSQC signal is increased compared to direct ^{13}C experiments. This is important for heteronuclear experiments where the amount of sample is limited so that maximum

sensitivity can be recorded. The resulting NMR spectrum is two-dimensionsal with ^{1}H recorded in the direct dimension and ^{13}C recorded in the indirect dimension. Resonances are observed for each ^{13}C-^{1}H correlation in the molecules present.

2.6.3 Heteronuclear Multiple Quantum Coherence (HMQC) Spectroscopy

The HMQC experiment is similar to the HSQC. It uses a 90° ^{1}H pulse to create transverse magnetisation. This is then transferred to the heteronucleus by a 90° ^{13}C pulse to create heteronuclear multiple quantum coherences. As with the HSQC the coherences are allowed to evolve to the ^{13}C chemical shift before being transferred back to the ^{1}H nuclei and detected. The HSQC offers better resolution and sensitivity in the indirect dimension compared to HMQC. Peaks in the HSQC spectrum are singlets while the HMQC contains multiplets. However HMQC experiments are often easier to implement as the pulse sequence is simpler and so this will be used first to test heteronuclear experiments in this work.

2.6.4 Total Correlation Spectroscopy (TOCSY)

The TOCSY experiment shows cross peaks of homonuclei (for example two ^{1}H nuclei or two ^{13}C nuclei) that are connected by a chain of couplings. It is therefore useful for identifying interconnected networks of spin couplings and can be used to separate the peaks of mixtures of molecules. The key feature of this experiment is a period of isotropic mixing during which magnetisation is transferred between spins which are connected through a chain of couplings.

It is possible to implement this isotropic mixing stage on other experiments such as the HMQC experiment. This creates an HMQC-TOCSY experiment where by covariance processing of the HMQC spectrum a TOCSY spectrum of the heteronucleus can be obtained. This is an effective way to indirectly obtain a TOCSY spectrum of ^{13}C.

2.7 Probe Sensitivity

Description of the signal to noise ratio available in an NMR experiment is taken from a combination of work by Hoult and Richards,[26] Levitt,[27] and Mispelter et al.[8]

The signal generated from a sample can be calculated using the principle of reciprocity. A $\mathbf{B_1}$ field generated by a coil will be stronger at a point close to the coil than further away. In the same way, a precessing magnetic dipole ($\mathbf{m}$) closer to the coil will induce a greater signal than the signal from a dipole at a further distance. The induced emf (ξ) at a point is given by:

$$\xi = -(\partial/\partial t)\{\mathbf{B_1} \cdot \mathbf{m}\} \tag{2.14}$$

For a sample with a volume V_s we need to know B_1 at each point in the sample:

$$\xi = -\int (\partial/\partial t)\{\mathbf{B_1} \cdot \mathbf{M_0}\}\ \mathrm{d}V_s \tag{2.15}$$

$\mathbf{M_0}$ is the total magnetisation. If the B_1 field is homogeneous then Equation 2.15 simplifies to:[8]

$$\xi = K\omega_0(B_1)_{xy}M_0V_s\cos\omega_0 t \tag{2.16}$$

K is an inhomogeneity factor caused by the geometry of the coil. To maximise the signal from an NMR experiment it is therefore important to maximise ω_0 and M_0 (both proportional to B_0), the B_1 induced magnetic field, and the sample volume V_s. However as well as maximising signal it is equally important to minimise noise.

Noise predominantly originates from the thermal noise generated by agitation of electrons in the coil. For a given bandwidth, the root means square (rms) of the voltage can be calculated as follows:

$$V = (4k_BT_c\Delta fR)^{1/2} \tag{2.17}$$

where k_B is the Boltzmann constant, T_c is the coil temperature, Δf is the bandwidth in Hz, and R is the resistance.

Alternating electric current distributes throughout a conductor so that the current density is greatest near the conductor surface. At high frequencies current is restricted

almost entirely to the conductor surface. For example at 300 MHz the skin depth in copper is approximately 3.7 μm. Approximating the current to be restricted to the current surface allows R to be calculated for a long straight cylindrical conductor using the following:

$$R = (l/p)(\mu\mu_0\omega_0\rho(T_c)/2)^{1/2} \tag{2.18}$$

l and p are the length and circumference of the conductor respectively, μ is the conductor permeability, and $\rho(T_c)$ is the resistivity.

Combining equations 2.1, 2.16, 2.17, and 2.18 an equation for the SNR can be generated:

$$\Psi_{rms} = \frac{K(B_1)_{xy}V_sN\gamma\hbar^2I(I+1)}{7.12kT_s}\left(\frac{p}{FkT_cl\zeta\Delta f}\right)^{1/2}\frac{\omega_0^{7/4}}{(\mu\mu_0\rho(T_c))^{1/4}} \tag{2.19}$$

F is the preamplifier noise and ζ is a proximity factor. This is quite a hefty equation but there are only a few variable factors that determine the SNR. $K(B_1)_{xy}$, p, and l are the only factors that depend on the coil geometry. T_c is the coil temperature, $\rho(T_c)$ is dependent on the material that the coil is made from and F is down to the quality of the preamplifier. For a solenoid we can therefore use the following approximation:

$$\Psi \propto V_s(B_1)_{xy}(p/l)^{1/2} \text{ or } V_s(B_1)_{xy}/R^{1/2} \tag{2.20}$$

Also from Equation 2.19 it can be seen that the relationship between SNR and the Larmor frequency is to the power 7/4. There are some unpublished observations[7] that suggest that the practical sensitivity improvement may scale linearly with B_0 rather than ${B_0}^{7/4}$, although it has been shown experimentally that sensitivity improvements with ${B_0}^{7/4}$ or even slightly greater can be seen.[28,29]

When a probe and transmitter are matched, the power supplied W dissipates in the resistance R of the coil. The current flowing though the coil is calculated by:

$$I = (W/R)^{1/2} \tag{2.21}$$

The irradiating field is calculated from $(B_1)_{xy}$, the radio-frequency field for unit current:

$$(B_1*)_{xy} = I(B_1)_{xy} = (B_1)_{xy}(W/R)^{1/2} \tag{2.22}$$

Combining this with Equation 2.20 gives:

$$(B_1*)_{xy} \propto W^{1/2}\Psi/V_s \tag{2.23}$$

This demonstrates that the 90° pulse length is a direct measure of the SNR (assuming the number of nuclear spins is equal and that the same power is used).

Comparison of sensitivity of probes is quantified by the normalised limit of detection (nLOD) This is defined as "the number of spins that have to resonate within a bandwidth of one Hertz to yield an SNR of 3." [5] In the frequency domain nLOD is calculated as follows:

$$\mathrm{nLOD}_\omega = \frac{3n_s\sqrt{\Delta t}}{\mathrm{SNR}_\omega} \tag{2.24}$$

where n_s is the number of nuclear spins that correspond to a peak in the NMR spectrum, Δt is the experiment time, and SNR_ω is calculated from the maximum amplitude of the corresponding spectral peak, divided by the square root of twice the variance in an area of the spectrum with no peaks. [5]

2.8 Methods of Increasing Sensitivity

Increasing the strength of the static magnetic field will always improve sensitivity, assuming that other factors stay the same. A higher field strength will increase the magnetisation in the sample and also generate a higher frequency of precession. Developments to improve the B_0 field strength are ongoing and strengths of 23.5 T for high-resolution NMR spectroscopy have been reported. [30] However, these systems are very expensive and not always readily available. This work assumes that the equipment available is at a fixed magnetic field and the aim is to improve sensitivity using the existing superconducting magnet.

At thermal equilibrium, the net distribution of nuclear spins is parallel with the static magnetic field, with a greater number of spins along the field than opposed to the field. The thermal energy at room temperature is much greater than the energy difference between the two states, meaning that the population difference between spins aligning and opposing the magnetic field is very small. This effect makes the sensitivity of NMR inherently weak, meaning that a relatively large amount of sample is required compared to other analytical techniques such as mass spectrometry.

Several methods of boosting the polarisation in methods known as hyperpolarisation have been proposed. These include para-hydrogen-induced polarisation (PHIP),[31,32] optical pumping,[33] and dynamic nuclear polarisation.[34,35] These techniques have the potential to increase the observed signal by over 10,000 times, but are limited to certain molecules and incorporation into microfluidic devices is challenging. PHIP has been combined with microfluidics, albeit by remote not in situ detection.[36]

The simplest way to increase signal is to maximise the number of spins within the sample volume. In microfluidic devices this is limited by the small sample volume. In addition, it is not always possible to use more sample. For example, when using expensive samples, or concentration-limited samples such as sample of metabolites or proteins.

Another method of increasing signal is signal averaging. NMR signals are reproducible, while the noise is random. By repeating the experiment and adding the signals together the SNR is increased. The increase in SNR is proportional to the square root of the number of experiments. This technique becomes impractical beyond a certain point as the time taken to increase the signal becomes extremely long.

As well as trying to boost signal, one way of increasing SNR is to reduce the amount of noise present in the spectrum. The main source of noise is thermal noise from the motion of electrons in the metal. Cooling the coil and the pre-amplifier to cryogenic temperatures will reduce the noise.[37] This technique is often used for NMR spectroscopy on a standard sample size. The drawback with this method is that maintaining the sample at room temperature (or body temperature in the case of biological samples) is a major technical challenge on micro-scale systems. A flow of air can be used to prevent the sample from cooling[38] but this air gap reduces the filling factor, negating the benefit of cooling the circuitry.

2.9 Spectral Resolution

In the case of a perfectly homogeneous B_0 magnetic field the peak width in Hz at half height is $1/(\pi T_2)$. A larger value of T_2 gives a slow signal decay and narrow linewidth.

However the B_0 magnetic field is never perfectly homogeneous. It may be distorted by imperfections in the equipment setup or by magnetic susceptibilities introduced by the sample. The nuclear spins will experience a slightly different static magnetic field depending on their position and since the Larmor frequency is dependent on the B_0 magnetic field nuclei that may have the same inherent chemical shift will precess at slightly different rates. The effect of B_0 inhomogeneity is broadening of the spectral peaks, known as inhomogeneous broadening.

Spectral broadening is undesirable as it may make peaks that are close to each other indistinguishable. In addition to this, broadening reduces the peak amplitude. For samples where the peaks are only just visible above the noise these broadened peaks may get lost in the noise unless experiment time is increased.

In micro-NMR, spectral resolution is often limited by differences in magnetic susceptibilities between different materials in the coil, sample holder, and the sample itself. These magnetic susceptibility mismatches cause field variations over the sample volume, limiting resolution. Efforts to minimise susceptibility broadening include using a susceptibility matching fluid, which has a similar magnetic susceptibility to the sample holder.[39]

2.10 Micro-NMR detectors

To improve the signal generated by the precession, a resonant circuit is used. These circuits store energy oscillating at the circuit's resonance frequency. The greater the energy stored in the circuit the more efficient the detector will be, both at manipulating the nuclear spins and at gathering the resulting signal. The performance of the resonator can be described by the Q factor. The dimensionless parameter Q is used to describe the energy loss in a resonator, with a higher Q indicating a low rate of energy loss.

The circuit is tuned by a capacitor to resonate at the frequency of precession. As the magnetisation precesses around the static magnetic field the oscillatory field in the resonator increases, and provided a high quality capacitor is used, the induced emf in the resonator will be Q times greater than in a non-resonant circuit.

Commonly, Alderman-Grant resonators or saddle coils with diameters ranging from 4 to 12 mm and lengths of 8 to 15 mm are used in commercial liquid state NMR probes for excitation and detection.

It has been demonstrated theoretically and experimentally that miniaturised NMR detectors benefit from a favourable scaling of mass sensitivity (the absolute number of spins required for a detectable signal) with probe volume.[40,41] This had led to flow probes with very high sensitivity based on micro-solenoid coils wound around glass capillaries. More recently, capillary detectors have been combined with microfluidic devices to form remote-detection systems, in which a large coil is used for spin excitation and encoding, and signals are detected downstream from liquid flowing out of the chip into a capillary NMR detector.[42] While this is an elegant approach, it requires a fluidic connection between the microfluidic device and the NMR system, and therefore not an in-situ technique.

Down-scaling of existing detector geometries isn't always feasible. Miniaturised saddle coils have rarely been successful.[43]

2.10.1 μ-Solenoids

One commonly used geometry of detector is the micro-solenoid. The solenoid is an axial resonator, the B_1 magnetic field generated is parallel to the resonator axis. They must be placed perpendicular to the B_0 static field. This positioning may lead to B_0 inhomogeneity and also makes access to the sample difficult.

Small scale solenoids have been used for sensitive detection in many instances, using capillary sample holders.[26,41,44] To minimise magnetic susceptibility broadening the coil and sample capillary are immersed in a fluid that matches their susceptibility as much as possible.[41] Use of multiple coils inductively coupled to one receiver makes simultaneous scanning of different samples possible.[45]

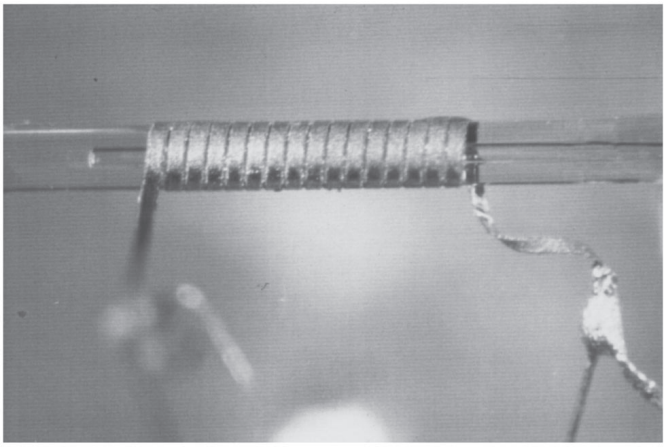

Figure 2.3: Image of a microsolenoid coil made by microcontact printing taken from Rogers et al.[1]

μ-solenoid coils can be hand wound, or wound with the help of mechanical winding devices. More advanced techniques have been developed, including microcontact printing followed by electroplating,[1] focused ion beam,[46] or lathe machining.[43] Wire bonding machines can produce solenoids on cylindrical templates produced lithographically.[47] This greatly improves the reproducibility of solenoidal microcoils.

This design is not investigated for use with microfluidic devices because of the incompatible geometry. Due to the cylindrical shape a microfluidic device cannot be simply inserted into the coil and so is not suitable for our purposes. It would be possible to use this detector to measure samples from a capillary attached to the device and then pump the sample through, however this would then not be an in situ technique and would disturb the sample.

2.10.2 Planar spiral μ-coils

Typically made using lithographic techniques, these planar designs are suited to microfluidic applications as well as detection of thin films and interfaces. They can also be produced without the need for clean room procedures, by etching copper-laminated polyimides,[2] or by functional ink-jet printing.[48]

Planar coils tend to produce somewhat less homogeneous magnetic fields than solenoids. This is because the outer coil windings contribute less to the magnetic field at the centre

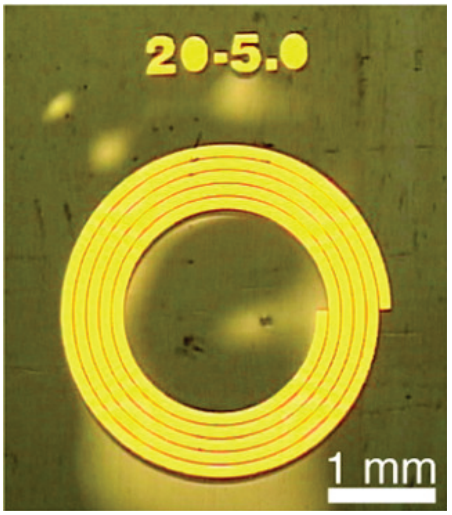

Figure 2.4: Image of an inductively coupled planar microcoil taken from Ryan et al.[2]

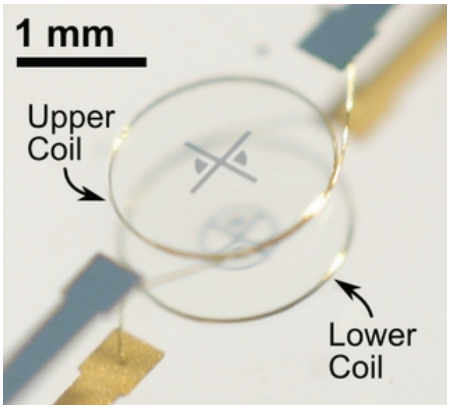

Figure 2.5: Image of a microfabricated Helmholtz coil taken from Ryan et al.[3]

than the inner windings.[49] Planar μ-coil detectors have been used in portable NMR systems which utilise permanent magnets.[50]

Despite the seemingly lower homogeneity, high-resolution NMR spectroscopy has been performed using self-resonant inductively coupled microcoils.[2] The inductively coupled nature of these coils allows easy insertion and removal of the microfluidic chip from the spectrometer, having potential applications as a high throughput technique.

2.10.3 Helmholtz Pairs

Helmholtz pairs use two solenoidal coils on the same axis, producing a region with near uniform magnetic field homogeneity. This technique has been shown to offer increased

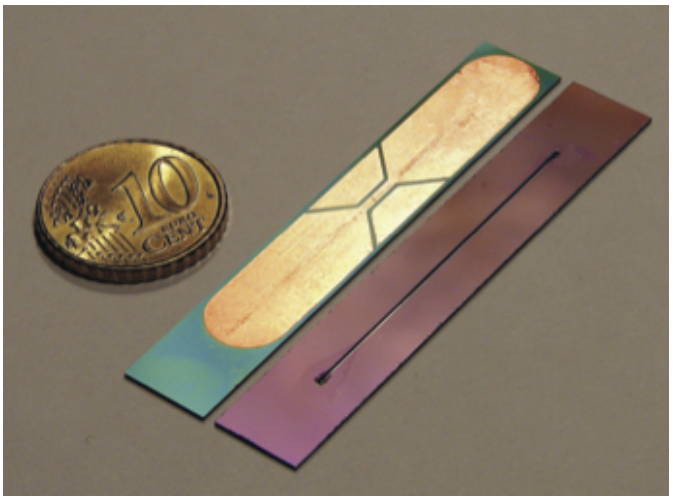

Figure 2.6: Image of a coil with stripline geometry taken from Kentgens et al.[4]

sensitivity over a solenoidal microcoil.[51]

2.10.4 Stripline

Another planar detector design, these linear geometries use a single current path instead of a coil with numerous windings.[52] The sample is exposed to the magnetic field generated by the current passing through the single channel. A constriction in the region where the sample is located maximises the B_1 field generated.[53]

Striplines are a transverse resonator meaning that the create a magnetic field perpendicular to the main axis. This make sample accessibility much easier.

Linear detectors are much more easily manufactured than micro-solenoids. Aligning the linear geometry with the external magnetic field minimises susceptibility broadening effects. They also give very good B_1 field homogeneity.[54]

This design will be investigated further as it meets the requirements of a microfluidic detector. It is planar, meaning that a microfluidic device and because of it's simple geometry provides good homogeneity as magnetic susceptibility boundaries are minimised.

Variants of the stripline include the microstrip,[55] and the microslot,[52] in which further constrictions are made to increase the generated B_1 magnetic field.

2.11 Comparison of Sensitivity

Sensitivity in microdetectors is quantified by the nLOD, this takes into account both the SNR that can be expected per nuclear spin in the sample, but also how many spins are accommodated within the active volume of the coil. nLOD is calculated in the frequency domain as in Equation 2.24 The sensitivities of a variety of detectors from literature are shown in Figure 2.7. For comparison the nLOD is scaled by a factor of 600 MHz/$\omega^{7/4}$ corresponding to a standard proton Larmor frequency of 600 MHz. The figure shows a clear trend between mass sensitivity and detector volume - sensitivity improves as the detector volume gets smaller.

However, it is also important to consider the concentration limit of detection (cLOD). This can be obtained by dividing the nLOD by the volume. It can be seen from Figure 2.7 that although mass sensitivity increases as the coil size gets smaller, the volume decreases as well meaning that the concentrations of sample within that volume need to be much greater in order to be detectable. If the sample is too concentrated line shape may be degraded and chemical shifts may be affected. These changes in spectral quality may be due to high viscosity or solute-solute interatctions.[7] Extremely small μNMR probes are only sensible when samples are mass-limited.

For the volumes that we are interested in (approximately 1 μl) the detectors with the best sensitivity currently are e[56] with an nLOD of 13.8 nmol $s^{1/2}$ for a 0.4 μl volume, and m[57] with an nLOD of 12.3 nmol $s^{1/2}$ for a sample volume of 0.5 μl. The detector with the best cLOD currently is p[58] with a cLOD of 0.6 mM $s^{1/2}$ although this uses a sample volume of 50 μl.

Using a commercial cryogenically cooled probe (with matched susceptibility plugs in a 5 mm sample tube) it is possible to reach a signal to noise ratio of 10:1 in 10 minutes acquisition in a 300 μl sample of 2 mM glucose.[7] This corresponds to an nLOD of 1.32 nmol $s^{1/2}$ to reach a signal to noise ratio of 3:1. This is 10 - 10^2 times more sensitive than many of the microcoil geometries with 10^4 times small volume. However this probe does have the advantage of cryogenic cooling which can boost sensitivity by a factor of five.[59] It is clear though that there is some potential to increase sensitivity in the μl sample volume range without the need to go to smaller volumes.

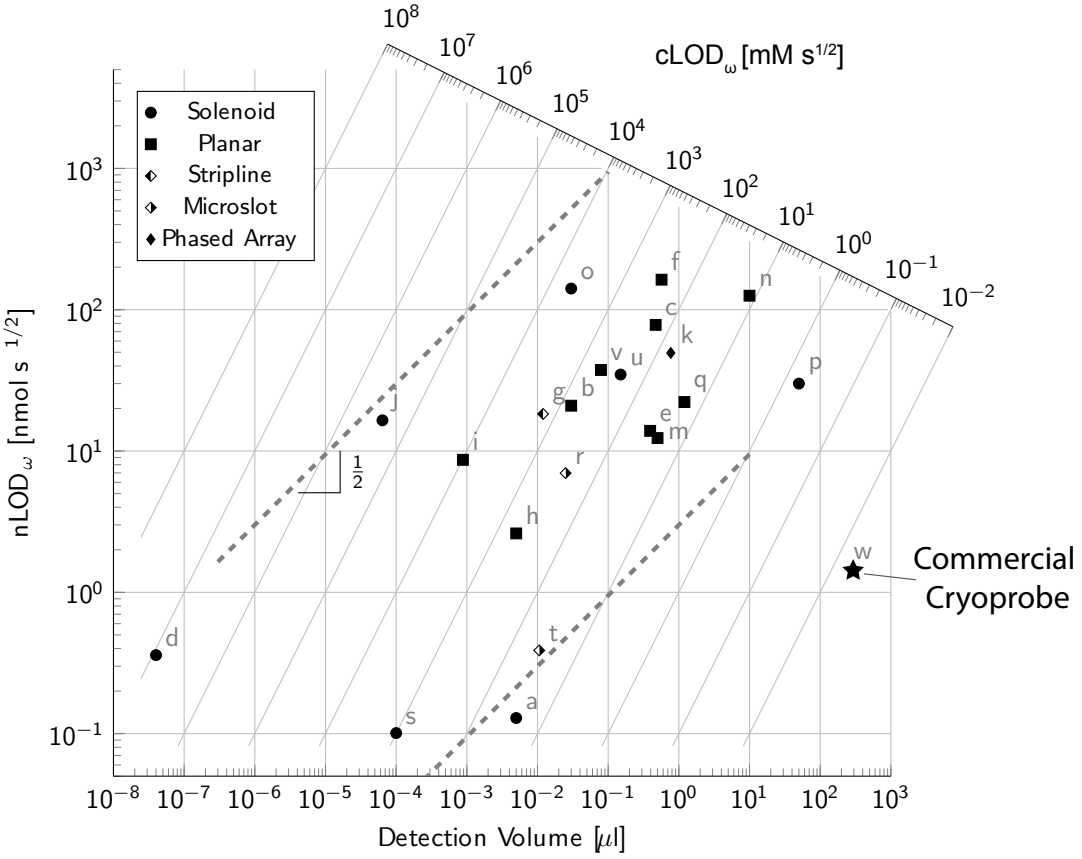

Figure 2.7: Sensitivity of various μ-detectors described as both nLOD and cLOD. The dashed line shows the correlation between detection volume and nLOD with a gradient of 1/2. Letters a-t correspond to different authors as cited by Badlita et al.[5] Data points u[6] and v[3] represent more recent work. Data point w[7] refers to a commercial cryoprbe. Individual references can be found in Table 2.1

Table 2.1: References for selected NMR micro-detectors shown in Figure 2.7

Detector	*Geometry*	*Reference*
a	Solenoid	Olson et al.[60]
b	Planar	Massin et al.[61]
c	Planar	Massin et al.[61]
d	Solenoid	Ciobanu et al.[62]
e	Planar	Trumbull et al.[56]
f	Planar	Wensink et al.[63]
g	Stripline	van Bentum et al.[53] and Kentgens et al.[4]
h	Planar	Ehrmann et al.[64]
i	Planar	Stocker et al.[39]
j	Solenoid	Badilita et al.[47]
k	Phased Array	Gruschke et al.[65]
l	Planar	Renaud et al.[66]
m	Planar Needle	Syms et al.[57]
n	Planar Helmholtz	Goloshevsky et al.[67]
o	Solenoid	Rogers et al.[1]
p	Solenoid	Yamauchi et al.[58]
q	Planar	Ryan et al.[2]
r	Microslot	Maguire et al.[68]
s	Solenoid	Seeber et al.[69]
t	Microslot	Krojanski et al.[70]
u	Solenoid	Meier et al.[6]
v	Planar	Spengler et al.[3]
w	Cryoprobe	Fan et al.[7]

Chapter 3

Microfluidic Devices

3.1 Overview

Microfluidics in general deals with liquid flows on a μl scale. It is considered a science in itself, the study of the behaviour of liquids at the μl scale, and also a technology. Microfluidic devices have been developed since the mid-1970's, when a chromatographic analyser was fabricated on silicon.[71] These devices are often also referred to as Micro Total Analysis Systems (μTAS) or Lab-on-a-Chip (LoC) devices in literature.

The idea of μTAS was proposed by Manz et al.[72] These systems incorporate sample handling, separation, and detection within a silicon chip. Many features can be included on a chip including mixing, pumping, sorting, analysis, and environmental control. The ability to have multiple functionalities within a single device where usually several pieces of lab equipment would be required gives rise to the idea of a lab-on-a-chip. Despite the agreeable idea of containing all of these features on a small device of a few cm, in reality external inputs and outputs are often required such as pumps or syringes.

Microfluidic devices have the advantage of using smaller amounts of sample and solvent, reducing waste and allowing analysis of expensive samples. They can also increase efficiency and the mobility of the analytical process. Another benefit is the ability to combine separation techniques such as chromatography and electrophoresis within a single device. Applications then spread from separation to the handling and reaction of biomolecules such as DNA amplification,[73] cell metabolism measurement[74] and flow cytometry.[75]

Microfluidic technology is desirable because it allows a large number of experiments to be conducted, making it suitable for high-throughput analysis.

3.1.1 Manufacture

Manufacture of microfluidic devices is convenient because of processes developed in the silicon microprocessors industry.[76] These techniques have made micro-lithography, machining and fabrication cheaper and more accessible.[77] Development of processes such as electrodeposition, etching, bonding, injection moulding, embossing, and soft lithography allows the use of a variety of materials to be used for microfluidic manufacture. Commonly used for microfluidics are polymers such as PDMS (polydimethylsiloxane), glass, and silicon. More recently paper-based microfluidic devices have even been developed[78] This range of materials creates microfluidic devices suited to different applications. Biological or chemical compatibility with the chip material, lower production costs or speed of manufacture, as well as specific optical characteristics.

Silicon is biocompatible in different forms such as single crystal silicon, silicon dioxide, polycrystaline silicon and substrates of the photo epoxy SU-8.[79] Silicon is opaque to visible and UV light, so is not compatible with traditional microscopy methods. Manufacturing with silicon tend to be expensive,[80] so isn't suitable for a disposable microfluidic device. The processes used for fabrication of silicon microelectronics can be applied to other materials.

Polymethylsiloxane (PDMS) is commonly used to make chips using a soft-lithography process due to the speed and ease of manufacture. Prototypes can be made quickly to test the desired application. PDMS has many advantages. It is transparent, meaning that is possible to see inside the chip and also is compatible with optical detection methods. PDMS is also gas-permeable allowing more complex microfluidic techniques.[81] It is possible to tune the surface properties to be more hydrophobic or hydrophilic.[82] PDMS can bind reversibly to glass, plastic, and other materials, as well as itself. It is also biocompatible, inexpensive and easily moulded. PDMS is gas permeable, which could be beneficial for oxygenation of the sample. However this also can lead to sample evaporation, and a loss of the stable environment characteristic of microfluidic devices.[83] In addition PDMS gives a broad background NMR signal which may overlap with small peaks in the NMR spectrum.

Poly(methyl methacrylate) (PMMA) is an alternative polymer to PDMS for microfluidics systems.[84] It has the advantage of being transparent, rigid and can be directly patterned using laser ablation.[85] PMMA is compatible with NMR spectroscopy and has a magnetic susceptibility that is very close to that of water.[86] This means that magnetic susceptibility broadening effects due to the boundary between the chip and the sample will be minimised, maintaining the best possible spectral resolution. For this reason PMMA is used for the microfluidic devices in our experiments.

Typically when making a microfluidic device the design is made computationally and transferred to a photomask. A resin is spread on a flat surface such as a silicon wafer to the desired thickness of the device. The resin is then exposed to UV radiation through the photomask, before being developed in a solvent to remove the areas of resin no exposed to UV light. This mould is then used to create the microfluidic channels. PDMS is poured into the mould with a cross-linking agent. Inlet and outlet holes are punched into the device which is then bonded to a glass slide.

Simple microfluidic devices can be manufactured using soft-lithography in the lab without the need for expensive equipment. Going to smaller and smaller scales requires an extra level of precision and often a clean room environment is needed to ensure the quality of the microfluidic channels meets the requirements.

3.2 Microfluidics

At the micro-scale fluid behaviour differs from that on a larger scale. The complex flow patterns have been modelled for various geometries with small volumes.[87] The system is dominated by factors such as fluidic resistance, surface tension, and energy dissipation. because of these factors microfluidic systems tend to have a low Reynold number (Re), a dimensionless parameter that describes the ratio of inertial vs. viscous forces in a liquid.[88] The flow of these liquids is laminar rather than turbulent. This means that liquids do not mix and molecules move between them via diffusion. The behaviour of these liquids is much more predictable than in larger scale systems. The environment within a microfluidic device (pH, temperature, concentration) can be closely controlled, giving more uniform reaction conditions.

On the micro-scale, surface and interfacial tension become dominant forces.[88] Fluids reduce free energy by contracting at the interface. Capillary action is also a dominant force at the micro-scale,[89] allowing fluids to move opposed to gravity.

Movement of liquids on this scale can be achieved a number of ways. Passive liquid manipulation methods often use capillary forces to transport fluids along a narrow channel. Additionally centrifugal forces can be closely controlled on a disk-shaped microfluidic device using precise rotational movements.[90] Other methods use active manipulation often combining micro-pumps and micro-valves. If continuous flow of liquid is required then external pumps[91] or pneumatic fluid handling systems[92] are usually required.

3.3 Applications

Microfluidic devices have a wide range of applications. Of interest here are applications in the life sciences. They can be use for diagnostic applications reducing assay volumes, and speeding up sample processing and analysis, allowing point-of-care diagnostics.[93] The high throughput nature of these devices could allow testing of the wider population rather than just once people experience medical issues which has the potential to lead to personalised/preemptive medicine.[94]

The phenomenon of interfacial tension dominating at the micro-scale has been utilised in microfluidic devices to sort protein and cells on a chip, and to perform protein crystallisation. Capillary action is used in personal diagnostic devices such as pregnancy tests and portable glucometers to measure blood sugar levels.[88] These are good examples of where previously complex biochemical assays can be performed to give an immediate measurement.

Assaying biological fluids using microfluidics can reduce time and the amount of sample required. For example, neutrophils are the phagocytotic cells that act as first responders in the innate immune system. These can be purified and analysed in a few minutes using just a few microlitres of blood from a finger prick, where previously it would take about an hour using some millilitres of blood taken from a venipuncture.[95] Purification of proteins is simple and fast. The dominant force of surface tension allows sorting of analytes across multiphase barriers. In addition to this sensitivity of protein purification is improved due to fewer wash cycles being needed to carry out an experiment.[96]

Microfluidics can offer solutions for diagnostics in low-resource settings, where expensive analytical equipment may not be available. For these applications cheap devices that are easy to operate are required. For example, a system has been developed to perform an ELISA-like assay to test for HIV. It doesn't need an external pumping system and uses cheap photodetectors for the readout which is available in around 20 minutes.[97]

In vitro models on a chip can create new strategies for drug development. In vivo organ function can be recreated on a microfluidic chip. Combining several microfluidic components, organ function, or disease function can be simulated. For example lung-on-a-chip,[98] or kidney-on-a-chip.[99] The hope is that these in vitro assays could be used to test the predicted effect of new drug molecules, before animal testing and human clinical trials.

3.4 Detection Methods

Microfluidic assays require a readout technique which obtains interpretable data by performing a chemical analysis on the system enclosed on the chip. Due to the small sample volumes, highly sensitive optical (fluorescence, chemiluminescence, and Raman spectroscopy) or electrochemical techniques are commonly used for this purpose.[100,101,102,103,104]

The most common optical detection method for microfluidic systems is fluorescence. This is due to the ease of which the systems can be coupled and the ability to detect small sample volumes.[105] Fluorescence spectroscopy uses a beam of light to excite electrons in certain molecules and then analyses fluorescence from the sample. It can be extremely useful for example in biological, chemical and medical study of organic compounds that contain a fluorophore such as tryptophan.[106] Fluorescence spectroscopy is extremely sensitive and can be used to detect a single molecule.[107] It is suitable for quantitative analysis where the compound being studied is known but lacks the resolution for distinguishing complex mixtures, such as in metabolomics.

Surface-enhanced Raman scattering (SERS) can qualitatively identify analytes. It enhances Raman scattering caused by molecules that are adsorbed onto rough metal surfaces by a factor of 10^{10} meaning that it is possible to detect single molecules.[108]

For example colloidal silver can be used to differentiate between thiophenol and 2-napthalenethiol.[109] This technique require metal nanoparticles, so aren't compatible with the biological processes that will be studied on the microfluidic devices.

Surface plasmon resonance permits study of binding interactions. It has been used to conduct substrate-ligand binding studies in droplets without without the need to use labels that may affect the binding process.[110] This again requires a metal surface so isn't a suitable technique for our purposes.

3.5 Combination with NMR

While these techniques are non-invasive (i.e., the analysis can be performed directly on the chip), they typically offer only limited chemical resolution, allowing the quantification of a handful of different species at most. Mass spectrometry (MS) also provides very good sensitivity,[111] and like NMR, can directly quantify a large number of metabolites. However, it is invasive, since it requires the removal of aliquots for injection into an MS ionisation chamber.

By contrast, NMR spectroscopy offers the possibility of completely non-invasive metabolomic readout. It is suitable for studying a wide range of molecules, particularly organic ones found in many biological systems.

Direct NMR detection of microfluidic chips was originally performed using planar microcoil integrated into the surface of a chip with a sample reservoir of 30 nl.[56] Spectra of water/ethanol were taken with a linewidth of 1.39 Hz as a proof of concept.

NMR studies of some biological molecules are enhanced by the use of isotopically enriched samples such as ^{13}C or ^{15}N. This process can be very expensive and utilising the sensitivity of microdetectors can make these experiments feasible.[112]

3.5.1 Hyphenated NMR

Combination of NMR with microfluidics has been used for 'hyphenated NMR', that is an amalgamation of NMR with other techniques such as liquid chromatography or capillary electrophoresis.

Liquid chromatography separates, purifies and analyses chemical mixtures. Combination with NMR on a ml scale is challenging due to the short detection time available as chemicals pass through the detection volume. Going to to smaller volumes increases the rate of the chromatography process. An optimal point is reached at around 50 nl where amino acid and peptide separation have been detected.[113] Applications of similar systems include metabolomics and biomarker identification. Studies of biological fluids such as urine, saliva or plasma can be performed when only limited sample is present.[114] This technique can also be used to study a large collection of samples by high throughput analysis. For example a system has been developed to analyse a 96 well plate in under 50 minutes using an HPLC pump, auto sampler, and a capillary flow NMR probe.[115] This method also uses 2 μl sample volumes and spectra with a signal to noise ratio of 10:1 can be obtained in 2 minutes using a sample concentration of 30 mM. Scaling this to a 1mM solution the experiment time would be approximately 3 hours to obtain a signal to noise ratio of 3:1.

In NMR-capillary electrophoresis analytes travel at different rates so some have a shorter period in the NMR active volume than others. There also challenges created by the electrophoretic current generating a magnetic field which will disrupt the peaks in the NMR spectrum. Also, Joule heat is generated in the system which reduces the ability of the NMR detection process. This techniques has been performed at the microscale, using a sample volume of just 5 nl.[116] The disturbance by the electrophoretic current can be nullified by stopping the electrophoresis while the sample is being studied.[117]

3.5.2 Remote Detection NMR

Remote detection has been shown by exciting the nuclear spins in a microfluidic device and then detecting them via a microcoil wrapped around the outlet capillary. This method can be used to characterise the flow of liquids, gas flows, and spectra of hyperpolarised ^{129}Xe.[118] This does provide a viable method for analysing samples on microfluidic devices, but doesn't provide in-situ analysis and will disturb the sample.

3.6 Metabolomics

Metabolomics is the study of the small molecules present within a living cell or organism. By monitoring the changes in metabolites and the concentrations of these molecules information can be gained into the physiological state of the cells or tissues being studied. This requires high sensitivity as well as good spectral resolution. Metabolomics applications include medical diagnosis,[119,120] food testing,[121] analysis of biochemical pathways[122] as well as drug discovery.[123]

Metabolism is altered by changes to the cellular environment for example in many widespread diseases.[124] By monitoring cell metabolism during treatment information can be found into the effectiveness of the treatment and cellular response. NMR metabolomics on a chip could provide a convenient method of high throughput screening for new drug candidates.

Mass spectrometry and NMR spectroscopy are the two leading analytical techniques used for metabolomics.[125] Currently mass spectrometry is the more commonly used approach for metabolomics but both methods have strengths and weaknesses.

Mass spectrometry is an analytical technique that offers both qualitative and quantitative information. Ionised fragments are separated according to their mass-to-charge ratio by acceleration through an electric or magnetic field. These ions are then detected by either inducing a charge or producing a current as they hit a detector surface. Mass spectrometry has increased sensitivity over many other analytical techniques, being able to detect individual atoms in the most sensitive cases,[126] and has an advantage over NMR in the number of compounds that can be resolved.[125] Mass spectrometry is also able to detect nuclei that are invisible to NMR such as ^{16}O and ^{32}S. However, it is a destructive technique meaning that an aliquot of sample has to be removed for analysis. This will disturb the sample meaning that experiments cannot be studied at intervals over an extended period of time.

3.6.1 NMR Metabolomics

Despite the strengths of mass spectrometry, for certain applications NMR spectroscopy has a number of advantages. NMR data is highly reproducible and offers superior

unknown structure determination. Importantly NMR is non-destructive, allowing in-situ observation of living systems. The more common molecules present in biological systems can be monitored without need for extraction, sample preparation or fractionation. Molecules with identical masses or different isotopomer distributions can be identified by using NMR spectroscopy.[125]

Conventional NMR spectroscopy offers only limited sensitivity, typically requiring several hundred μl of sample. As a result, NMR metabolomics has so far mainly found applications in medical diagnostics, where large samples are easily obtained from abundant body fluids such as urine or blood serum.[127] Additionally evaluation of the neurochemical environment of a rats brain has been done using in vivo micro-dialysis in combination with nanoprobe NMR spectroscopy.[128] This procedure records NMR spectra of a 20 μl sample of cerebrospinal fluid in approximately 3 hours experiment time. This would mean for a 2 μl sample a 300 hour experiment would be required.

In the context of microfluidic lab-on-a-chip (LoC) systems, where the available volumes are much smaller, NMR spectroscopy is less widespread. The flexibility of lithographic microfabrication makes it possible to grow cells, tissue samples, and micro-organisms in controlled environments that closely mimic in vivo conditions. A broad arsenal of techniques for the growth, selection, sorting, and analysis of cells in LoC devices has become available over the past decade.[16,129]

3.7 The Microfluidic Chip

The work demonstrated in this thesis uses a simple microfluidic chip design. The chip comprises of a sample chamber which is filled via an inlet and outlet channel. The purpose of this chip is to demonstrate the potential sensitivity of the detector. Once this has been established then more complex functionality can be introduced to the chip. Commonly PDMS is used for such devices but for this case PMMA is used. Fabrication methods for making microfluidic devices from thermoplastics such as PMMA have been well established.[130]

A sample chamber is cut from a sheet of PMMA using a laser cutter and filling channels etched into the PMMA surface. This is then sandwiched between 2 further layers of PMMA with holes in the top layer for filling the chip (Figure 3.1).

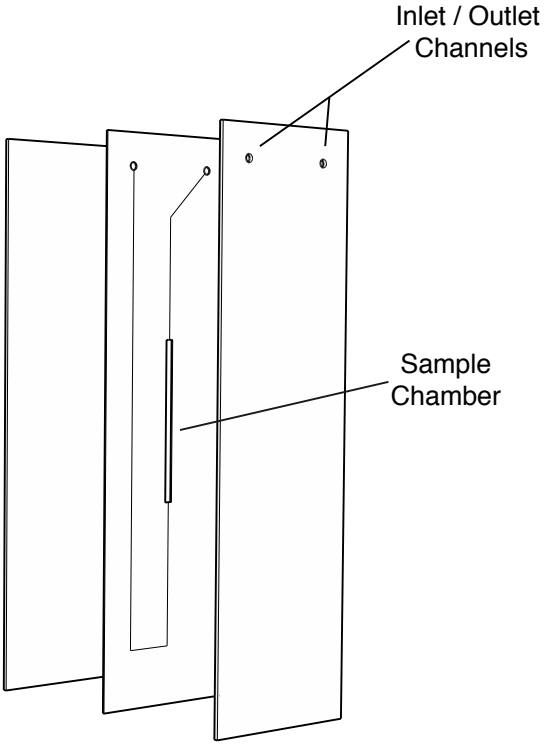

Figure 3.1: Schematic showing the layers of the standard microfluidic chip

Original chips were bonded using a layer of adhesive tape between each layer of PMMA. This allowed for quick manufacture of microfluidic chip prototypes. A 0.2 mm central PMMA layer was used with 2×0.1 mm layers of adhesive tape creating a sample chamber with approximately 0.4 mm thickness sandwiched between two 0.2 mm PMMA layers. This design was not biocompatible, so for later chips thermal bonding was achieved using oxygen plasma exposure, addition of DBP plasticiser and a heated press to bond the PMMA layers directly. A central PMMA layer of 0.5 mm thickness was used for this purpose giving a slightly larger filling factor.

The biocompatibility of PMMA as a surface for cell growth has been previously established in unpublished work by our group. This is confirmed in metabolic experiments conducted in these chips and can be seen in Figure 5.9.

Chapter 4

Planar Microcoils

4.1 Introduction

Previous work by Ryan et al.[2] has demonstrated that inductively-coupled planar resonators can allow high-resolution NMR on microfluidic devices. These microcoils are self-resonant at a specific frequency dependent on their geometry and slight variations in geometry, such as the gap between the turns in the coil or the width of the copper track, can cause the resonant frequency of the coil to be altered. If an accurate method of simulating these coils can be developed then the resonant frequency of different coil geometries can be predicted. Further to this, by simulating coils of different geometry that resonant at the desired frequency, an optimised design can be developed to maximise the sensitivity of these coils.

Pairs of planar Helmholtz micro coils can provide greater magnetic field homogeneity and improved sensitivity to some microfabricated solenoidal micro-coils.[51] The planar spiral microcoil design has also been used for magic angle spinning NMR.[131]

Planar spiral coils can be fabricated using lithographic techniques, as well as by etching of copper laminated polyimides,[2] or by functional ink-jet printing.[48,132] These planar structures can be integrated much more easily with planar microfluidic structures,[2,133,56,134,135] and so are a design that would be practical to use for detection of metabolites on a lab-on-a-chip. However sensitivity in these structures is lower than for micro solenoids,[49] so this is a property that will need to be improved in order for the proposed device to be useful. Self-resonant planar micro-coils do not require a physical connection to the NMR

probe circuit. This 'contactless' NMR spectroscopy means that a microfluidic chip with built in coil could be easily inserted and removed from the spectrometer.[2]

We have developed a method for accurately predicting the resonant frequency and efficiency of planar microcoils. Using a finite element model with a perfect conductor boundary condition it is possible to make these calculations in a way that is computationally efficient. High quality microcoils that are tuned to the required resonant frequency can then be made for high-resolution microfluidic NMR spectroscopy.

Inductive coupling is advantageous for small samples, avoiding electrical leads to the detector which would lead to magnetic susceptibility broadening. Inductively coupled planar microcoils are suitable for microfluidic NMR as they have a thin structure enabling use in spatially confined configurations. They are easily integrated into a microfluidic device and can be positioned close to the sample ensuring maximum sensitivity. NMR spectra can be obtained by inserting the device into a spectrometer. A planar microcoil design is practical for fabrication and integration into a microfluidic device but also important to maximise the B_0 magnetic field homogeneity. By using a planar design, there are no magnetic susceptibility boundaries caused by the coil that are in the same axis as the sample. This means that the sample is minimally affected by such susceptibility boundaries.

The dimensions of the coil will determine the properties of the device such as resonant frequency and efficiency. By modelling the coil at high frequency we can also accurately predict the current density of the coil and the magnetic field surrounding it. Being able to predict the resonance frequency and efficiency of coils is important for their design and optimisation. This information can then be used to make high quality microcoils that can provide the high resolution required for microfluidic NMR.

4.2 Simulation

Resonant frequency can be calculated using the finite element method. This is a numerical technique that divides a model into components (or elements) in order to approximate a solution to differential equations.

The simulation departs from Maxwell's equations:

$$\nabla \cdot \mathbf{D} = \rho(\mathbf{r}) \tag{4.1}$$

$$\nabla \cdot \mathbf{B} = 0 \tag{4.2}$$

$$\nabla \times \mathbf{E} = -\frac{\partial \mathbf{B}}{\partial t} \tag{4.3}$$

$$\nabla \times \mathbf{H} = \mathbf{J} + \frac{\partial \mathbf{D}}{\partial t} \tag{4.4}$$

D is the electric displacement field, ρ is the free electric charge density. **B** is the magnetic flux density, **E** is the electric field, **H** is the magnetic field and **J** is the free current density.

In order to solve these equations for a given geometry, it is necessary to know the relationship between the electric field and the displacement field, as well as the relationship between the magnetic field and the magnetic flux density:

$$\mathbf{D} = \epsilon_r \, \epsilon_0 \mathbf{E} \tag{4.5}$$

$$\mathbf{B} = \mu_0 \mathbf{H} \tag{4.6}$$

ϵ_r is the relative permittivity and ϵ_0 is the vacuum permittivity. μ_0 is the vacuum permeability.

The proton Larmor frequency in a 14.1T magnetic field is approximately 600MHz. At this frequency current is restricted to a small area at the surface of the coil due to the skin effect.

Simulation of resonators at high frequency is challenging due to the spatial resolution required to model this skin effect. Brute-force finite element computation requires element sizes below the skin depth (a few μm) leading to unmanageably large meshes. We make use of the perfectly conducting surface approximation:

$$\mathbf{J} = 0, \text{everywhere but on surfaces} \tag{4.7}$$

The resonant structure is represented by a perfectly conducting surface, and is surrounded by a perfectly conducting sphere of a dimension large enough to observe the

magnetic and electronic fields surrounding the detector (Figure 4.1). The only currents in the problem are restricted to the surface of the conductor. This is a good approximation of the skin effect if the conductor is large compared to the skin depth. The surface of the coil is treated as a perfect conductor meaning that the magnetic field may not have a component perpendicular to the surface:

$$\mathbf{n} \cdot \mathbf{H} = 0 \quad \text{on coil or sphere surface.} \tag{4.8}$$

Combining the constitutive relations with Maxwell's equations, we obtain the homogeneous Helmholtz equation for $\mathbf{E}(\mathbf{r})$:

$$\nabla^2 \mathbf{E} + \frac{\omega^2}{c^2} \mathbf{E} = 0 \tag{4.9}$$

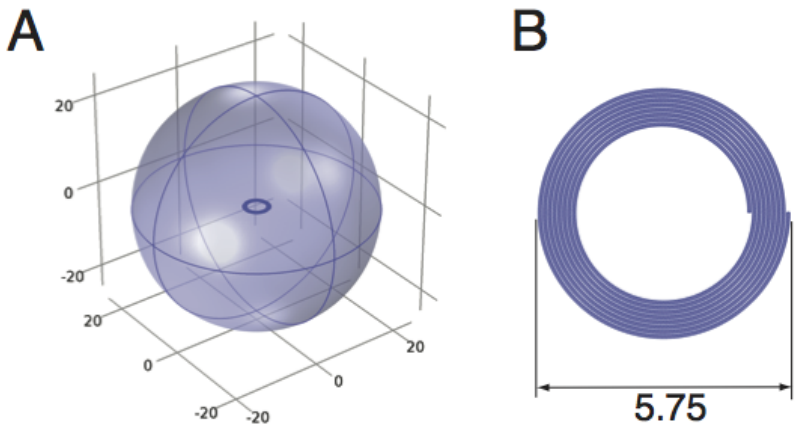

Figure 4.1: A: Image of the simulation structure, with self-resonant planar coil surrounded by a conducting sphere. B: Detailed view of a meshed could with 5.75mm outer diameter and 8 turns.

The number of elements in the computation is controlled by a finite element mesh of tetrahedrons. The mesh must be fine enough on the surface of the resonance structure to capture proximity effects, but can be decreased away from the conductor. Finite Elements Analysis is computationally demanding. The perfect conductor boundary condition is necessary to reduce the computing power required. 4.10 gives an approximation for the skin depth:

$$\delta = \sqrt{\frac{2\rho}{\omega\mu_r\mu_0}} \tag{4.10}$$

Where ρ is the resistivity, ω is the angular frequency of the current, μ_r is the relative magnetic permeability of the conductor, and μ_0 is the permeability of free space. By approximating the skin effect with a perfect conductor boundary condition, calculations can be made without the need to find the relative permeability of the conductor.

Prediction of the resonance frequency of a coil requires solving 4.9 subject to the boundary condition 4.8. This is an eigenproblem with the eigenfrequency ω. In general, a given geometry gives rise to a discrete *spectrum* of eigenmodes. The finite element simulation is used to calculate the frequency of the first resonant eigenmode, along with the corresponding distribution of the magnetic and electric field amplitudes.

The optimisation parameters for this study are the outer diameter of the coil and the total number of turns in the coil. This is to match up with experimental data previously collected.

Eigenfrequencies are calculated by solving the homogeneous vector Helmholtz equation subject to the perfect conductor boundary condition. The finite element simulation gives the first resonant eigenmode. The volume around the coil and the coil surface are meshed as the fields inside the conductor do not need to be modelled. The mesh does not need to resolve skin depth reducing computational demand.

Convergence experiments were carried out to observe the effect of mesh size. A coil with a diameter of 5.75 mm and 8 turns was used for these calculation. Maximum element sizes between 0.045 and 0.105 mm were used, giving between 102350 and 344224 elements. The mesh size was incremented systematically and the resonant eigenfrequency value calculated for each mesh size.

Experimental results were taken from previous work conducted by Ryan et al. Resonance is observed experimentally by resonant interference with mutually decoupled loops. Experimental measurements are obtained from Cu/PI coils.[2]

4.3 Materials and Methods

Simulations were performed using COMSOL Multiphysics software (COMSOL Inc., USA) with the RF module. The model of the coil was generated using parameters of track width (wt), outer diameter (od), track separation (ts), number of turns (nt), copper thickness (hc), surrounding sphere diameter and maximum element size.

The coil geometry was defined using two planar spirals which were then connected to convert to a solid 2D shape. The expressions for the two spirals were as follows:

$$\text{x coordinate spiral 1;} \quad (\tfrac{od}{2} - (wt + ts)s)\cos(2\pi s) \quad ; 0 \leqslant s \leqslant nt \tag{4.11}$$

$$\text{y coordinate spiral 1;} \quad (\tfrac{od}{2} - (wt + ts)s)\sin(-2\pi s) \quad ; 0 \leqslant s \leqslant nt \tag{4.12}$$

$$\text{x coordinate spiral 2;} \quad (\tfrac{od}{2} - wt - (wt + ts)s)\cos(2\pi s) \quad ; 0 \leqslant s \leqslant nt \tag{4.13}$$

$$\text{y coordinate spiral 2;} \quad (\tfrac{od}{2} - wt - (wt + ts)s)\sin(-2\pi s) \quad ; 0 \leqslant s \leqslant nt \tag{4.14}$$

The 2D spiral was then extruded by hc to create a 3D object.

Boundary conditions were then set for the model. All surfaces were set to be perfect electrical conductors and the area surrounding the coil set to have the electric permeability, permittivity and electrical conductivity values of air . The model was set to solve the electric wave equation. A finite element mesh was generated using the maximum element size. The study used a MUMPS eigenvalue solver.

4.4 Results and Discussion

A convergence experiment was run to find the optimum element size for the simulation experiments. Element size was decreased with the idea that at a certain point the resolution would be sufficient to completely accurately simulate the coil. Results from the convergence experiment (Figure 4.2) show that as element size is decreased the resonant frequency is increasing. Convergence is not reached, however by extending

the trend to a maximum element size of 0 mm the potential margin for error can be established.

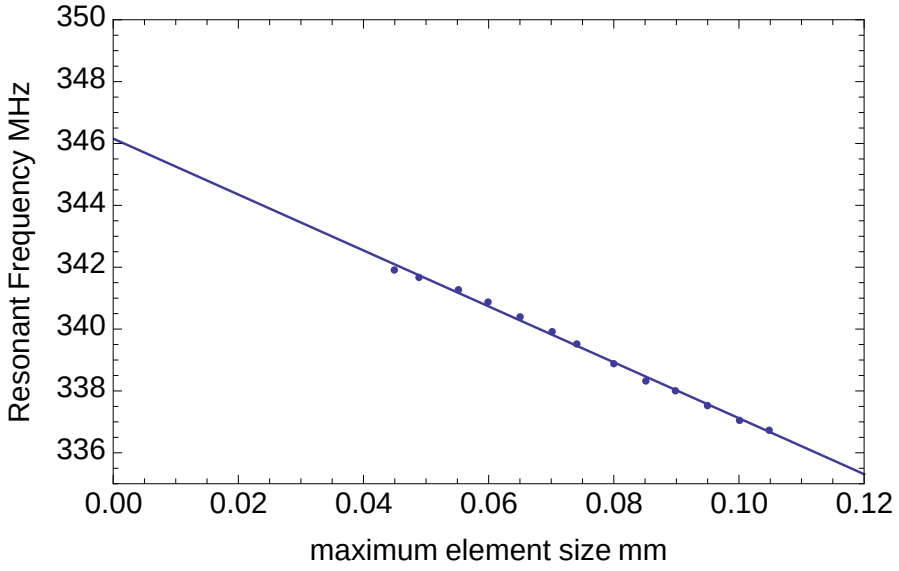

Figure 4.2: Convergence data for 5.75mm coil with 8 turns

As the maximum element size decreases the number of elements greatly increases, increasing the computational demand with it. For this reason it was decided that an element size of 0.065 mm (approx. 200000 elements) would be used for the remaining calculations. Assuming a linear trend in resonant frequency increase as maximum element size decreases then for this coil dimension there is an error of approximately 6 MHz, or 2% in the calculations. It is expected that the trend is not linear but will converge and plateau at some point between 0 and 0.04 mm. The error margin of 6 MHz is taken as a worst-case scenario. A maximum element size of 0.065 mm gives an optimum between accuracy of calculation and short experiment time. Simulations for 200000 elements take approximately 15 minutes to calculate using the university supercomputer system, where the simulations for over 300000 elements take 2 hours or longer, making the possibility to run many simulations impractical.

Results show that the calculated resonance frequencies match the measured frequencies to good agreement (Figure 4.3). It is expected that any major differences between experimental and simulated values comes as a result of faults in fabrication. The perfect conductor simplification is sufficient to provide accurate predictions while reducing the number of calculations required. This shows that the finite element method can be used

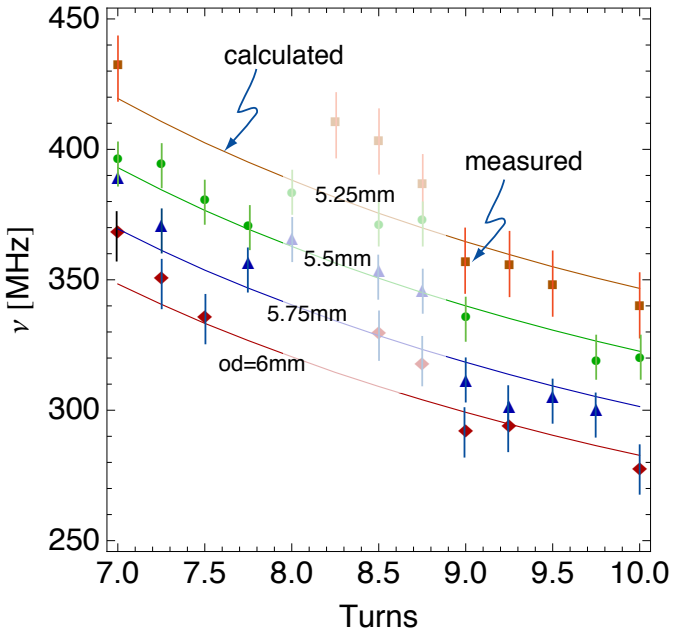

Figure 4.3: Calculated and measured resonant frequencies for coil diameters with varying no. turns.

to calculate frequencies of planar micro coils, meaning that the dimensions of the coil for a desired resonant frequency can be determined before fabrication.

Applying a perfect conductor boundary condition also gives the distribution of surface currents (Figure 4.4C). The surface current density distribution is as would be expected, indicating that the perfect conductor boundary condition is a good approximation to the skin effect that is observed at high frequency.

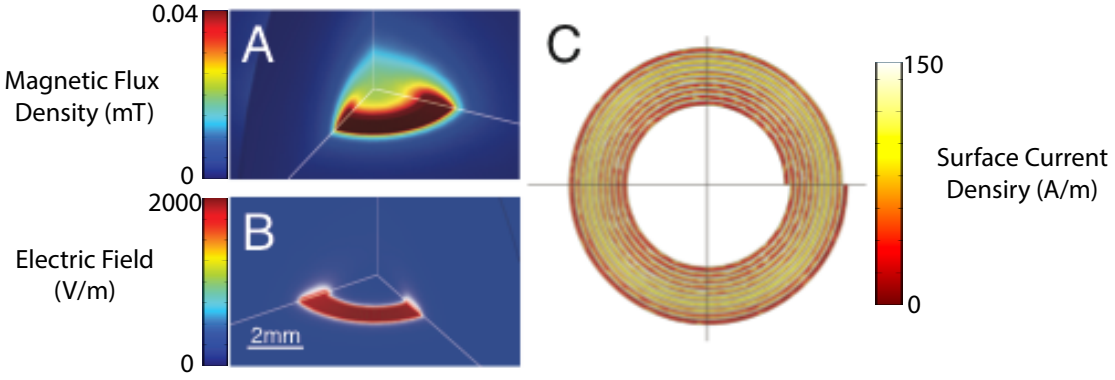

Figure 4.4: A: Quadrant projection of the magnitude of the magnetic field corresponding to the first resonant eigenmode of the coil. B: Magnitude of the electric field. C: Surface current density of the coil

Figure 4.4 shows the magnitude of the magnetic and electric fields, obtained from the calculation. The magnetic field amplitude at the centre of the coil is used to calculate

the efficiency of the coil as is shown late in Equation 4.18.

4.4.1 Optimisation of Planar Microcoil Design

As can be seen from the calculated resonance frequency values (Figure 4.3), it is possible that coils of different dimension may have the same resonant frequency. When designing coils it would be beneficial to know which coil dimensions will give the best signal. The sensitivity is related to the efficiency of the coil so by calculating this we can indicate the optimum coil dimensions.

Methods for estimating losses and signal-to-noise ratio in planar inductive micro coils have previously been demonstrated,[49] however it makes sense to combine this estimation with the calculations for resonance frequency already being made.

Other parameters (including track width and track separation) are fixed, although it may be interesting to see how these would affect the efficiency of the coil in order to further optimise the coil design before manufacture.

Calculated resonance frequency values (Figure 4.3) show that a planar microcoil with more turns or a larger diameter will have a lower resonance frequency. This indicates that there is a negative correlation between the track length of the coil (the length of copper in the coil if it were to be unwound) and the resonance frequency. This can be used to predict coil dimensions which will resonate at approximately 600 MHz.

Coil length (L) is calculated using the following formula:

$$L = 2\pi(\frac{od}{2} - \frac{tw}{2})nt - \frac{tw + ts}{2}nt^2 \tag{4.15}$$

Where od is the outer diameter of the coil, tw is the track width, ts is the track separation and nt is the number of turns.

Using the finite element method described previously it is possible to calculate the efficiency of these coils. Coils with greater efficiency will be more sensitive.

The perfect conductor boundary condition gives rise to a surface current density $\mathbf{j}_s(\mathbf{r})$. Integration of $\mathbf{j}_s^2$ over the surface yields the total surface current I_s, which provides the dissipated power (P_L) together with the surface resistance (R_s):

$$R_s = \sqrt{\frac{\omega\ \mu_0}{2\ \sigma}}. \tag{4.16}$$

$$P_L = \iint_S 0.5\ j_s^2\ R_s\ dS \tag{4.17}$$

P_L is the power that is lost due to resistance, as heat. This allows the calculation of the probe efficiency η using equation 4.18:

$$\eta = \frac{B}{\sqrt{P_L}} \tag{4.18}$$

The conserved power (P_C) is the power that is converted to magnetic field:

$$P_C = \iiint_V \frac{\omega\ \mathbf{B}^2}{\mu_0}\ dV \tag{4.19}$$

Q factor is calculated for these coils by the ratio of the conserved power to the dissipated power:

$$Q = \frac{P_C}{P_L} \tag{4.20}$$

Initially a prediction was made as to which dimensions of planar microcoil would resonate at 600 MHz. This was done empirically by applying a factor of $1 + \frac{od}{c}$ to the coil length of previously calculated resonance frequencies, where *od* is the outer diameter of the coil and c is a constant used to fit the data. This could then be solved to find the different combinations of outer diameter and number of turns predicted to provide this frequency.

Efficiency was then calculated for these coils by using finite elements analysis to solve the homogeneous vector Helmholtz equation subject to the perfect conductor boundary condition, as with the eigenfrequency calculation. The perfect conductor boundary condition also gives the distribution of surface currents. As well as this, the simulation gives magnetic and electric field amplitudes. By modelling the magnetic field amplitude we can also indicate the coil efficiency. Efficiency is calculated from the amplitude of the magnetic flux density at the centre of the coil.

Figure 4.5 shows the fit of the calculated resonance frequencies, used to predict coil dimensions that will resonate at 600 MHz.

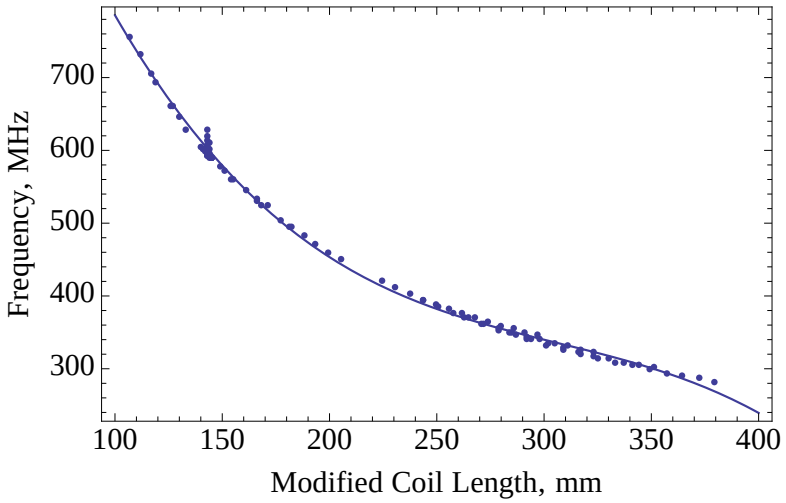

Figure 4.5: Resonance frequencies of planar microcoils with coil length modified in order to provide a fit.

In order to fit, the coil lengths were multiplied by a factor of $(1+\frac{od}{4})$. The fitted function was solved to give the number of turns and outer diameters of coils predicted to resonate at 600 MHz. (Figure 4.6)

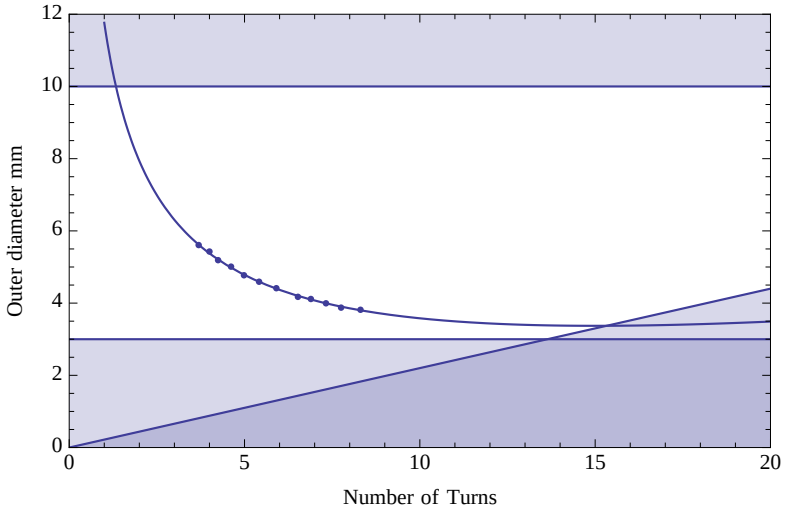

Figure 4.6: Possible dimensions of planar microcoils with a resonance frequency of 600 MHz. Shaded areas depict areas of geometrical (diagonal line) and self-imposed (horizontal lines) constraints, points are the dimensions that were tested.

The curve shows coil dimensions that are predicted to resonate at 600 MHz. The horizontal lines at 3 and 10 mm are self-imposed constraints to show coil sizes that would not be feasible for our purposes, and the diagonal line shows the geometrical constraint

where it would no longer be possible to build coils of this dimension. For example, with a coil of 2 mm outer diameter it is not possible to fit in 10 turns of the coil.

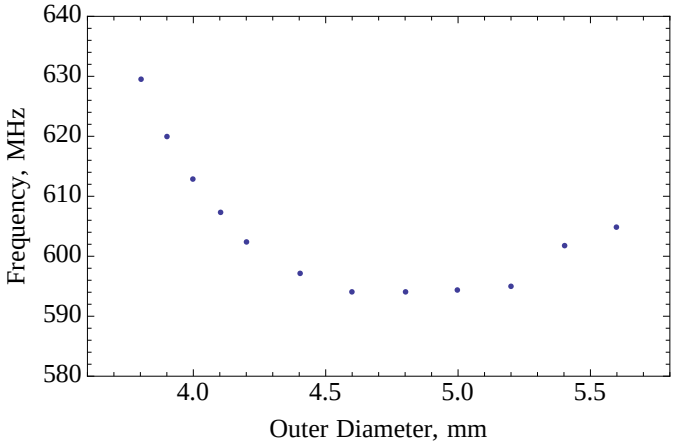

Figure 4.7: Calculated frequencies of coils predicted to resonate at 600 MHz.

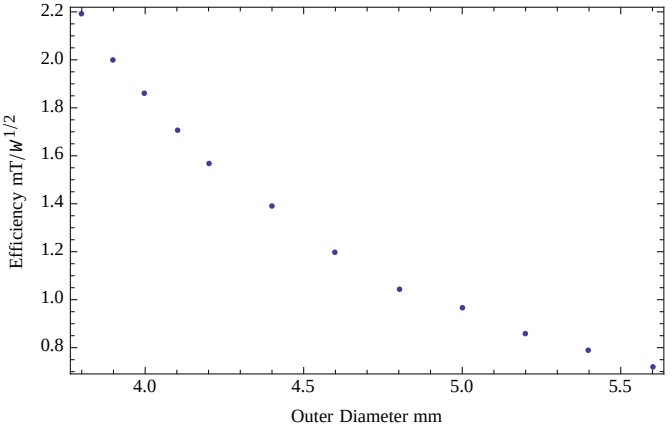

Figure 4.8: Efficiency of coils with resonant frequency of 600 MHz. The number of turns for each diameter was changed in order to match those in Figure 4.6.

Included in Figure 4.7 are the resonance frequencies of the coils that were predicted to resonate at 600 MHz. It can be seen that there is some deviation, from the 600 MHZ predicted, in the calculated results.

The efficiencies of the coils shown in Figure 4.6 were then calculated (Figure 4.8). The coils shown above yield values between 0.12 and 0.18 $\mathrm{mT}/\sqrt{\mathrm{W}}$. For protons, this corresponds to $5 \ldots 7\ \mathrm{kHz}/\sqrt{\mathrm{W}}$. Experimental value: $7.83\ \mathrm{kHz}/\sqrt{\mathrm{W}}$.[2]

These results show that smaller coils with more turns have greater efficiency than larger coils which resonate at the same frequency. These efficiencies are of an order of magnitude greater than those predicted when calculating the initial resonant frequencies. This shows that the optimisation step is worthwhile in the design of these planar micro coils.

The coils exhibit an experimental quality factor up to 60. The same value is obtained by analysis of the surface current density pattern, based on the nominal bulk conductivity of Cu.

From the field map of the B_1 field (Figure 4.9), it can be seen that the areas at the top and bottom of the coil have a lower B_1 field amplitude. This is because transverse magnetisation is created when the current is parallel with the static magnetic field. This means that the magnetic field generated by these coils will not be entirely homogeneous.

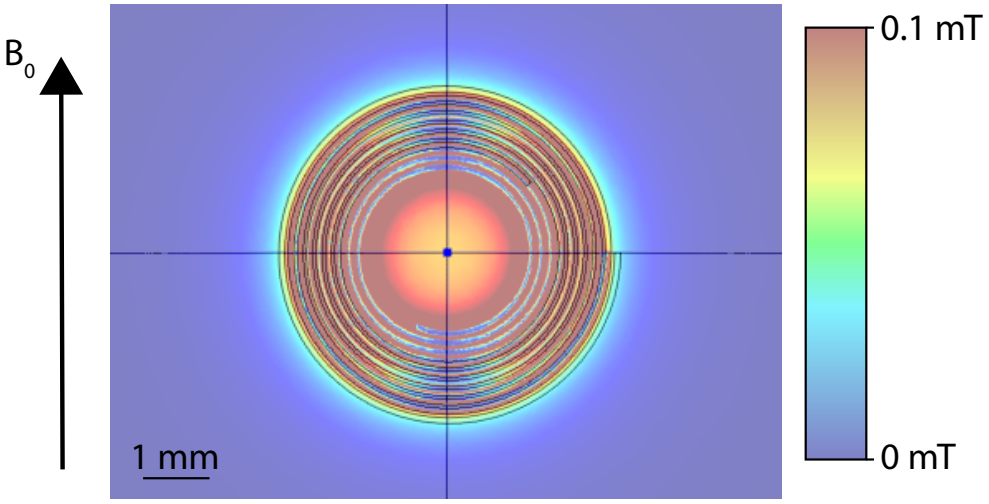

Figure 4.9: Field map of the B_1 field amplitude in a planar microcoil

This design was not pursued because of the difficulties in manufacture. Due to the small feature sizes (track width 0.07 mm and track separation 0.04 mm) lithographic manufacture of these designs is challenging. Despite the photoresist layer protecting the surface of the microcoil during etching, by the time the copper from the gaps was etched away some of the copper had been etched from the sides of the channels. This over-etching creates cracks in the coil meaning that they do not resonate at the desired frequency. In addition to this, the frequency at which inductively coupled planar microcoils resonate is defined by their geometry and is very hard to tune and match. The combination of these two factors lead to the decision to pursue another design.

Chapter 5

Prototype Stripline Design

We present a novel double-stripline NMR probe head that accommodates planar microfluidic devices, and obtains the NMR spectrum from a rectangular sample chamber on the chip with a volume of a few μl. The sensitivity and efficiency of this system are characterised, and its ability to follow changes in the exometabolome of a microfluidic culture of less than 5000 human adenocarcinoma cells is demonstrated.

5.1 Stripline NMR

Planar, linear detector geometries using a single current path have been suggested. These include the stripline,[53,136,54,137] microstripline,[55,138] and microslot detectors.[68,139]

When a current is passed through a straight wire that is placed parallel to a magnetic field, the magnetic component of the radio frequency field that is generated will be perpendicular to this field and can excite NMR transitions.[54] This translates well to the stripline, a flat conductor with a constriction to increase current density. If placed vertically in the NMR probe, the current passing through the stripline will be parallel to that of the external magnetic field. Therefore the entire magnetic field generated will be perpendicular to the B_0 field, enabling efficient manipulation of nuclear spins.

An infinitely long metal wire placed parallel to the B_0 magnetic field will not affect the magnetic field homogeneity. For a finite length wire the homogeneity is not greatly affected in the area of sample detection as long as the distance between the sample from

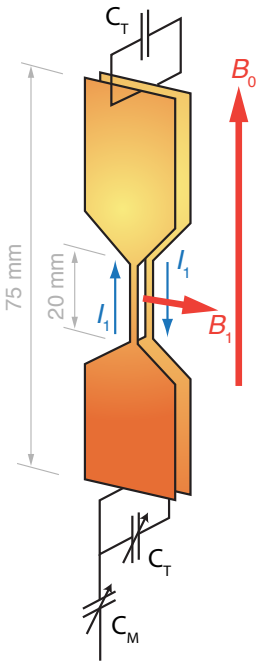

Figure 5.1: Diagram of double stripline configuration showing current I_1 flowing antiparallel through the two conductors. Capacitors at the top and bottom of the plates are used for tuning (C_T) and a variable capacitor is used for matching (C_M)

the wire is much smaller than the length of the wire. In microfluidics it is beneficial to place the sample as close to the detector as possible anyway so this is not an issue. As before, this behaviour will also apply to a stripline meaning magnetic field homogeneity will be good for this design.[54]

In most cases a standing wave is excited in the conductor, which has a length of half the wavelength at Larmor frequency. A constriction is located close to the sample in order to maximise the B_1 field. This constriction is located at the current antinode of the standing wave. These structures are more easily fabricated and offer better filling factors than micro solenoids, as well as improved homogeneity.

A constriction in the centre of the transmission line (Figure 5.2A) creates a region of high current density, concentrating the magnetic flux density and therefore focussing sensitivity on the sample area. The detector is attached vertically to the probe, parallel with the B_0 magnetic field. The constriction and the sample are positioned at a current anti-node of the standing wave mode.[5] This means that the electric field amplitude will be zero, reducing noise.

Van Bentum et al.[53,137] have demonstrated the excellent sensitivity and both high B_0 and B_1 homogeneity offered by planar transmission line resonators. These designs are characterised by a planar conductor which is aligned with the static magnetic field symmetrically between two ground planes. They accommodate a standing electromagnetic wave with a magnetic field anti-node at the centre and nodes at the ends. A constriction at the location of the magnetic field anti-node leads to a concentration of the radio-frequency magnetic field at the location of the sample. While several applications of this type of resonators as flow probes have been described, it has not been adapted to accommodate exchangeable microfluidic devices.

5.2 Planar transmission line design

In the following, an NMR probe assembly based on a variant of the planar transmission line resonator will be described. It accommodates a generic microfluidic chip of dimensions 100 × 25 × 0.8 mm ($l \times w \times h$). The probe is designed such that the radio frequency magnetic field is concentrated on a rectangular sample chamber of approximately 1 mm width and 5 mm length in the centre of the chip. With a chamber thickness of 400 μm, this corresponds to a sample volume of 2 μl. A prototype of the probe was built, and its performance characterised by NMR. As will be discussed in detail below, the resulting sensitivity is sufficient to quantify sub-mM species within a few tens of minutes of measurement time at a static magnetic field strength of 7 T.

Due to the simplicity of the design it is possible to estimate the maximum efficiency of the constricted region of this transmission line detector. From Ampere's Law:[140]

$$\oint_C B \cdot dl \;=\; \mu_0 \iint_S J \cdot dS \;=\; \mu_0 \, I_{enc} \tag{5.1}$$

$$B \;=\; \frac{\mu_0}{2} \frac{I}{l} \tag{5.2}$$

B is the B_1 magnetic field generated by the coil, J is the surface current density, μ_0 is the vacuum permeability and I is the current.

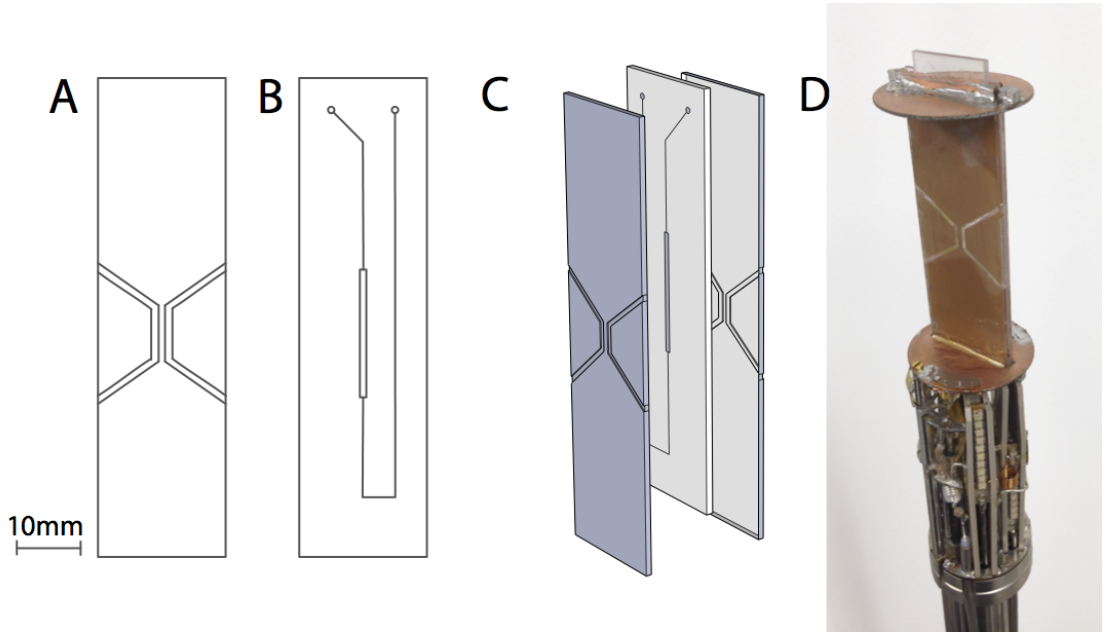

Figure 5.2: A: Diagram of stripline design with narrow region where sample will be located. B: Microfluidic chip designed to correspond with this detector. C: Expanded schematic showing orientation of chip inserted between two stripline resonators. D: Photograph of detector attached to the NMR probe with chip inserted.

Using Equation 4.17 efficiency can be predicted for two rectangular conductors with width (w) and length (l) of the same dimension as the constricted region of the parallel transmission line design, using the following formula:

$$\eta = \frac{\mu_0 I}{\sqrt{w\ l\ I^2\ R_S}} \tag{5.3}$$

η is the efficiency, R_S is the copper resistance.

Which simplifies to:

$$\eta = \mu_0 \frac{1}{w\ l\ R_s} \tag{5.4}$$

For a width of 1 mm and length 6 mm this corresponds to a theoretical maximum efficiency of approximately 4 mT $W^{1/2}$.

The Q factor for these detectors is calculated from the ratio between the resonant frequency and the half-power bandwidth ($\Delta\omega$):

$$Q = \frac{\omega}{\Delta\omega} \tag{5.5}$$

5.3 Materials and Methods

The planar transmission line design was fabricated from single-sided copper-laminated Teflon with a copper thickness of 18 μm (Shenzhen Meidear Co. Ltd., Shenzhen, China). A channel in the copper layer was milled using a micro miller with CNC control (Proxxon, Föhren, Germany) to create the constricted section. The pieces were then cut out from the sheet material using the same milling tool and fixed using cyanoacylate glue (Henkel, UK). The detector was tuned using fixed ceramic capacitors (Johanson, Camarillo, California, USA) and attached to an existing narrow bore probe base (Bruker, Billerica, Massachusetts, USA). The probe base had the previous detection coil removed but the connections to the ^{1}H channel were reused by attaching the stripline coil.

The second generation planar transmission line designs were fabricated by photolithography from copper-laminated polyimide sheet material with a copper thickness of 18 μm (DuPont, Wilmington, USA). The copper layer was coated with a 10 μm layer positive photoresist (AZ9260, AZ Electronic Materials, Germany) by spin coating after cleaning with isopropanol. The desired pattern was created by exposing the photoresist to UV light through a photo mask comprised of photographic emulsion on a polyester base (JD Photo-Tools, UK). The photoresist was developed with AZ400K (AZ Electronic Materials, Germany) solution in water (1:4) and the copper etched using a solution of sulfuric acid, hydrogen peroxide and water (5:21:200). The patterned copper sheet was then fixed to a glass support using cyanoacrylate glue (Henkel, UK).

In order to measure their unloaded resonance characteristics, resonator prototypes were weakly coupled between the ports of a vector network analyser (Agilent, Santa Clara, USA). Eigenfrequency and Q factors were measured from the position and 3 dB points of the peak observed in the S_{12} scattering parameter. The Q values were corrected for finite coupling.[141]

Microfluidic chips were manufactured from PMMA sheets (Nitto Jushi Kogyo Co. Ltd., Tokyo, Japan). The design was created using AutoCAD and then cut with a CO_2 laser cutting system (Epilog, Golden, Colorado, USA). The sample chamber was cut from

0.5 mm PMMA with channels for filling scored into the PMMA surface. Initially the layers were bonded using adhesive tape (Thorlabs, Newton, New Jersey, USA). In later experiments the bonding procedure follows that of Yilmaz et al.[142] Surfaces were exposed to oxygen plasma in a plasma etcher (Diener, Switzerland) and sandwiched between two 0.2 mm PMMA panels and thermally bonded in a hot plate press (Specac, UK) with the help of dibutyl phthalate plasticiser (Sigma Aldrich). This technique improved the biocompatibility of the chips.

NMR spectra were acquired on a Bruker AVANCE III spectrometer equipped with a 7 T Oxford Instruments Wide Bore Magnet.

Nutation diagram was obtained from 50 single scan experiments with a pulse length ranging from 0 to 100 μs each with 16k points.

Field map was created by taking the phase difference between two magnetic resonance images with different echo times. Both images used a field of view of 1.28 cm, and a single sagittal slice with 1 mm thickness. The images were taken with 128 matrix points, a repetition time of 200 ms and 4 averaged scans. The two images had echo times of 6 and 16 ms respectively. Images were processed using Mathematica software by reading the two imaging data sets, returning the complex image. The value of each data point relates to the average of the two spectra, the phase value corresponds to the average of the two phases. Each number is then converted into a colour according to the phase, the brightness represents the magnitude.

1D spectra were obtained using a simple 90° pulse-observe sequence, in some cases with solvent presaturation of 0.1 mW power for 3 seconds and a 128 ms T_2 filter consisting of a spin echo train with suppressed J evolution[143] to suppress interfering signals from larger, slow moving molecules with high molecular weight.[144] The 1D 200 mM glucose spectrum was obtained using a composite excitation pulse[145] to limit the effective sample volume and reduce the water signal from the region outside of the sample chamber. 1D spectra were recorded with a spectral width of 12 ppm, 32k data points and a relaxation delay of 3 s between scans. Test samples were made from 150 mM sodium acetate (Sigma Aldrich) in H_2O, and from Dulbecco Modified Eagle's Medium (DMEM) supplemented with 10% Fetal Bovine Serum (FBS) (Life Technologies, USA). 10 mM 4,4-dimethyl-4-silapentane-1-sulphonic acid (Sigma Aldrich) was added as a chemical shift reference.

All NMR data was processed using Mathematica.

Batch cultures of MCF-7 cells were carried out in T75 flasks (Fisher Scientific UK Ltd.) using 12 ml of growth medium. Cells were maintained as recommended by ATCC, in Dulbecco Modified Eagle's Medium (DMEM) supplemented with 10% Fetal Bovine Serum (FBS) (Life Technologies, USA). All cells were kept at 37°C under 5% CO_2 in an incubator and harvested using phosphate buffer (DSBS, Life technologies, USA) to wash the cells and Trypsin (0.05% Trypsin-EDTA, Life Technologies, USA) solution to detach them. Detached cells were centrifuged at 5000 rpm for 4 minutes. The cells were resuspended in 1 ml of growth serum (DMEM/FBS). Cells used during experimental work were between the 20th and 40th cycles. Around 10,000 cells were cultured in microfluidic devices and kept under optimal conditions for 24 hours for adhesion prior to NMR analysis. 200 μL of fresh growth serum containing 0.01% TMS was added to the chips directly before NMR analysis. After this period, around 5,000 cells remained in the sample chamber. Devices were then sealed to avoid contamination before transferring to the NMR spectrometer. Metabolomic spectra were obtained from 128 scans with an experimental time of approximately 15 minutes. 4 experiments were run before chips were placed back into the incubator (37°C, 5% CO_2) for a period of time.

5.4 Probe Performance

The nLOD was calculated in order that the sensitivity of the detector could be compared with other micro detectors. nLOD has been scaled by a factor of $2^{7/4}$ to make them comparable with detectors designed for a 14.1 T magnetic field. This is only an approximation as it doesn't take into account effects of the magnetic field on relaxation times.[5] In addition, line broadening caused by magnetic field inhomogeneity will scale with the magnetic field and so sensitivity may not turn out quite as high as predicted. This needs to be followed up by further experiments at greater magnetic field strength.

Based on the anomeric protons of glucose, nLOD was of 13.5 nmol $s^{1/2}$, as determined from a 2 μL sample of 0.5 M glucose in D_2O solution. The nLOD was calculated from the signal to noise ratio of the combined peak heights of the α and β-H_1 protons of D-glucopyranose (Figure 5.3A).

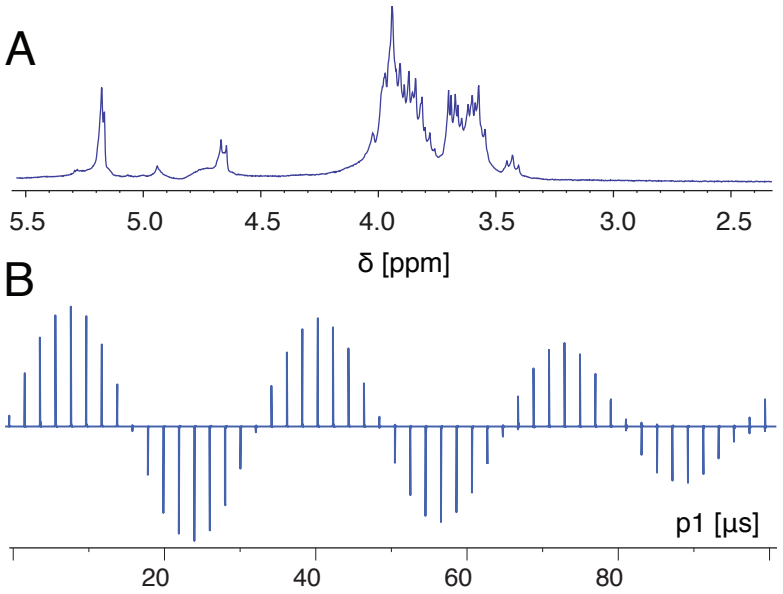

Figure 5.3: A: ^{1}H NMR spectrum of 1 μL of 0.5 M glucose in D_2O. B: Nutation diagram of an array of pulse duration

A previous stripline detector has reported a nLOD of 22.3 nmol $s^{1/2}$ for the sucrose anomeric proton in a 0.6 μL sample volume.[54] A planar micro coil has shown similar sensitivity of 22.2 nmol $s^{1/2}$ from the anomeric protons of glucose in a 1.2 μL sample volume.[2] This shows that sensitivity for our initial detector design is comparable to previously seen results.

The efficiency of the resonator is 0.40 mT $W^{1/2}$. The homogeneity of the radio frequency (B_1) field was characterised using the nutation diagram (Figure 5.3B) from the ratio of peak amplitudes of the 810 and 90 degree pulses. For this design $A_{810}/A_{90} \approx 70\%$, whereas commercial liquid probes are around 80%. The B_0 homogeneity can be seen in Figure 5.4, a field map obtained of the constricted region of the stripline.

In order to achieve the calculated maximum efficiency of 4 mT $W^{1/2}$ a majority of the losses in the detector must come from the constricted region. However, currently there are other areas in the circuit which are of similar diameter to this region, including the capacitors connecting the two conducting plates and the connections to the probe. It may be that losses occurring in other narrow regions are limiting the efficiency of this design. Other potential limits to the efficiency include surface losses from roughness in the copper surface and air spaces between the detector and the chip.

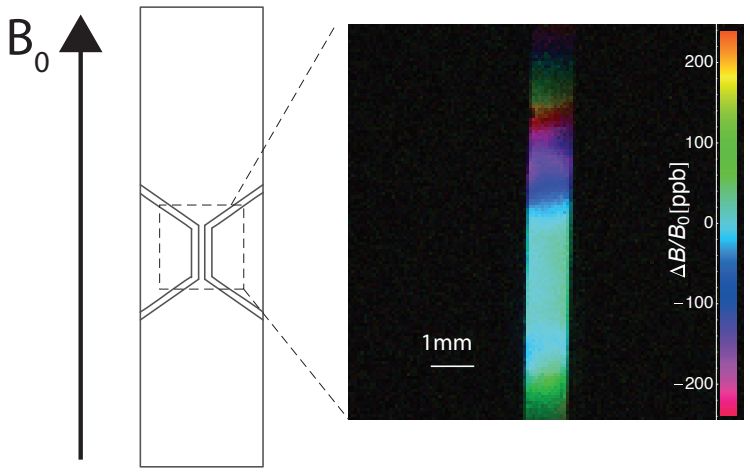

Figure 5.4: Field map of constricted region of stripline

5.5 Second Generation Design

Following on from these results a second detector was designed, using the same overall principles as the first. Some improvements were made in the manufacturing processes in the aim of improving the quality of the obtained spectra. Photolithography was used to create the transmission line in order to minimise the depth of the channels preventing magnetic susceptibility broadening. A longer 10 mm constricted region was used in the hope to further increase the sensitivity. A photograph of the finished detector is seen in Figure 5.5

For this detector the $\pi/2$ pulse length is 9.2 μs at a power of 12.7 W. This corresponds to a probe efficiency of 0.37 mT/W$^{1/2}$.

The nutation diagram for this probe in Figure 5.6 shows an A_{450}/A_{90} ratio of 0.38, and an A_{810}/A_{90} ratio of 0.28. This is much lower than would be found in a conventional setup (usually around 0.8), however after a sharp initial drop in intensity the peak amplitudes level out considerably, indicating that there is a region of the detector in which there is very good homogeneity. It is thought that this is caused by the extremely narrow gap where the constriction is etched from the copper sheet. Although a small gap was intended to reduce magnetic susceptibility broadening it is possible that the magnetic flux density being forced through this narrow gap actually causes increased distrotions in the B_1 magnetic field.

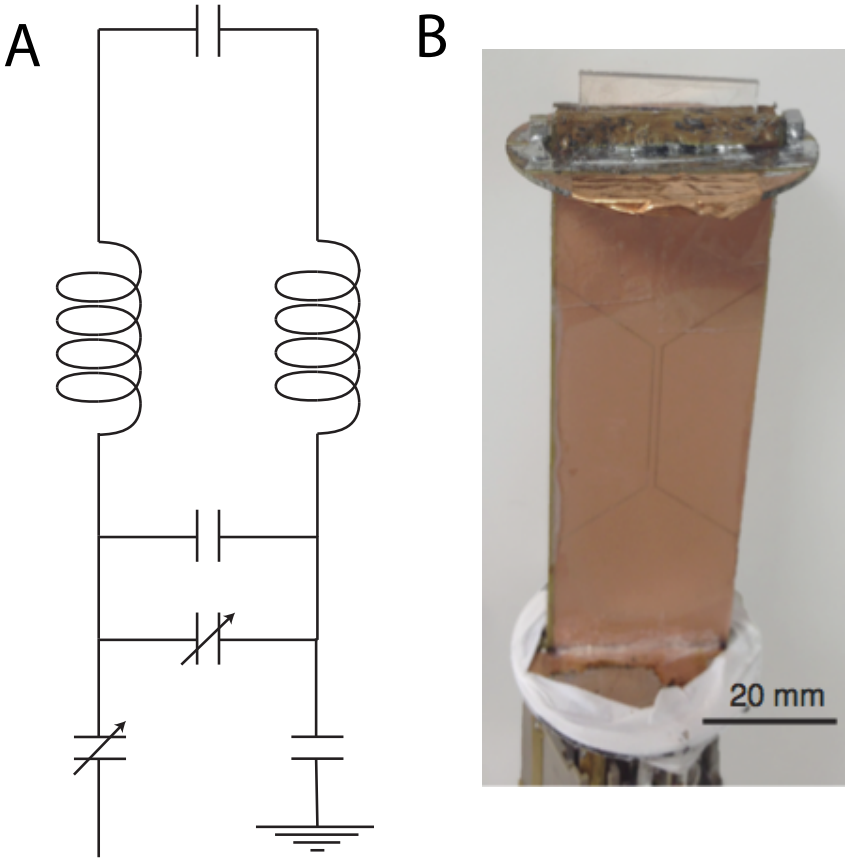

Figure 5.5: Principle of the double stripline detector. A) The electromagnetic oscillator circuit. B) Photo of the microfluidic chip inserted between the two conducting plates connected to the NMR probe base.

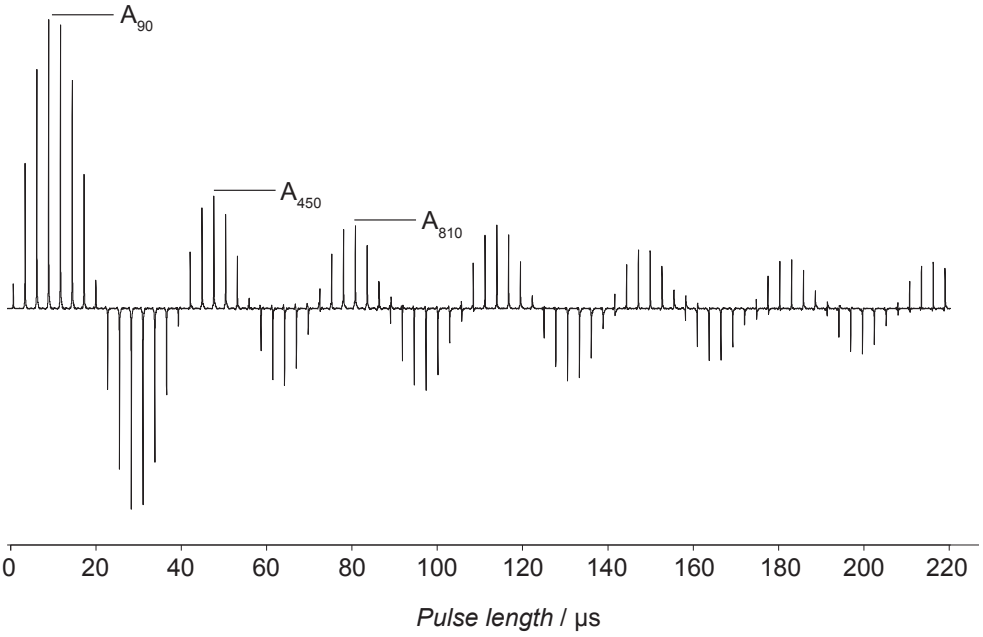

Figure 5.6: Nutation spectrum of the second generation probe.

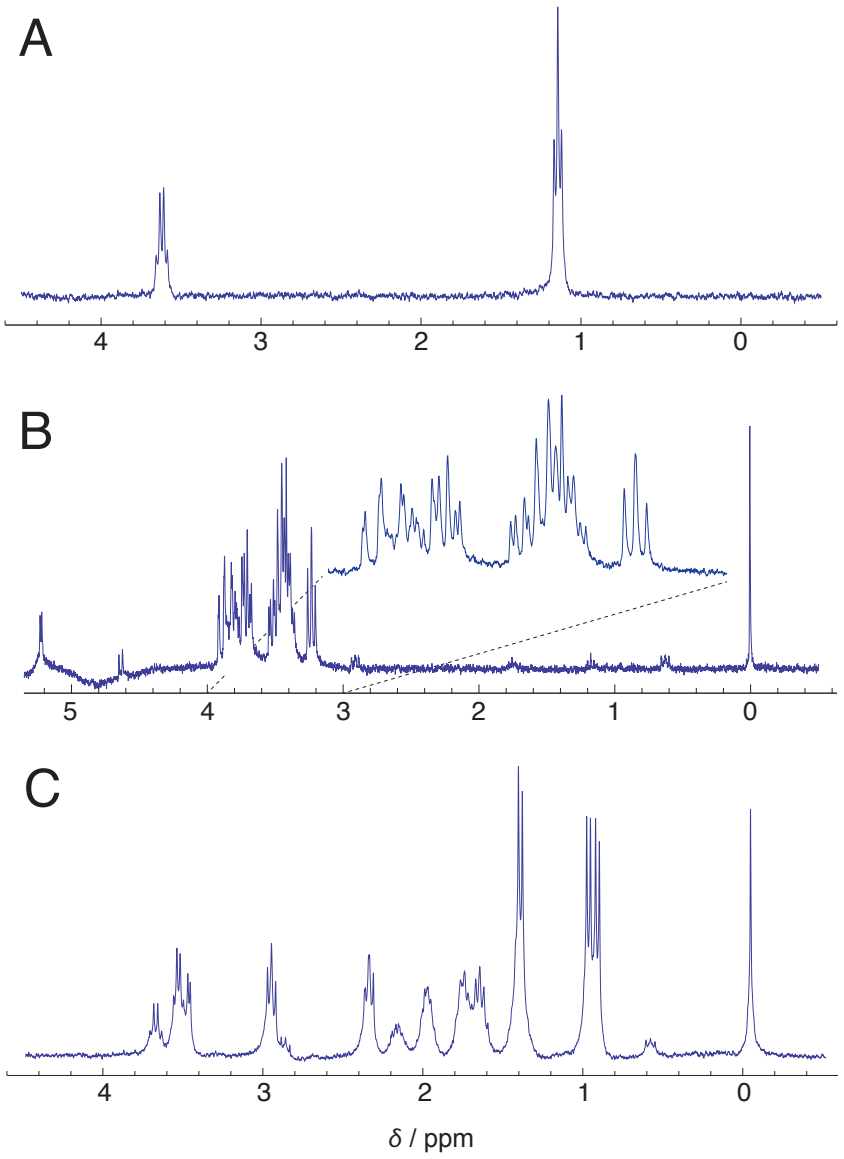

Figure 5.7: ^{1}H NMR spectra of 4 μl of A) 100 mM ethanol in D_2O, aquired over 8 signal averaged scans B) 200 mM glucose in H_2O, 16 scans. Expanded region between 3 and 4 ppm of the same spectrum. C) 5 mM valine, glutamine, lysine and alanine in D_2O, 32 scans.

The performance of this probe system is illustrated by the spectra shown in Figure 5.7. The probe sensitivity and efficiency were assessed using a sample of of 100 mM ethanol in D_2O.

Sensitivity was quantified by the normalised limit of detection in the time domain,

$$\mathrm{nLOD}_t = \frac{3n_s}{\mathrm{SNR}_t\sqrt{\Delta f}}, \tag{5.6}$$

where n_s is the number of spins present in the sample, SNR_t is the signal to noise ratio, and Δf is the spectral bandwidth, defined by the sum of the widths at half height of all lines contributing to the time-domain signal. SNR_t is calculated in the time domain by dividing the point with the largest magnitude of the free infection decay (FID) by the root mean square of twice the noise amplitude.[5] The spectra in Figure 5.7 have been obtained at a magnetic field of 7 T, corresponding to a proton Larmor frequency of $\omega/2\pi = 300$ MHz. It has become customary to report the sensitivity of micro-NMR detectors at a field of 14.1 T ($\omega_0/2\pi = 600$ MHz proton frequency), by scaling the nLOD with a factor of $(\omega_0/\omega)^{7/4}$. From the data shown in Figure 5.7A, we thus obtain

$$\mathrm{nLOD}_t@14\mathrm{T} = 2.0\,\mathrm{nmol\,s}^{1/2}.$$

While the time domain limit of detection provides a standardised test of the detector performance, it is only of limited value in judging the practicality of metabolomic NMR spectroscopy. It does not take into account that NMR spectra are often acquired repeatedly, and SNR is gradually improved through signal averaging. In this case, the required measurement time is determined by the relaxation delay between scans, which must be at least of order of the spin-lattice relaxation time T_1 to ensure accurate results. A more meaningful (and stringent) test of probe performance is therefore given by measuring the limit of detection in the frequency domain for a standard compound which exhibits a T_1 typical of metabolic species; sucrose or glucose are commonly used for this purpose. Figure 5.7B shows a spectrum of 200 mM glucose in H_2O obtained with this probe. The triplet centred at 3.20 ppm, which stems from the H2 proton in the β-glucopyranose anomer, was used to assess sensitivity. The frequency-domain limit of detection is given by

$$\mathrm{nLOD}_\omega = \frac{3n_s\sqrt{\Delta t}}{\mathrm{SNR}_\omega}.$$

From the spectrum shown in Figure 5.7B, we obtain

$$\mathrm{nLOD}_\omega@14\mathrm{T} = 10.6\,\mathrm{nmol\,s}^{1/2}.$$

To put this into perspective, Figure 5.8 compares the sensitivity of 20 different micro-NMR detectors reported in the literature as mentioned earlier on.[5] The probe presented here (red triangle) compares favourably with other micro NMR detectors. For example, a

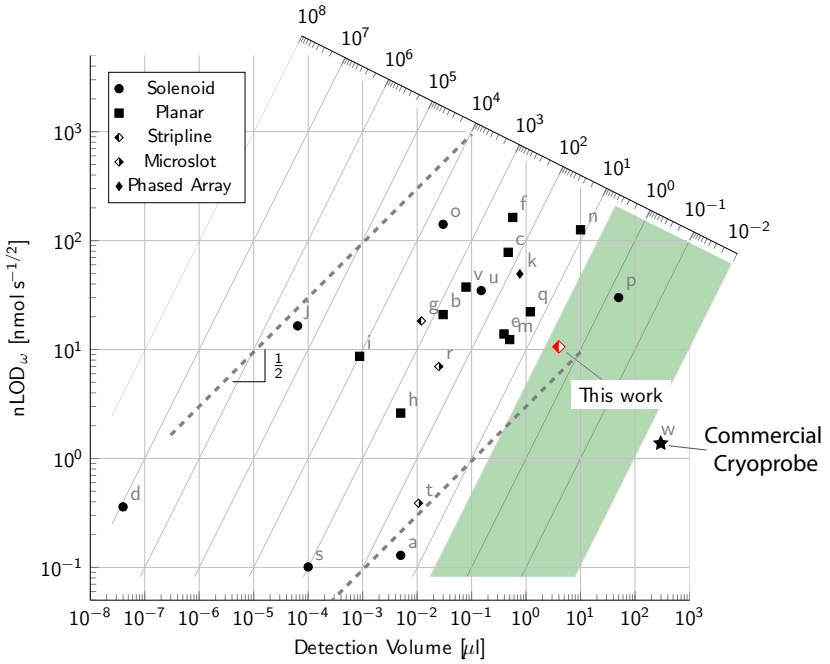

Figure 5.8: Plot comparing sensitivity of previously designed micro-NMR detectors. Letters a-t correspond to different authors as cited by Badilita et al.[5] Data points *u*[6] and *v*[3] represent more recent work. Point *w*[7] refers to a commercial cryoprobe. The performance of the double micro stripline probe presented here is shown in red. (Adapted from Figure 2.7, individual references can be found in Table 2.1.)

stripline design with a smaller sample volume of 0.012 μl affords a nLOD of 18.3 nmol s$^{1/2}$ (data point *g*).[53] Planar detector designs of a similar sample volume 0.4,[56] 0.5,[57] and 1.2 μl[2] also have lower mass sensitivities of 13.8, 12.3 and 22 nmol s$^{1/2}$ respectively (data points *c*, *f*, and *q*). While more sensitive detectors have been reported (e.g, capillary/solenoid or micro-slots), their sample volumes are significantly smaller than 4 μl. In the context of LoC and metabolomics, samples are not only mass limited, but also *concentration* limited; only the most abundant metabolites are typically present at more than 1 mM concentration, and many of them substantially lower.

For practical metabolomics studies, the concentration limit of detection (cLOD) must be at least such that species present at 0.1 mM concentration can be quantified in about 20 min of measurement time. This corresponds to cLOD $\leq$ 5 mM s$^{1/2}$. The area where this condition is satisfied is shaded in Figure 5.8. The detector presented here lies well inside this region, whereas many other micro NMR detectors are not suitable for metabolomics studies, even though their mass sensitivity is superior. For example,

a solenoid detector with an excellent nLOD of 0.1 nmol $s^{1/2}$ has been demonstrated by Seeber *et al.*[146] (data point *s*). However, since the sample volume is only 100 pL, the concentration limit of detection is 1000 mM $s^{1/2}$, insufficient for metabolomics by several orders of magnitude.

Despite comparing favourably with microcoils of similar volume, there is some way to go to compete with a commercial cryoprobe which exhibits an nLOD of 1.32 nmol $s^{1/2}$ in a volume of 300 μl. This cryoprobe performs better both in terms of mass and concentration sensitivity. For cases where sample volume is limited, such as in microfluidic devices then the microcoils may still be preferable. It is important to optimise the coil geometry in order to maximise the sensitivity, and this will be investigated in chapters 6 and 7.

In addition to good sensitivity, the double stripline design also offers reasonably good spectral resolution, as illustrated by the glucose spectrum shown in Figure 5.7B. The resolution is about 2 Hz, enabling observation of multiplets in the NMR spectrum, although with some peak overlap. From the two stripline designs tested so far it can be seen that there is a trade-off between sensitivity and homogeneity. The optimal design can be found by simulation and is explored in Chapter 6.

The spectrum in Figure 5.7B has been obtained using water pre-saturation, in combination with a composite excitation pulse.[145] While this effectively removes the water resonance at 4.8 ppm, it leads to noticeable baseline distortions, which are particularly severe in the spectral region downfield from the water resonance. This is most likely due to the presence of water in parts of the chip that are outside of the focal area of the detector and therefore not exposed to the full radio-frequency field. However, as shown in the following, the water suppression performance, albeit lacking in some respects, is still sufficient to obtain metabolomics-quality spectra in the region upfield from the water signal. Quantitative metabolomic spectra require effective solvent suppression techniques so that metabolite peak amplitudes are accurate. In future work methods of narrowing the water signal will need to be investigated in order that the water signal can be more effectively suppressed.

The ability to analyse mixtures is demonstrated in Figure 5.7C, which shows the spectrum of an aqueous solution of 50 mM each of valine, glutamine, lysine and alanine in

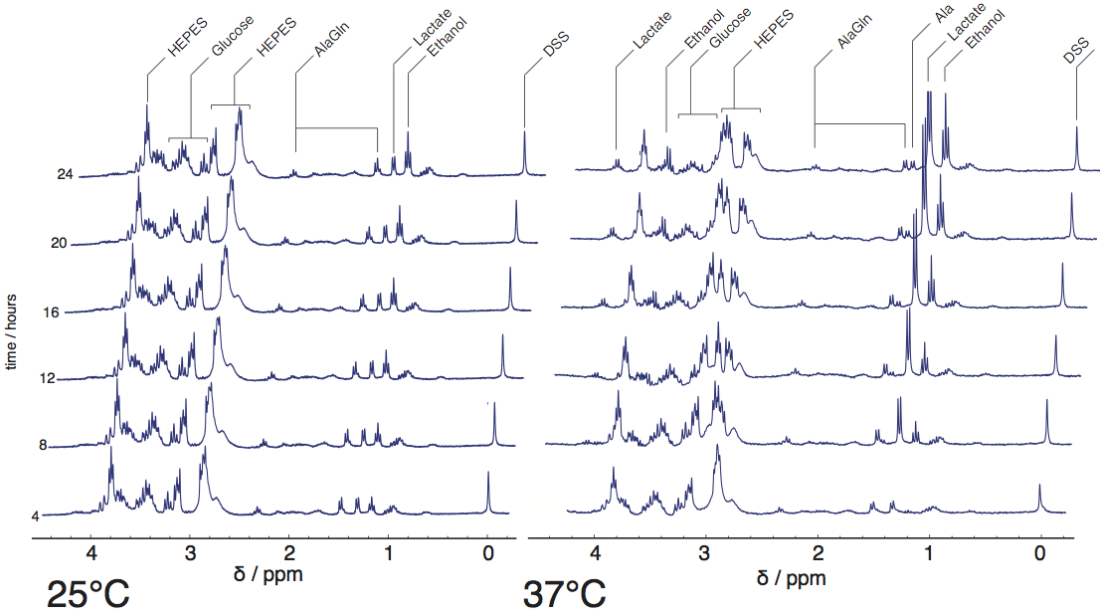

Figure 5.9: Study of MCF-7 cells over a period of 24 hours. Left: cells cultured at 25°C; right: cells cultured at 37°C.

D_2O. The ability to observe these different chemicals within a mixture opens up the possibility for cell metabolomics on a chip.

5.6 Metabolomics

A metabolic study of human adenocarcinoma (MCF-7) cells under hypoxic conditions was undertaken in order to demonstrate the possibility of using this detector for in-situ NMR metabolomics. The cells were seeded onto the microfluidic chip and given 24 h to adhere to the chip surface. Immediately before the start of NMR observation, the medium in the chips was replaced, and the chips were then sealed in order to observe the cell metabolism under hypoxic conditions.

Figure 5.9 shows two time series of ^{1}H spectra obtained over the course of 24 h after the initial seeding period. In one case (Figure 5.9A), the chip was left in the spectrometer for the entire duration of the experiment, thus keeping its temperature at 25°C. In the other case, the chips were kept in an incubator at 37°C in between NMR measurements (Figure 5.9B). In both cases, NMR spectra were recorded over 50 min of acquisition time every 4 h.

Both sets of spectra clearly show a number of gradual changes over time. In both cases, the ethanol concentration appears to increase over time, with a slightly more marked effect at 37°C. This is an artefact due to residual ethanol being leached from the chip into the solution, as confirmed by control experiments with chips that have not been seeded with cells.

Apart from this, the changes in the spectrum obtained at 25°C are minimal, whereas there are very clear signs of glycolysis[147,148] at 37°C, illustrating the much higher metabolic rate at physiological temperature. The growth of the lactate concentration at 37°C is the most obvious one, as evidenced by the doublet at at 1.3 ppm (closer inspection shows a small amount of growth in this peak at 25°C, as well). This indicates that the cells are undergoing anaerobic respiration. In parallel to the formation of lactate, the glucose signals decrease over time; this is most clearly seen in the group of peaks between 3.4 and 3.6 ppm. Also observed is a shift in the glutamine peak from 1.5 to 1.4 ppm. This due to the conversion of the dipeptide L-alanyl-L-glutamine present in the medium to alanine (Ala, observed at 1.4 ppm) and glutamine (Gln). Concurrently, shifts are observed in the signals from the HEPES buffer due to a change in pH. The most intense peak of the HEPES buffer shifts from 2.95 ppm at the start of the experiment to 3.15 ppm after 24 hours. This corresponds to a change in pH from 7.6 to 7.0,[149] illustrating gradual acidosis as a result of the hypoxic conditions.

The conversions of glucose to lactate and alanyl glutamine to alanine can be quantified by peak integration of the NMR spectra, as shown in Figure 5.10. At 37°C, the glucose concentration decreases from an initial concentration of around 25 mM to 3 mM and lactate shows a concomitant increase from 5 mM to 25 mM (Figure 5.10A; solid lines and closed symbols). Since glycolysis produces two molecules of lactate for every molecule of glucose consumed, it therefore seems that some lactate is being used for further biosynthesis. This is corroborated by microscopy, which confirms continuing proliferation and growth of the cells throughout the experiment (see Figure 5.11). At 25°C, lactate production and glucose consumption proceed much more slowly (Figure 5.10A, dashed lines/open symbols).

Figure 5.10B shows conversion of AlaGln to Ala and Gln, which proceeds to about 50% completion at 37°C, while it is not detectable at 25°C.

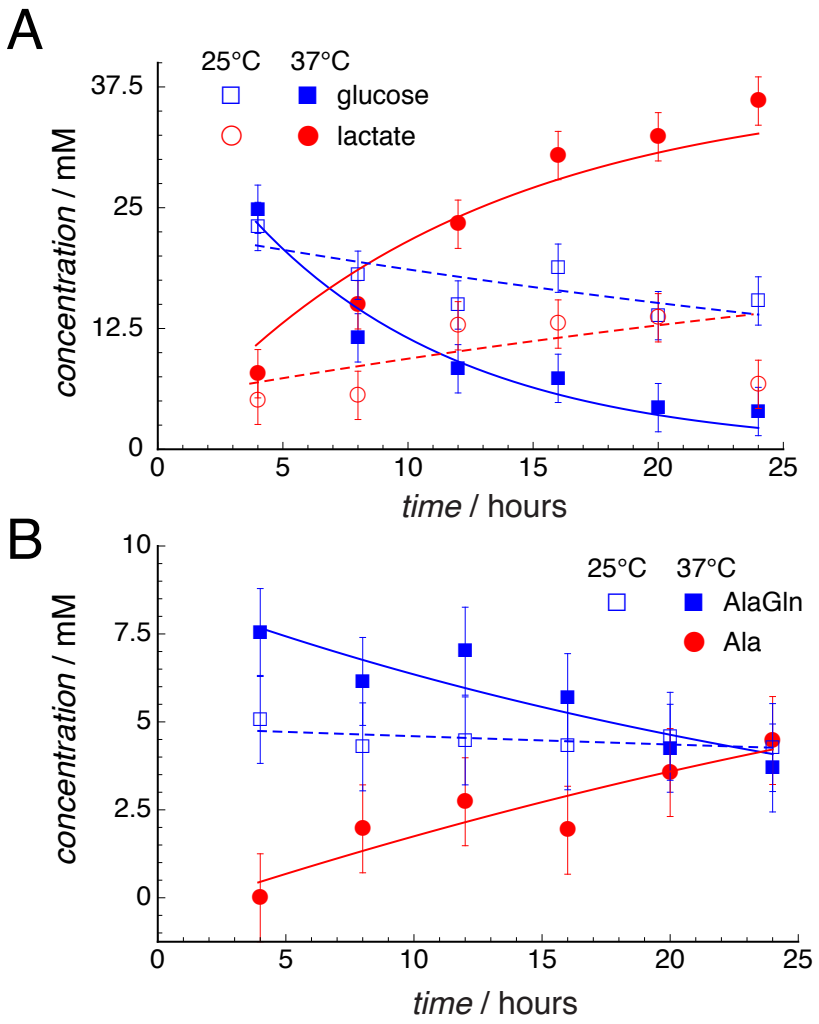

Figure 5.10: Consumption and production of selected metabolites throughout the experiment time.

The second generation probe exhibits similar sensitivity to the first generation design with an efficiency in the original design of 0.4 mT/W$^{1/2}$. This sensitivity allows detection of 0.1 mM concentrations within a 4 μl sample volume in less than 20 minutes of experiment time.

The nutation plots indicate that the second generation design had poor B_1 field homogeneity, this doesn't affect the 1D spectra greatly but could limit the application of this probe for complex pulse sequences. The first probe had good B_1 homogeneity with an A_{810}/A_{90} ratio of approximately 70%, compared to 28% in the second design. It is thought that this is caused by the narrower gap around the constriction in the second generation so this should be altered in future designs. Despite this the spectral

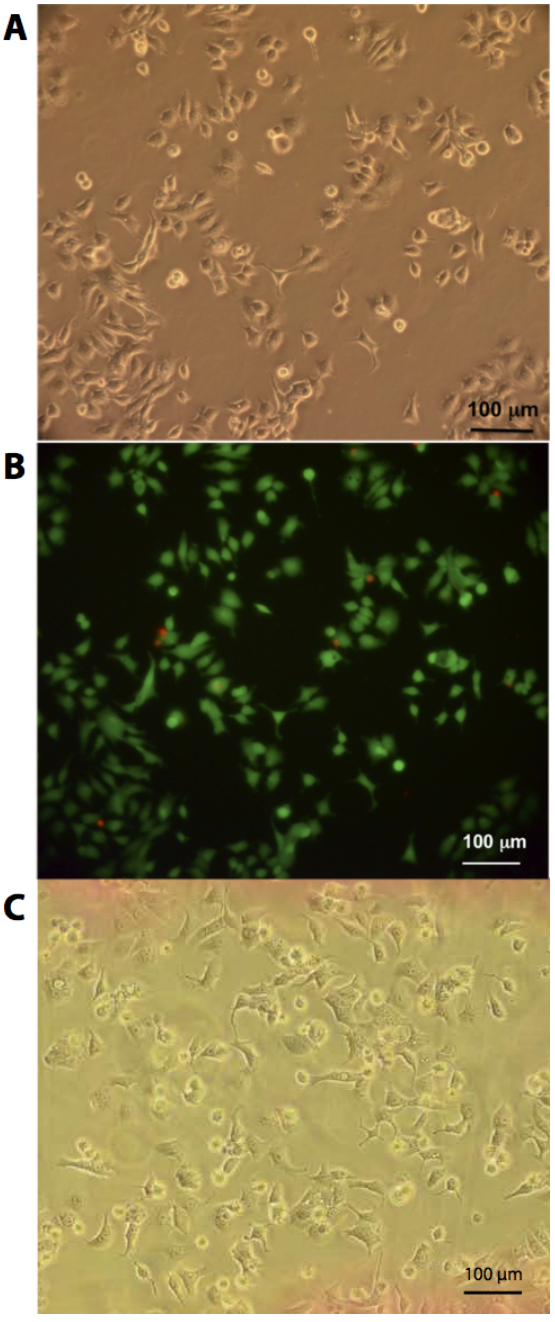

Figure 5.11: A) Light microscopy image of cells 24 hours after seeding. B) Fluorescent image of cells 24 hours after seeding with LIVE/DEAD stain. C) Light microscopy image of cells 48 hours after seeding (red lines at top and bottom of image caused by markers used for cell counting.)

resolution is improved in the second generation, indicating good B_0 homogeneity and this is demonstrated by the narrow linewidths, enabling metabolomic information to be determined.

Chapter 6

Finite Element Simulations

The previous prototype proved that in-situ metabolomic NMR could be performed on a microfluidic chip. In order to further improve the design of the probe finite element simulations were used. Simulations were tested against experimental results and then used to optimise the design to achieve maximum sensitivity whilst maintaining spectral resolution. This would allow similar quality spectra to be obtained in a shorter experiment time, or alternatively samples with lower concentration could be detected in the same time.

6.1 Stripline Simulation

As has been show by Hoult and Richards,[26] the sensitivity of NMR detectors (i.e. the number of spins precessing within a unit bandwidth for a given signal to noise ratio) is related to their efficiency (i.e. amplitude of the resonant B_1 field per square root of the radiofrequency power). Optimisation of one quantity therefore automatically also optimises the other.

A finite element analysis approach is used in order to compute the radiofrequency magnetic and electrical fields in the planar transmission line resonator. This model is based on the Helmholtz equation for the electric field **E**:

$$\nabla^2 \mathbf{E} = \mu\epsilon \frac{\partial^2 \mathbf{E}}{\partial t^2} + \mu\sigma \frac{\partial \mathbf{E}}{\partial t} \tag{6.1}$$

where μ, ϵ, and σ represent the local magnetic permeability, electrical permittivity, and electrical conductivity respectively. Since we are only interested in stationary (standing wave) solutions, the time and spatial dependence of the electric field can be separated as

$$\mathbf{E}(\mathbf{r},t) = \Re(\mathbf{E}(\mathbf{r})e^{-\lambda t}) \tag{6.2}$$

with the eigenvalue $\lambda = \delta - i\omega$, and the Helmholtz equation becomes

$$\nabla^2\mathbf{E}(\mathbf{r}) = (\lambda^2\mu\epsilon - i\lambda\mu\sigma)\mathbf{E}(\mathbf{r}) \tag{6.3}$$

where $\mathbf{E}(\mathbf{r})$ is the complex (magnitude and phase) amplitude of the electric field. Finite element analysis (FEA) modelling of a resonator consists in solving the above non-linear eigenvalue problem given a spatial distribution of the electric conductivity, magnetic permeability, and electric permittivity. Assuming such a solution is found, the complex eigenvalue $\lambda_k = \delta_k - i\omega_k$ then characterises the resonant frequency ω_k as well as the damping coefficient δ_k of the kth resonant mode (typically only the fundamental mode is of interest in NMR detectors). The magnetic field is separated in the same way as the electric field:

$$\mathbf{B}(\mathbf{r},t) = \Re(i\mathbf{B}(\mathbf{r})e^{-\lambda t}) \tag{6.4}$$

Faraday's law can the be used to calculate the corresponding magnetic field distribution:

$$\mathbf{B}_k(\mathbf{r}) = \frac{1}{i\lambda_k}\nabla\times\mathbf{E}_k(\mathbf{r}) = \frac{\omega_k - i\delta_k}{\omega_k^2+\delta_k^2}\nabla\times\mathbf{E}_k(\mathbf{r}) \tag{6.5}$$

This definition ensures that the magnetic and electrical field distributions $\mathbf{E}_k$ and $\mathbf{B}_k$ can both be chosen to be real in the limit of a loss free system, while the true time-dependent electric and magnetic fields $\mathbf{E}(\mathbf{r},t)$ and $\mathbf{B}(\mathbf{r},t)$ are out of phase by $\pi/2$

The quality factor

$$Q_k = \frac{\omega_k}{2\delta_k} \tag{6.6}$$

represents the ratio of the stored to the dissipated energy per oscillation cycle. Therefore, the time-averaged loss power P_L can be computed from the maximum stored magnetic or electric energy and Q_k as

$$P_L = \frac{\omega_k}{Q_k} \int \frac{1}{2\mu} \mathbf{B}_k \cdot \mathbf{B}_k^{\dagger} d\mathbf{r} \tag{6.7}$$

By the correspondence principle, the sensitivity of a resonator tuned to the Larmor frequency is related to the normalised magnetic field

$$\tilde{\mathbf{B}}_k(\mathbf{r}) = \frac{\mathbf{B}_k(\mathbf{r})}{\sqrt{P_L}} \tag{6.8}$$

Transmission line resonators were simulated by finding numerical simulations to the eigenvalue Eq. 6.3. The geometry of the model is shown in figure 6.1. The conductor plates forming the resonator are represented by an impedance boundary condition, with the electric and magnetic fields excluded from the interior of the conductors.[141,150,151] This type of boundary condition constrains mutually perpendicular components of the magnetic and electric fields in the boundary to be proportional, with the ratio given by the surface impedance

$$Z_S \approx (1+i)\sqrt{\frac{\omega\mu}{2\sigma}} \tag{6.9}$$

where σ denotes the bulk conductivity. This eliminates the need to explicitly account for the exponential drop of the electric field within the skin depth, and greatly reduces the number of spatial elements needed for converged results. Due to the symmetry of the system, it is sufficient to explicitly represent only the quadrant $x \geq 0, y \geq 0$, corresponding to one lateral half of one conductor. The central plane (xz) between the conductor plates can be represented by a perfect electrical conductor (PEC) boundary condition, since the electric and magnetic fields are perpendicular and parallel to it by symmetry, respectively. For the middle plane through the conductors (yz), the inverse is true: the magnetic field is perpendicular to it, while the electric field is parallel. This

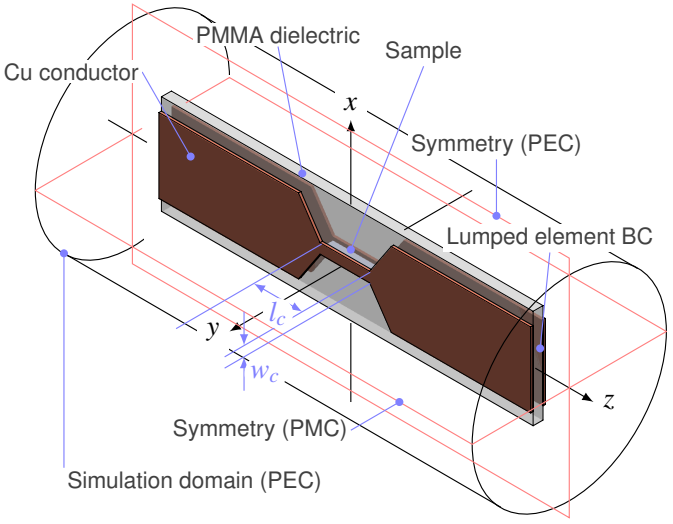

Figure 6.1: The model used to simulate the chosen geometry. One quarter of the model was defined explicitly and the remainder generated by symmetry using appropriate boundary conditions.

type of boundary condition is commonly referred to as a perfect magnetic conductor (PMC).

In practice, the resonator geometry is chosen to ensure an eigenfrequency close to, but somewhat above, the Larmor frequency. Fine-tuning is then achieved by adding small capacitances across the gaps in the copper in the top and bottom plates (Fig. 6.2). In the finite element simulations, these tuning capacitances were not explicitly modelled, but represented by lumped element boundary conditions at the end planes of the transmission line.

While a perfectly conservative resonator would be characterised by an imaginary eigenvalue λ_k and an infinite Q-factor, several sources of electromagnetic losses limit the attainable values of Q in practice. In the present model, we have taken into account the finite conductivity of the copper plates, the complex electric permittivity of the dielectric between the conductors, and the dissipation factor of the tuning capacitances. Table 6.1 lists the parameters that were used in the calculations.

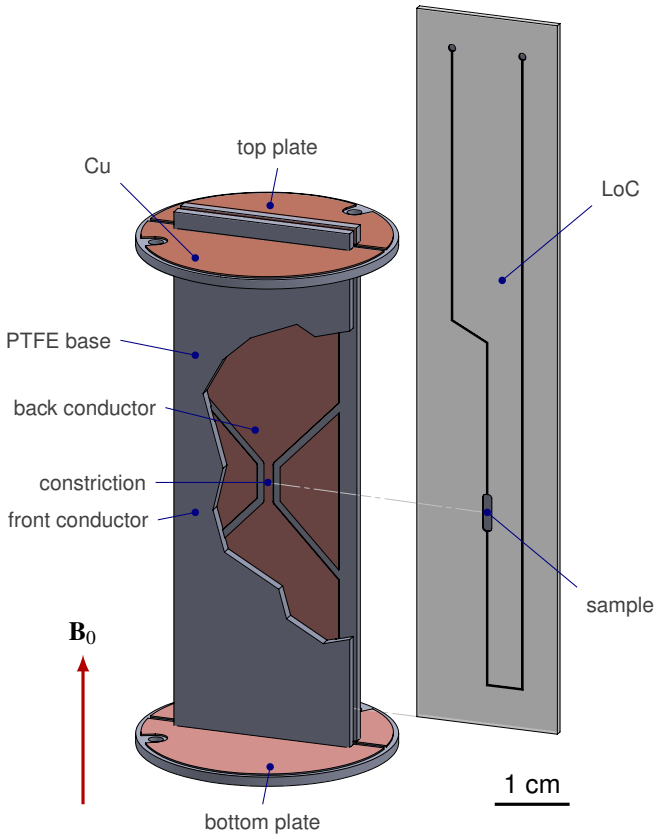

Figure 6.2: CAD drawing of the transmission line resonator with a corresponding microfluidic LoC device. A part of the front conductor plate has been removed to reveal the constriction at the location of the sample, and the LoC device has been displaced to the right for clarity.

6.2 Materials and Methods

Finite element simulations were carried out using COMSOL Multiphysics (COMSOL Inc, Cambridge, UK) using the radio frequency (RF) package. One quarter of the geometry of the double stripline was created and the rest generated by symmetry in order to minimise computing time. The geometry was represented using an unstructured tetrahedral mesh, with the distance between mesh vertices no more than a quarter of the width of the constricted section in the vicinity of the sample area. Materials of air, PMMA, and copper were assigned to the respective parts of the model in order to accurately simulate the relative permeability, permittivity, and electrical conductivity.

An impedance boundary condition is used at the conductor plates. The central plane between the conducting plates uses a perfect electrical conductor boundary condition, and the plane through the conductors a perfect magnetic boundary condition is used.

Lumped element boundary conditions are used to connect the ends of the plates to simulate the tuning capacitors. The electric wave equation is solved using an iterative eigenfrequency solver. This was then used to calculate self-resonance frequencies and quality factors.

6.3 Validation of the FEA model

The finite element model for planar transmission line resonators was validated by computing the resonance frequencies and quality factors for a range of different resonator geometries, and comparing them to experimental values obtained from prototypes built to nominal geometries from printed circuit board. Resonance frequencies and unloaded Q factors were obtained using a vector network analyser as described in the experimental section. Figure 6.3 shows the calculated normalised magnetic field $\tilde{\mathbf{B}}_x$ distributions at the centre planes of resonators with outside dimensions of 75 mm × 20 mm, and 1 mm separation. The constriction area is 20 mm^2 in all cases, but the aspect ratio of the constriction is varied from left to right, with the constriction lengths indicated in the figure. The magnetic field amplitude of the first eigenmode, normalised to 1 W of power dissipation, at the central plane between the resonator plates is shown in Figure 6.3. As can be seen clearly in the figure, the maximum magnetic field amplitude increases at first with the aspect ratio of the constriction, and reaches its highest value in the case of $l_c = 10$ mm. It should be noted that these computations simulated the free resonators, i.e. there were no capacitors at the ends. As a result, the frequency of the first eigenmode monotonously decreases with increasing aspect ratio, due to the increasing inductance of the structure. The simulated eigenfrequencies, compiled in the top panel of Figure 6.4 (open triangles), are in excellent agreement with the experimental results (filled triangles).

A second set of resonators were built, tested, and simulated. In this series, the aim was to use additional capacitors between the ends of the resonator conductors in order to keep the resonance frequency close to a target of 300 MHz. The necessary capacitor values were determined empirically. The same capacitance values were then represented in the finite element models as impedance boundary conditions at the end caps (Fig. 6.1). As shown in Figure 6.4 (open and filled circles), the agreement is reasonably good in all

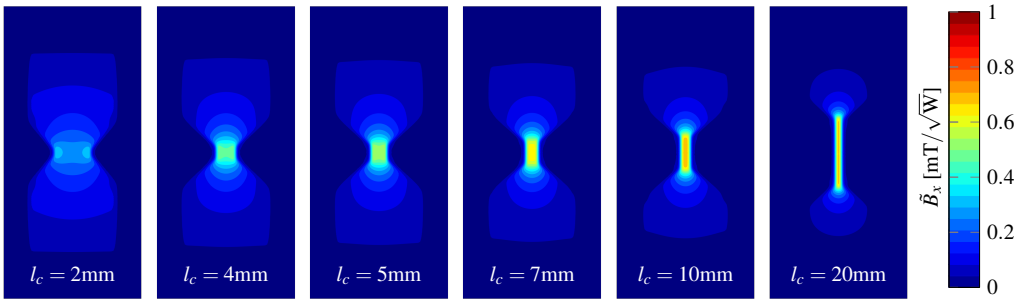

Figure 6.3: Field maps of the normalised magnetic field amplitude between resonator plates for resonators with varying constriction aspect ratio. Constriction areas is constant at 20 mm^2

cases, with the simulations systematically overestimating the resonance frequency by a small amount.

Computed and measured Q_0 factors for the tuned resonators are compared in the bottom panel of Figure 6.4. The simulations initially significantly overestimate Q_0 ($\otimes$). However, these computations assumed the end capacitors to be loss-free, and the only sources of dissipation were the finite conductivity of copper and the loss tangent of the dielectric. The predicted Q_0 values reach from 150 for a 20 mm $\times$ 1 mm ($l_c \times w_c$) constriction up to 310 in the case of 5 mm $\times$ 4 mm. This is not consistent with the measured values, which are constant at about 120 within the measurement accuracy (solid circles). However, the agreement is excellent if a complex boundary impedance $Z_{\text{end}} = (\tan\delta - i)/(\omega C_{\text{end}})$, including a realistic loss tangent $\tan\delta = 0.005$, is used to represent the end capacitors.

6.4 Optimisation

The FEA model was used to identify an optimal geometry of the resonator and the sample chamber. As is well known, the mass sensitivity of NMR detectors tends to improve as the detector volume is made smaller. Therefore, the sample volume was kept fixed at 2 μl. The thickness of the sample chamber, as well as the separation of the two resonator planes were also kept fixed due to fabrication limitations for the microfluidic chips, which were created from PMMA sheets of given thickness. This could be further optimised in the future. The free optimisation variables were therefore: the length of the sample chamber l_S, the length and width of the resonator constriction l_C and w_C, and the terminating capacitances at the end points C_{end}.

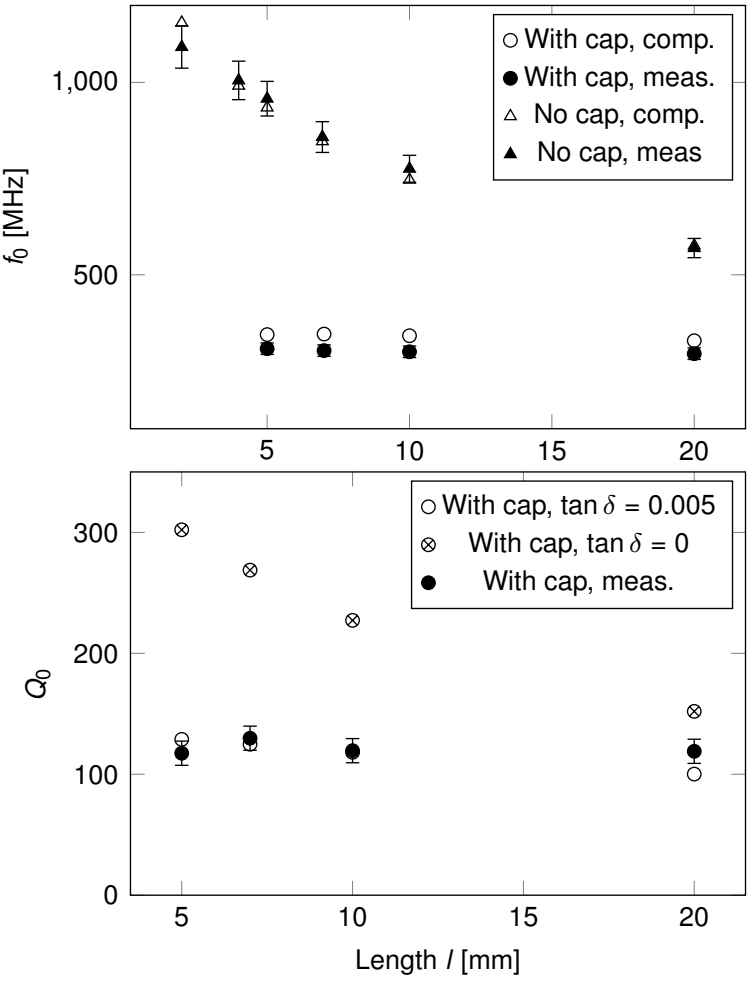

Figure 6.4: Validation of FEA model. Top: Predicted (open symbols) and experimental (filled symbols) resonance frequencies for open resonators (triangles) and for resonators tuned with end capacitors (circles). Bottom: predicted and measured resonator quality factors.

The optimisation objective was derived from the first and the second moment of the $\widetilde{\langle \mathbf{B}_x \rangle}$ distribution:

$$O_1 = \frac{\widetilde{\langle \mathbf{B}_x \rangle}}{mT/\sqrt{W}} \text{ and } O_2 = \sqrt{\frac{\langle B_x^2 \rangle}{\langle B_x \rangle^2} - 1} \tag{6.10}$$

where the angular brackets indicate averaging over the sample volume. The overall optimisation objective was a linear combination of O_1 and O_2

$$O = O_1 - \alpha O_2 \tag{6.11}$$

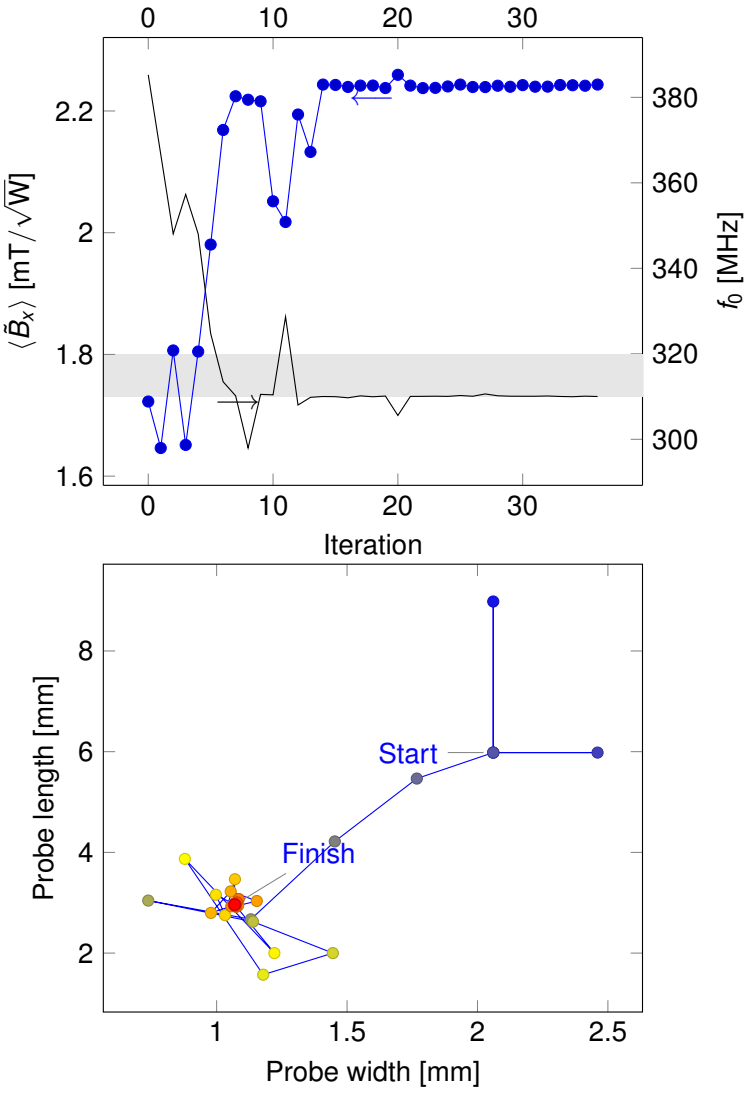

Figure 6.5: Top: convergence of the normalised average magnetic field $\langle \tilde{B}_x \rangle$ (blue dots). The resonance frequency (solid dark line) converges into the tolerance interval (grey band) within the first 10 iterations. Bottom: Optimisation trajectory of two out of the four optimisation variables.

where the weighting between efficiency (maximum $\widetilde{\langle \mathbf{B}_x \rangle}$) and homogeneity was controlled by the dimensionless parameter α. An α value of 0 indicates that the optimisation will target only the maximum efficiency, whereas a greater value of α will put more emphasis on the homogeneity. In addition to this objective, the optimisation was constrained to produce a resonance frequency between 310 and 320 MHz. A target slightly above the Larmor frequency of 300 MHz was chosen since it is easy in practice to correct the resonance frequency downward by adding a small parallel capacitance. By contrast, increasing the resonance frequency of a resonator is very difficult.

Table 6.1: Parameters to be optimised were the length (l_S) and width (w_S) of the sample chamber, the length (l_C) and width (w_C) of the constriction, and the end tuning capacitance (C_{end}). Note that the product $l_s w_s$ was constrained to 5 mm^2.

Parameter	*Unit*	*initial*	*optimised*	
			$\alpha = 0$	$\alpha = 10$
l_s	[mm]	3.66	3.66	4.64
$w_s = 5$ mm$^2/l_s$	[mm]	1.36	1.36	1.07
l_c	[mm]	6.00	2.97	5.20
w_c	[mm]	2.06	1.07	1.29
C_{end}	[pF]	35.00	57.40	52.98

The optimisation was carried out using the constrained optimisation by linear approximation (COBLYA) algorithm.[152] A typical optimisation trajectory is shown in Figure 6.5. As shown in the top panel, the average normalised magnetic field starts to rise after the first few iterations. At the same time, the optimisation adapts the end capacitance value (not shown in the figure) to adjust the resonance frequency within the target band (shown in grey). The normalised magnetic field then gradually increases, converging to a value of about 2.27 mT/$\sqrt{\text{W}}$ after 15 iterations. The trajectory of two out of the four optimisation variables is shown in the bottom panel of Figure 6.5. The initial geometry (marked as "Start") combines a 6 mm × 2 mm constriction with a 3.66 mm× 1.36 mm sample chamber (Table 6.1). As shown by the solid line in the top panel of Figure 6.5, this leads to too high a resonance frequency of more than 380 MHz. The optimisation algorithm then proceeds to decrease both the length and the width of the resonator, while leaving the sample chamber completely unchanged. The resonance frequency is quickly brought into the target band by a combination of the higher inductance caused by the smaller resonator, and an increase in the end capacitance. After about 15 iterations, the result is essentially converged.

Figure 6.6A shows a histogram of the RF magnetic field distribution over the sample volume resulting from the optimised structure. The optimisation has been run initially with $\alpha = 0$, thus optimising purely for efficiency. After convergence, α was set to 10, in order to obtain a balance between efficiency and homogeneity. As is obvious from Figure 6.6A, this leads to a lower average field amplitude, but a substantially narrower field distribution. From these histograms, proton nutation diagrams can easily be predicted. The results are shown in Figure 6.6B ($\alpha = 0$) and Figure 6.6C ($\alpha = 10$).

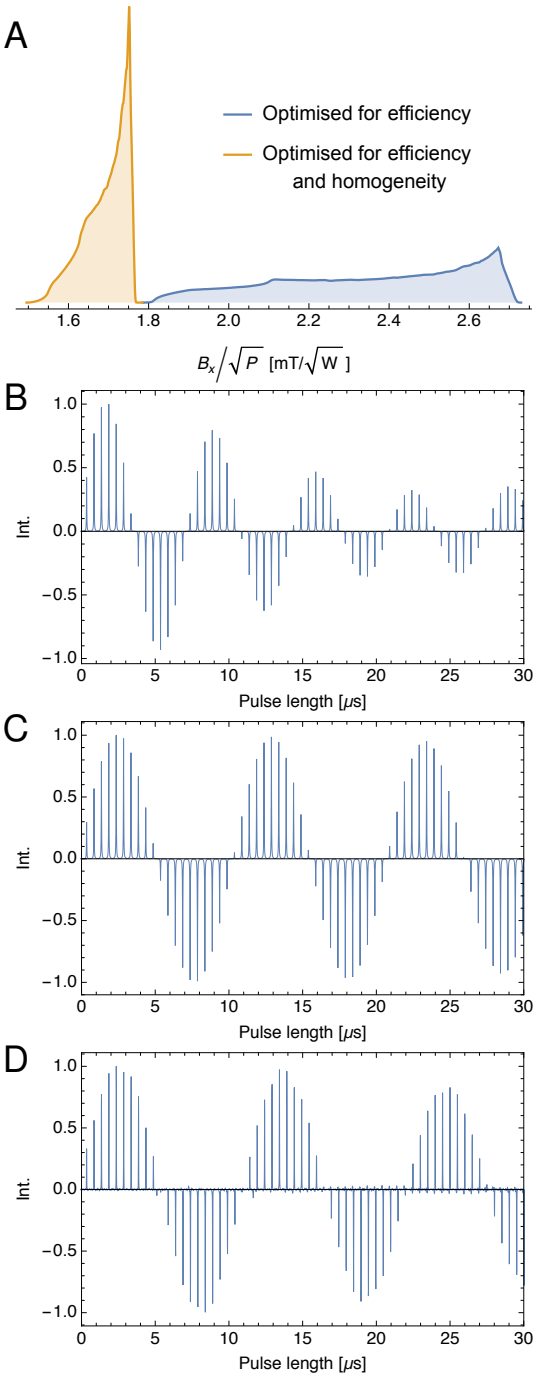

Figure 6.6: A: Histograms of normalised magnetic field amplitudes $\tilde{B}_x$ over the sample volume after optimisation with $\alpha = 0$ (efficiency, blue), and $\alpha = 10$ (efficiency and homogeneity, orange). B: computed nutation diagram from the histogram at $\alpha = 0$; C: computed nutation diagram at $\alpha = 10$; D: experimental nutation diagram from a resonator built to the geometry resulting from optimisation at $\alpha = 10$. (Results from this probe are described in Chapter 7)

These nutation diagrams have been computed assuming a power input of 6.9 W. In the case of $\alpha = 0$, the length of a 2π pulse is about 7 μs, compared to 10.5 μs for the resonator obtained with $\alpha = 10$. At the same time, the more homogeneous field distribution is reflected in a much slower decay of the nutation signal. The A_{810}/A_{90} ratio amounts to more than 95% in the case of $\alpha = 10$, where it is less than 50% for $\alpha = 0$.

6.5 Conclusion

A method of accurately simulating the magnetic field distribution of the double stripline geometry using finite element analysis has been developed. The FEA model provides a quantitative prediction of resonance frequencies and quality factors, taking into account resistive as well as dielectric losses. The absolute accuracy of these predictions is of the order of 5%. This information can be used to calculate the efficiency and homogeneity of the detector.

Using this method the detector design can be optimised to provide the maximum sensitivity whilst maintaining spectral resolution. The optimised design has sample dimensions of 4.64 $\times$ 1.07 $\times$ 1.50 mm and constriction dimensions of 5.20 $\times$ 1.29 mm. The geometry that has been optimised will need to be manufactured in order to prove that this optimisation has been successful. The results of this can be seen in Chapter 7.

This optimisation focussed on the length and width of the sample chamber, as well as the stripline constriction, and end capacitance. It is possible that the design could be further optimised by also taking into account the thickness of the sample chamber and the separation between the two conducting plates. These factors were not taken into account in our simulations because of manufacturing limitations.

Chapter 7

Optimised Stripline Design

Using the parameters calculated from the finite element simulations, an optimised stripline detector was manufactured. The stripline design was milled from copper laminated Teflon as this method is much faster for prototype generation than photolithography. The optimised design can be seen in Figure 7.1, featuring a 5.2 × 1.3 mm constriction. This design uses a microfluidic chip with a sample holder of dimensions 4.64 × 1.07 × 0.5 mm placed in the centre of the two conducting plates.

7.1 Materials and Methods

Nutation diagram was created using a sample of 150 mM sodium acetate (Sigma Aldrich) in H_2O with 10 mM 4,4-dimethyl-4-silapentane-1-sulfonic acid (DSS) (Sigma Aldrich) chemical shift reference. 60 single scan experiments were used each with 16k points.

1D experiments used a 9.5 W pulse for 3.2 μs duration for the 90° pulse. Sodium acetate spectrum was taken using the same sample as for the nutation experiment. 32 scans were used with a relaxation delay of 10 seconds. A water presaturation pulse of 3×10^{-5} W was applied for 3 seconds.

The growth medium spectrum uses a sample of Dulbecco Modified Eagle's Medium (DMEM) supplemented with 10% Fetal Bovine Serum (FBS) (Life Technologies, USA). The same mixture that is used to grow and maintain the MCF-7 cells in previous experiments. Spectrum is obtained using 256 scans with a 5 second delay.

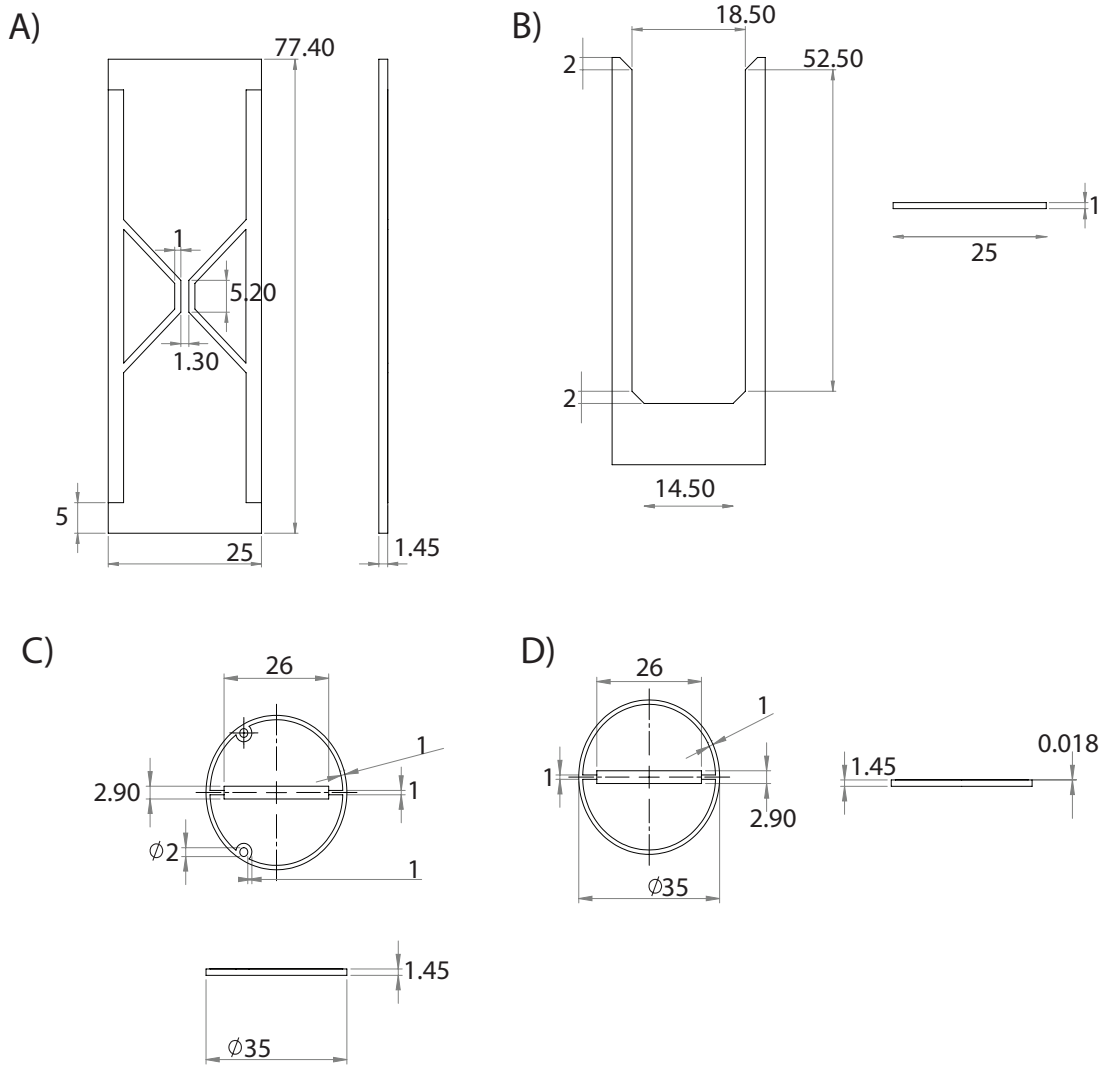

Figure 7.1: Technical drawings of the optimised detector design. A) Stripline conductor with constriction for sensitive detection. B) Chip holder, sandwiched between the two conducting plates to ensure sample is located in region of maximum sensitivity. C) Lower disk - used to connect the two conducting plates and for attachment to the probe base. D) Top disk - For connecting the two plates

7.2 Performance characterisation

As discussed in the Chapter 6, a resonator and corresponding microfluidic chip were built using the geometry optimised with $\alpha = 10$. The performance of this system was assessed using a solution of 150 mM sodium acetate in H_2O, with 10 mM DSS as a chemical shift reference. Figure 7.3 shows a representative spectrum obtained in this way. The acetate signal at 1.4 ppm was used for the experimental nutation spectrum shown in Figure 7.2B. Comparison with the corresponding simulated nutation diagram

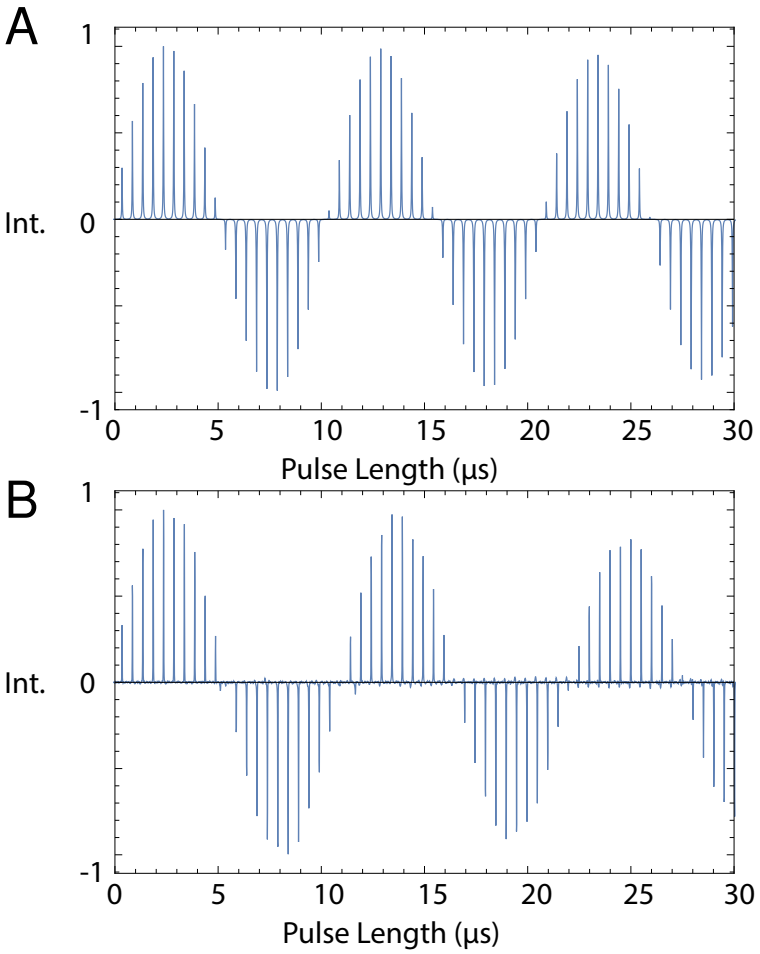

Figure 7.2: A: computed nutation diagram of optimised design; B: experimental nutation diagram from a resonator built to the geometry resulting from optimisation.

in Figure 7.2A shows that the two are in excellent agreement. It should be noted that there are no adjustable parameters in this comparison; the transmitter power in the in the experiment has been set to the same value (-10 dB on the Bruker AVANCE spectrometer, corresponding to 6.89 W) that was used in the simulations. The length of a 360° pulse at 11 μs (corresponding to a probe efficiency of 34.6 kHz/$\sqrt{W}$) is marginally longer in the experiment, but the difference is less than 0.5 μs. Also, the A_{810}/A_{90} ratio amounts to only 85%, compared to the simulated value of 95%. Both discrepancies are probably due to slight misalignment of the microfluidic chip and the probe assembly. Magnetic resonance images reveal that the centres of the probe and the sample chamber were misaligned sideways by 20 to 50 μm due to manufacturing tolerances.

The acetate spectrum shown in Figure 7.3 demonstrates the excellent B_0 homogeneity

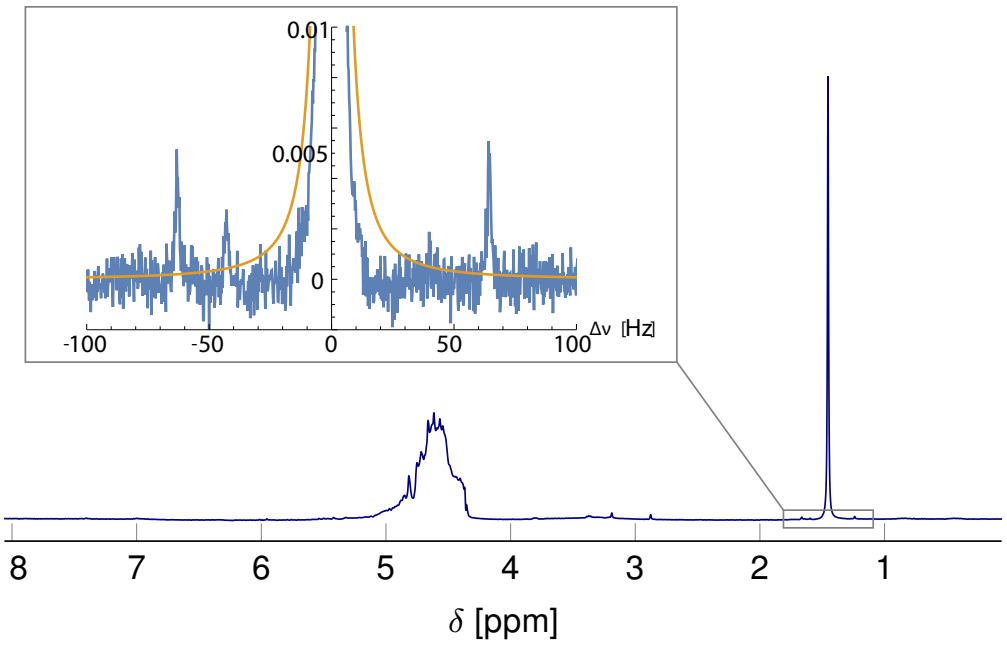

Figure 7.3: 1D NMR spectrum of 150 mM sodium acetate in H_2O, 32 scans with 90 Hz water presaturation. Expanded region shows the line width at the base of the peak and the ^{13}C satellites.

offered by the optimised probe/chip system. The width of the acetate peak is 1.73 Hz at half height, and 16.45 Hz and 29.0 Hz at 0.55% and 0.11% respectively. The inset in Figure 7.3 shows the details of the acetate peak base. The line shape is narrower than a Lorentzian peak with the same half width (orange solid line). A narrow peak base is particularly important for applications in metabolomics, where a large dynamic range is required to reliably quantify different metabolites with highly different concentrations. Figure 7.4 illustrates this with a spectrum obtained in 256 scans from 2 μl of a DMEM medium spectrum, a perfect echo sequence[143] was used to reduce signals from compounds with high molecular weight.

Both spectra exhibit a broad feature slightly downfield from the water resonance. This is most likely due to contributions to the signal from areas of the chip/probe system that are quite far away from the active site, e.g. the access channels and inlets into the microfluidic device. In these regions, the B_0 field is somewhat different in magnitude, leading to an apparent downfield shift of the water resonance. As a result, the CW presaturation is not effective in suppressing these signals. Closer investigation of the exact origin of these signals is currently underway, with the goal of finding a probe/chip design that will minimise them.

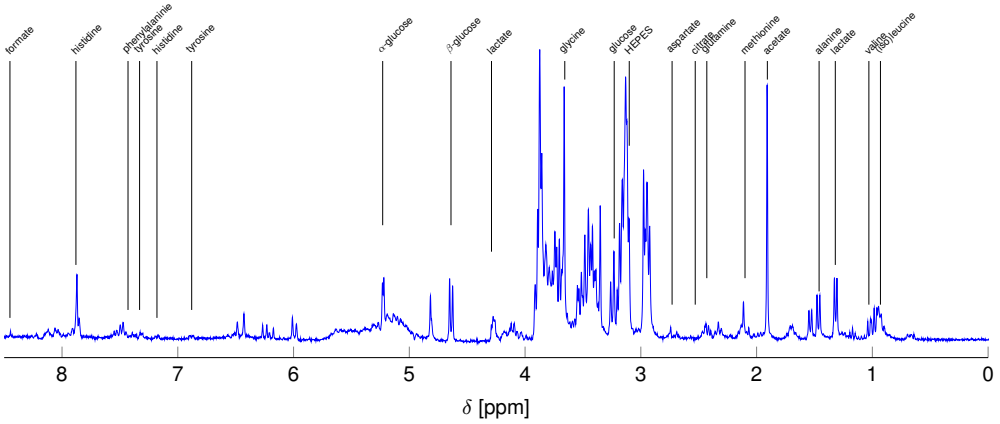

Figure 7.4: 1D NMR spectrum of DMEM cell growth medium solution supplemented with 10% fetal bovine serum, 256 scans with a total experiment time of 20 minutes.

The mass sensitivity of the optimised probe/chip system can be determined from the signal/noise ratio (SNR) of the acetate spectrum. The SNR of the acetate peak in the spectrum shown in Figure 7.3 is 4200:1 for 16 scans, corresponding to a value of 740 for a single scan. From the SNR, the limit of detection can be computed as[5]

$$\mathrm{nLOD}_\omega = \frac{3n\sqrt{\delta t}}{\mathrm{SNR}} \tag{7.1}$$

where n is the number of sample spins precessing in the chosen resonance, and δt is the total measurement time. Assuming a measurement time of 1.8 s per scan, which corresponds to the T_1 relaxation time of a typical metabolite such as glucose, and taking into account the number of protons that contribute to the acetate signal $n = 3 \cdot 150$ mM$\cdot$ 2 μl = 900 nmol, we obtain a limit of detection at 300 MHz of $\mathrm{nLOD}_\omega = 2.72$ nmol $\mathrm{s}^{1/2}$. It is common practice to report sensitivities of micro-NMR detectors at a standard field strength of 14.1 T (600 MHz) to facilitate comparison, using a scaling factor of $(\omega/\omega_0)^{\frac{7}{4}}$. The above limit of detection then amounts to $\mathrm{nLOD}_\omega^{600} = 1.57$ nmol $\mathrm{s}^{1/2}$.

Figure 7.5 again uses the plot comparing the mass sensitivities of a wide variety of different micro-NMR detectors that have been reported in the literature. Clearly, the optimised resonator compares favourably with other systems of similar size, and is on par with the most sensitive solenoid capillary detectors that have been reported. The optimised design is now also competitive in terms of mass sensitivity with a commercial

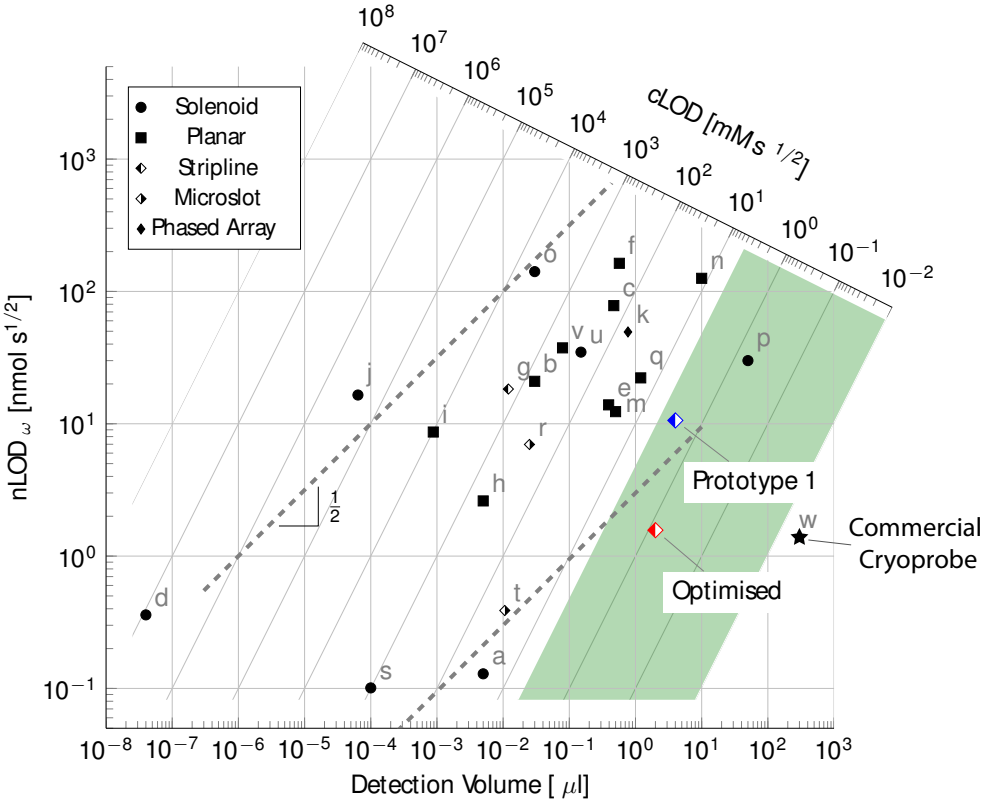

Figure 7.5: Plot comparing sensitivity of previously designed micro-NMR detectors. Letters a-t correspond to different authors as cited by Badilita *et al.*[5]. Data points u[6] and v[3] represent more recent work. Point *w*[7] refers to a commercial cryoprobe. The performance of the optimised probe presented here is shown in red, along with the earlier prototype that had not been numerically optimised (blue). (Adapted from Figure 5.8, individual references can be found in Table 2.1.)

cryoprobe.[7] Before optimisation, spectra with improved sensitivity could have been obtained by diluting the sample to 300 μl and testing in this cryoprobe. Now this method would yield spectra of similar sensitivity, and of course by not going through this process spectra can be obtained in-situ on a chip in a non-invase way.

Compared to the prototype stripline design, this optimised version shows improvement in both nLOD and cLOD. For practical metabolomics studies, the concentration limit of detection (cLOD) must be at least such that species present at 0.1 mM concentration can be quantified in about 20 min of measurement time. The detector presented here lies well inside this region, whereas many other micro-NMR detectors are not suitable for low-concentration studies, even though their mass sensitivity is superior. If scaled

to 600 MHz this detector should be able to detect 0.02 mM concentrations within a 2 μl sample (approximately 0.05 nmol) in 20 minutes.

The spectrum shown in Figure 7.4, obtained from a mixture of DMEM cell growth medium with 10% fetal bovine serum (FBS) demonstrates the feasibility of meaningful metabolomic studies using the optimised probe/chip system.

Chapter 8

Double Resonant Circuit Simulations

Having developed a detector that demonstrates sensitive in-situ detection of microfluidic devices, it was decided to investigate the possibility of tuning the probe to two frequencies. The aim was to adapt the detector circuit so that both ^{1}H and ^{13}C nuclei could be studied in a 7 T magnetic field. ^{13}C signals cover a 200 ppm range as opposed to around 10 ppm for ^{1}H and so are usually better resolved. However due to the low sensitivity of ^{13}C NMR (caused by a smaller gyromagnetic ratio and lower natural abundance) the main purpose of this double-tuning is to perform heteronuclear experiments rather than directly obtaining ^{13}C spectra. Heteronuclear 2D experiments allow more information to be found out about the molecules present and increase the range of applications including for structure determination of larger molecules. In the case of metabolomics, spectra can be very complicated and include peaks that overlap. By looking at the spectra in two dimensions the effective resolution of the spectrum is increased meaning that metabolites can be unambiguously identified.

There are several ways of tuning a probe circuit to multiple frequencies. These invariably involve the addition of extra components so will cause losses. The circuit used is optimised to be more efficient at the higher frequency which in our case is ^{1}H. This is so that 1D ^{1}H spectra can still be acquired with minimum loss in sensitivity. As well as this it is possible to detect other nuclei using the ^{1}H channel by using polarisation

transfer methods.[153] So as long as experiments are used that detect on the ^{1}H channel, sensitivity will be maximised.

8.1 Node Network Theory

The circuit used for multiple frequency tuning (Figure 8.1) is adapted from Mispelter et al.[8] It uses the original detector design (Z_{res}) with ^{1}H tuning (C_3) and matching (C_1) capacitors. In addition there are tuning (C_4) and matching (C_5) capacitors for the ^{13}C channel. It uses a high-frequency band stop (L_6 and C_6) and a low-frequency band pass (L_7 and C_7) to ensure that there is no power transferred between the two channels. To test how much loss is expected by adding the additional components and also to calculate expected values for the various capacitors/inductors required we need to simulate the circuit.

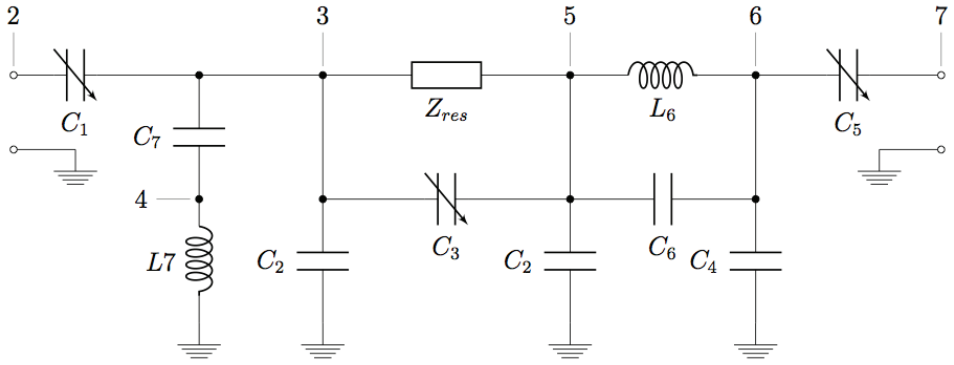

Figure 8.1: Double tuned probe circuit adapted from Mispelter et al.[8]

Values for the various circuit components can be calculated using network analysis.[154] In electronics, circuits are made up of a variety of interconnected components. Network analysis allows us to calculate the scattering parameters (or S-parameters) that describe the electrical behaviour of the network. Using this information we can find the resonant frequencies of the circuit when input values for the various capacitors and inductors are put in.

The network is described using the following definitions. A **component** is a device with two or more terminals through which current can flow. The circuit we are using is an RLC circuit, meaning that the components used consist of resistors (R), inductors (L),

and capacitors (C). A **node** (n) is the point where terminals of two components meet (represented by numbered black circles in Figure 8.1). Node 1 is ground by convention. A **branch** (b) is the component that joins two particular nodes. So in Figure 8.1, the branch $b_{2,3}$ would be the branch between nodes 2 and 3, represented by a variable capacitor C_1. A **port** (p) consists of two terminals where the current into one terminal is identical to the current out of the other one. In this case there are two ports, between nodes 1 and 2, and between nodes 1 and 7.

A series of matrices are created:

- **A** - Dimensions $(b \times n)$
  - This is known as the adjacency matrix, with values $A_{kl} = \pm 1$ if branch k connects to node l.
- $\mathbf{Y}^b$ - $(b \times 1)$ - List of branch admittances (Admittance is the inverse of impedance)
  - Admittance of the double stripline detector is taken from the finite element simulations (Chapter 6).
  - The admittance of the remaining branches can be calculated using the impedance equations for an RLC circuit.
  - $Y = \frac{1}{\omega L}$ for an inductor, $Y = \omega C$ for a capacitor
- $\mathbf{I}^b$ - $(b \times 1)$ - List of branch currents
- $\mathbf{V}^n$ - $(n \times 1)$ - Nodal voltages.
  - $V_1^n = 0$ by definition.
- $\mathbf{V}^p$ - $(p \times 1)$ - Port voltage differences
- $\mathbf{I}^p$ - $(p \times 1)$ - Port currents
- **P** - $(n \times p)$ - Port definitions

8.1.1 Calculation of the S-matrix

Ohm's law states that current passing through a conductor is directly proportional to the voltage ($V = IR$). Using Ohm's law, by substituting resistance for admittance, the branch current can be calculated as follows:

$$I_k^b = Y_k^b \sum_l A_{kl} V_l^n \tag{8.1}$$

However the individual branch currents ($\mathbf{I}^b$) and nodal voltages ($\mathbf{V}^n$) are currently unknown. Kirchoff's current law states that the sum of currents into any node m must vanish. (The sum of the currents flowing into the node is equal to the sum of the currents flowing out of the node.) Therefore the sum of the internal currents plus the sum of the port currents must equal zero:

$$\sum_k I_k^b A_{km} + \sum_q I_q^p P_{mq} = 0 \forall m \tag{8.2}$$

Combining Equations 8.1 and 8.2 gives

$$\sum_{k,l} Y_k^b A_{kl} V_l^n A_{km} + \sum_q I_q^p P_{mq} = 0 \tag{8.3}$$

This can be simplified by contructing the internal admittance matrix from the branch admittances and adjacency matrices:

$$Y_{lm}^n = \sum_k Y_k^b A_{kl} A_{km} \tag{8.4}$$

We can then rewrite Eq. 8.3 as Eq. 8.5 relating the port current to the nodal voltages:

$$\mathbf{Y}^n \cdot \mathbf{V}^n + \mathbf{P}\ \mathbf{I}^p = 0 \tag{8.5}$$

An admittance matrix that relates port voltages and currents would allow computation of the S matrix directly.

Since we know that $V_1^n = 0$ (ground by definition), we can remove one equation from the system. This yields the reduced admittance matrix $\mathbf{Y}^{nr}$, and the reduced port definition matrix $\mathbf{P}^r$

- $\mathbf{Y}^{nr}$ - Dimensions $(n-1 \times n-1)$

- $\mathbf{P}^r$ - $(n-1 \times p)$

The voltage vector is now $\mathbf{V}^{nr} = [V_2\ V_3\ V_4\ ...\ V_n]^T$ (V_1 removed). With this reduction $\mathbf{Y}^{nr}$ should have full rank (all voltage differences are well defined).

(From a rearranged version of Equation 8.5) The voltages are:

$$\mathbf{V}^{nr} = -(\mathbf{Y}^{nr})^{-1}\mathbf{P}^r\ \mathbf{I}^p \tag{8.6}$$

The port voltages can be calculated from the nodal voltages by using the port definition matrix $\mathbf{P}^r$:

$$\mathbf{V}^p = \mathbf{P}^{rT}\mathbf{V}^{nr} \tag{8.7}$$

$$\mathbf{V}^p = -\mathbf{P}^{rT}(\mathbf{Y}^{nr})^{-1}\mathbf{P}^r\ \mathbf{I}^p \tag{8.8}$$

Therefore the port impedance matrix, by dividing by the current is:

$$\mathbf{Z}^p = -\mathbf{P}^{rT}(\mathbf{Y}^{nr})^{-1}\mathbf{P}^r \tag{8.9}$$

From the port impedance matrix, the frequency dependant S matrix is computed:

$$\mathbf{S} = (\mathbf{Z}^p - Z_0\mathbf{1})(\mathbf{Z}^p Z_0\mathbf{1})^{-1} \tag{8.10}$$

Z_0 is the reference impedance, which in this case is set to 50 Ω.

8.1.2 Calculation of Branch Voltages

Voltage differences can be obtained with the branch adjacency matrix

$$\mathbf{V}^b = \mathbf{A}^r\mathbf{V}^{nr} \tag{8.11}$$

These can be calculated by combining with Equation 8.6:

$$\mathbf{V}^b = -\mathbf{A}^r(\mathbf{Y}^{nr})^{-1}\mathbf{P}\mathbf{I}^p \tag{8.12}$$

This can then be used to calculate the power dissipation in the different branches.

8.2 Double Resonant Circuit Simulation

The double tuned probe circuit was simulated using a node network calculation. The numbered points in Fig. 8.1 represent the nodes used in the calculation.

Calculation of the frequency dependent S matrix is made using realistic values for the various capacitors and inductors. The S parameters are then plotted in relation to the frequency (Figure 8.2). At resonance the S_{11} and S_{22} plots (Figure 8.2A and B) show a minimum where power is no longer reflected back to the input channel. The tuning and matching capacitors in the circuit were adjusted until the ^{1}H and ^{13}C resonances were at approximately the desired frequency (300 and 75 MHz respectively). Normally a reflection in these plots would aim to have a minimum at around -30 dB, corresponding to 0.1% power reflected. These peaks do not reach those levels, indicating that the circuit isn't perfectly matched, but they were just used to find starting values for the capacitors and inductors in the actual circuit. There is likely to be some variation in the exact values required so this was deemed good enough as a starting point.

Usually at the resonance frequency the S_{12} plot would show a peak where power is transmitted across the channels. To prevent this cross-talk from happening a band stop is used for the ^{1}H frequency and a band pass to ground used for the ^{13}C frequency. Each of these filters is comprised of a capacitor and an inductor. The values of the inductors and capacitors used is adjusted until a peak is no longer seen in the S_{12} plot (Figure 8.2C and D). In fact the amount of power transferred across the two channels is less than -40 dB (0.01%).

Figure 8.3 shows the power dissipation from the different components in the probe circuit, as calculated in section 8.1.2. Figure 8.3A shows that this set-up is an efficient method for detecting on the ^{1}H channel, with 53% of all power dissipated through the

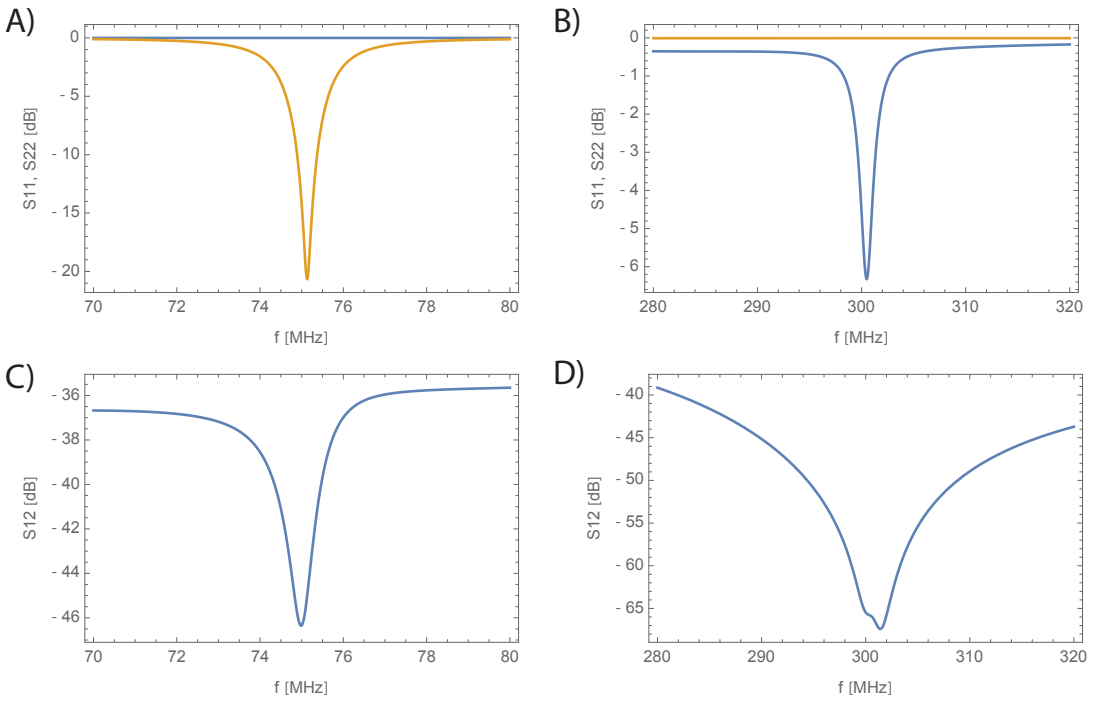

Figure 8.2: Simulation of the S-parameters (S_{11}, S_{12}, and S_{22}) calculated by nodal network analysis. A) Reflected power in the ^{1}H (blue, S_{11}) and ^{13}C (yellow, S_{22}) channels in the 75 MHz range. B) Reflected power in the ^{1}H (blue, S_{11}) and ^{13}C (yellow, S_{22}) channels in the 300 MHz range. C) Cross-talk between the two channels in the 75 MHz range (S_{22}). D) Cross-talk between the two channels in the 300 MHz range (S_{22}).

resonator. Conversely, Fig. 8.3B shows that at the ^{13}C frequency only 11% of power is dissipated in the resonator and the remaining power is lost through other components in the circuit, notably the two additional inductors. This means that direct detection of ^{13}C is not going to be as efficient. This is made use of by always detecting signals on the ^{1}H channel in order to achieve the maximum sensitivity.

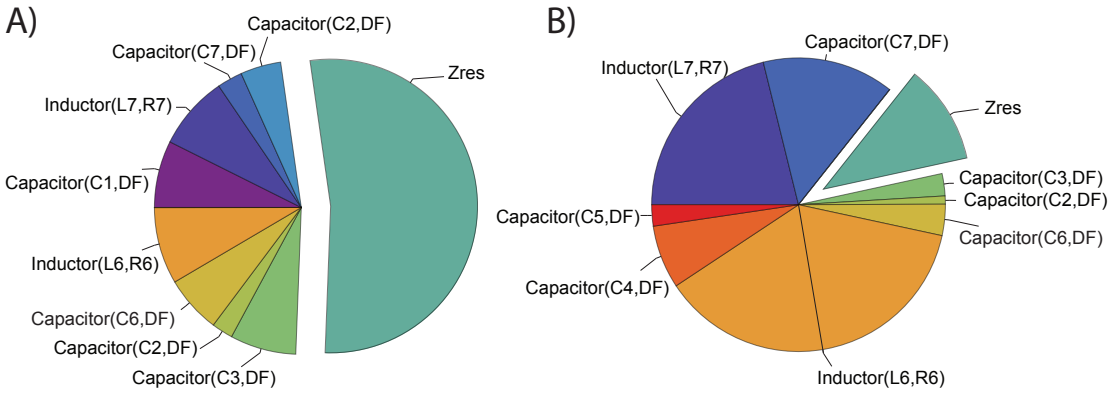

Figure 8.3: Pie chart showing power dissipation through the circuit, with dissipation through the resonator in the pulled out slice A) After a pulse at the 300 MHz. B) After a 75 MHz pulse

Chapter 9

Two Channel Probe

9.1 Heteronuclear NMR

Significant effort has been made to develop NMR detection systems that integrate with microfluidic systems.[155,61,63] Most of these efforts have focussed on metabolomic characterisation of biological systems, based on highly resolved one dimensional 1H spectra.

By contrast, multi-dimensional heteronuclear NMR methods, which are widely used in conventional formats for the study of the structure, dynamics, and interactions of biomacromolecules, have only rarely been integrated with microfluidic systems. Doing so would enable important applications, such as in-situ protein binding studies requiring only very small amounts of sample, integration of protein expression with structural and dynamic analysis by NMR on a chip, and others. For metabolomic applications, heteronuclear multidimensional methods offer significant advantages in spectral resolution over one dimensional spectroscopy. This is because spectral peaks are spread out over two dimensions, so peaks that were previously overlapping may now be more easily observed.

Heteronuclear two dimensional NMR using microcoils has previously been established using fixed capillary sample holders with solenoid coils. Realistic concentrations of proteins have been studied using such systems.[156] Solenoidal coils however are not compatible with microfluidic systems and the increased functionality that they offer. Two dimensional NMR on a chip using a non-resonant microcoil has been performed and has the advantage of being able to perform experiments on a variety of nuclei without

need for tuning and matching.[157] Microfluidic heteronuclear two dimensional NMR has also been demonstrated recently by Spengler et al.[158] with an elegant combination of micro-fabricated Helmholtz-coil detector and a microfluidic sample holder. However, the concentration limit of detection for these systems was relatively high, requiring several hours of acquisition for a heteronuclear single-quantum correlation (HSQC) spectrum of a sample at a concentration of 1 M. By contrast, biologically relevant samples, either metabolic mixtures or purified solutions of proteins, are of the order of 1 mM. Practical implementations of microfluidic heteronuclear correlation spectroscopy that operate at this level of concentrations have not yet been demonstrated.

We present a microfluidic detector and chip platform that is capable of producing high quality $^{1}H/^{13}C$ HSQC and HMQC spectra of 2 μl samples at concentrations as low as 1 mM. The system builds on the optimised transmission line detector geometry[10] for ^{1}H NMR spectroscopy at a field of 7 T (300 MHz ^{1}H Larmor frequency). Based on detailed finite element modelling of the complex resonator impedance as a function of frequency, we have designed a tuning/matching circuit that allows simultaneous operation at 7 T at both the ^{1}H and the ^{13}C resonance frequencies. The tuning/matching circuit has been optimised for efficiency at the ^{1}H frequency, which is similar to that of the original, singly tuned system. By contrast, the efficiency at the ^{13}C frequency is considerably poorer. This enables proton-detected techniques such as HSQC and HMQC, which are among the most sensitive heteronuclear techniques known today and which form the backbone of structural and dynamic studies of biomacromolecules.

The results demonstrate that it is possible to obtain useable HMQC and HSQC 2D spectra from ^{13}C-isotope labelled compounds, including proteins, at low mM concentrations. Even more complex pulse sequences, such as HMQC-TOCSY, are readily implemented on the system. As a proof of principle, we show that the binding of a peptide to calmodulin can be observed on the chip by following shifts in the HSQC signals of the methyl groups in universally ^{13}C labelled calmodulin at 3 mM concentration.

9.2 Materials and Methods

Nutation experiments performed using a 1 M solution of glycine-^{13}C-^{15}N (Cambridge Isotope Laboratories) in H_2O. The ^{1}H nutation diagram was made using 300 experiments

with pulse lengths ranging from 0 to 60 μs. Experiments used a single scan and had a 5 second relaxation delay. The ^{1}H 90° pulse for the following experiments is 3.6 μs for 10 W. The ^{13}C nutation diagram was made using 250 experiments ranging from 0 to 325 μs. Experiments each had 16 scans and used a 20 second relaxation delay. The ^{13}C 90° pulse for the following experiments is 22 μs

Glucose experiments were performed using a samples of 2 M glucose-1-^{13}C (Cambridge Isotope Laboratories, Inc., USA) or 200 mM D-Glucose (Sigma Aldrich) in D_2O with DSS (Sigma Aldrich) added as a chemical shift reference. HMQC experiments use a standard HMQC pulse sequence with GARP decoupling.[159] A 72 μs pulse is used at 16 dB attenuation for the decoupling pulse. The HMQC experiment was recorded with a spectral width of 12 ppm in the ^{1}H dimension and 180 ppm in the ^{13}C dimension, 512 data points and 512 increments with a relaxation delay of 5 s between scans.

The HMQC-TOCSY experiment uses a standard HMQC pulse sequence with a mixing period of 150 ms at the end. The spectra were recorded using a spectral width of 12 ppm in the ^{1}H dimension and 180 ppm in the ^{13}C dimension, 512 data points and 512 increments with a 3 s delay between scans. The ^{13}C TOCSY spectrum was created using covariance processing of the corresponding HMQC spectrum.[160]

Amino acid mixtures are made up of 1 mM glycine-2-^{13}C-^{15}N, alanine-2-^{13}C, methionine-(methyl-^{13}C), and proline-$^{13}C_5$-^{15}N (all Cambridge Isotope Laboratories, Inc.)in D_2O with 4,4-dimethyl-4-silapentane-1-sulfonic acid (Sigma Aldrich) added as a chemical shift reference. The HSQC experiment was recorded with a spectral width of 12 ppm in the ^{1}H dimension and 180 ppm in the ^{13}C dimension, 512 data points and 512 increments with a relaxation delay of 3 s between scans.

Ubiquitin sample was prepared using 3 mM ubiquitin in D2O with HEPES buffer. The HSQC experiment was recorded with a spectral width of 12 ppm in the ^{1}H dimension and 150 ppm in the ^{13}C dimension, 1600 data points and 400 increments with 16 scans per increment and a relaxation delay of 2 s between scans.

Calmodulin samples were of 2 mM in D_2O with 25 mM Bis-Tris, 150 mM KCl, 10 mM CaCl2, pH 6.8. One sample was supplemented with eEF2K82-100 peptide to 2 mM (1:1 ratio), and the pH adjusted to 6.8. The HSQC experiments were recorded with a spectral width of 12 ppm in the ^{1}H dimension and 150 ppm in the ^{13}C dimension, 1600

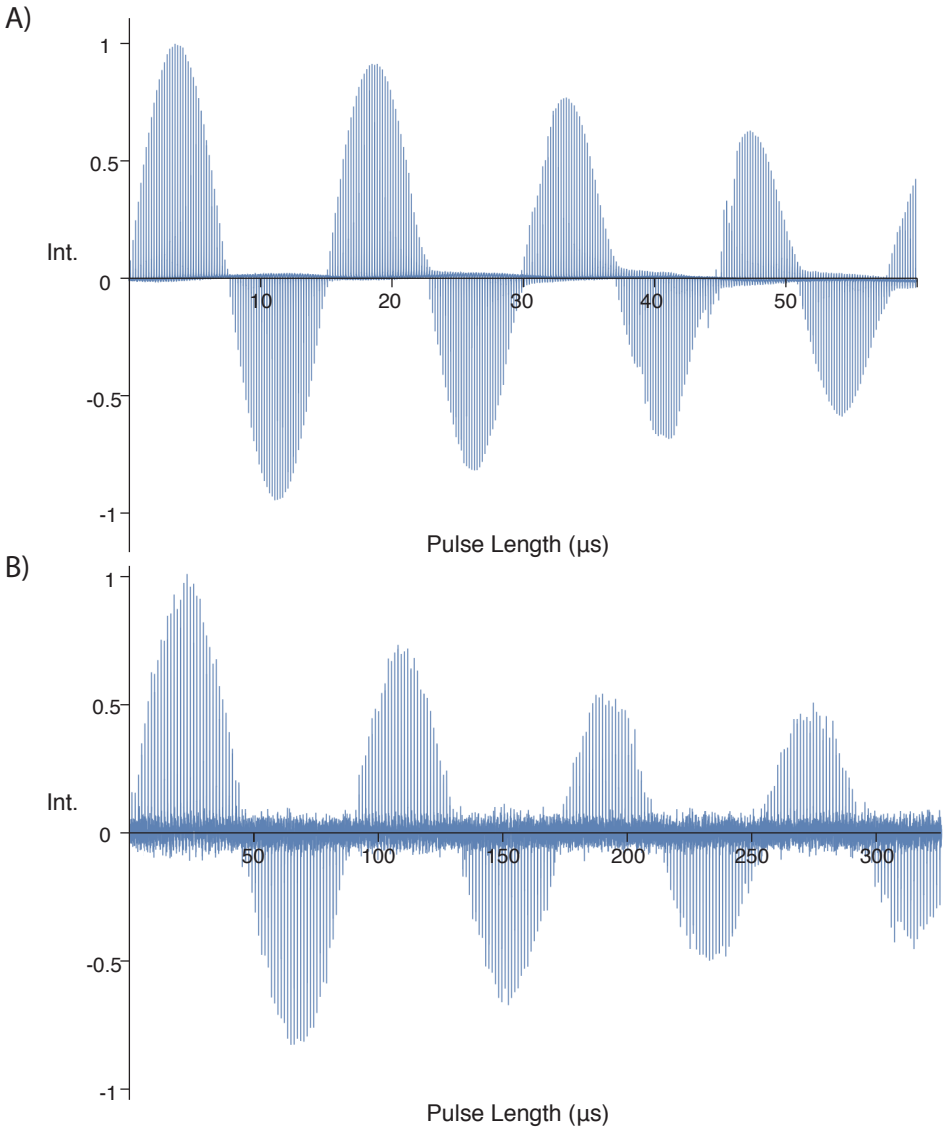

Figure 9.1: Experimental nutation diagrams. A) ^{1}H nutation diagram B) ^{13}C nutation diagram

data points and 200 increments with 32 scans per increment and a relaxation delay of 1 s between scans.

9.3 Double resonance probe characterisation

The probe circuit (Figure 8.1) was assembled based on the previous simulations. With the values for inductors/capacitors used as a starting point.

Performance of the probe was assessed using a 1 M solution of glycine-^{13}C-^{15}N in H_2O. The glycine signal at 3.54 ppm was used for the nutation diagram shown in Fig. 9.1A with a transmitter power of 10 W. The length of a 2π pulse is 15.2 μs corresponding to a probe efficiency of 20.8 kHz/$\sqrt{\text{W}}$. This corresponds to 87% of the efficiency of the single channel probe.

The A_{810}/A_{90} ratio is 77.2% which is sufficient to perform complex pulse sequences beyond the conventional pulse-acquire scheme (Figure 9.2 onwards).

Figure 9.1 shows the nutation digram of the ^{13}C glycine signal 175.1 ppm in a 2 M solution of glycine-^{13}C-^{15}N in H_2O. A higher concentration of glycine was used for this experiment to allow direct detection of the ^{13}C in a reasonable experiment time. The length of a 2π pulse at 10 W is 144 μs, with an A_{810}/A_{90} ratio of 53%. It would be expected that the ^{13}C pulse length would be at least 4 times longer than the ^{1}H pulse length due to the smaller gyromagnetic ratio. In this case the ^{13}C pulse length is around 10 times the ^{1}H pulse, due to the circuit being optimised for the higher frequency nucleus. This indicates that direct ^{13}C detection within a reasonable experiment time is not a feasible technique for this probe, but by using polarisation transfer techniques to detect on the ^{1}H nucleus.

9.4 2D Experiments

Tuning the probe to two frequencies leaves the efficiency of the proton channel at 20.8 KHz/$\sqrt{\text{W}}$, corresponding to 87% of the efficiency of the singly tuned probe. To compensate for the relative insensitivity of the lower frequency nucleus, polarisation transfer techniques such as HSQC are used which can increase ^{13}C sensitivity by a factor of 32.[27]

Initial testing of the multiply tuned probe was performed on a sample of 2 M glucose-1-^{13}C. Figure 9.2 shows the HMQC spectrum of this sample with the anomeric peaks of the α and β forms of glucopyranose found when glucose is in solution.[161] The signal to noise ratio (SNR) of the spectrum of this 1 hour 46 minute experiment is approximately 40,000. This sensitivity allows the peaks for the natural abundance ^{13}C found in the rest of the glucose molecule to be observed, as can be seen in the expanded region of Figure 9.2 when the receiver gain of the spectrum is increased. The natural abundance ^{13}C is present in concentrations of approximately 10 mM for each isomer.

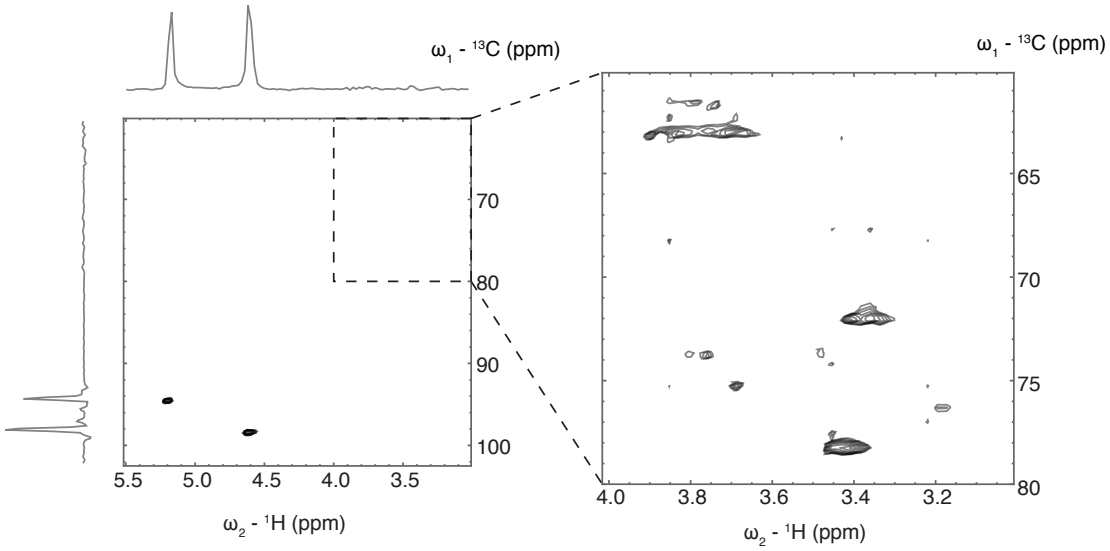

Figure 9.2: HMQC spectrum of 2 M glucose-1-^{13}C in D_2O

More complex variants of the HMQC experiment are also possible, such as the HMQC-TOCSY, which provides additional connectivity information.[160] Using covariance processing a ^{13}C-^{13}C TOCSY spectrum can be taken showing connectivity of ^{13}C atoms within a molecule.[160] Figure 9.3B shows the separation of the α and β form of glucopyranose in a solution of 200 mM unlabelled glucose in D_2O. In this sample ^{13}C is present in concentrations of approximately 1 mM for each isomer, indicating that the probe can perform heteronuclear experiments at the low concentrations present in biological samples. This also demonstrates the capability of the probe to perform more complex pulse sequences.

By using isotopically labelled samples, spectra from samples of biologically relevant concentrations can be obtained. Fig. 9.4 shows the HSQC spectrum of a mixture of amino acids in solution at 1 mM concentration. In this spectrum, methionine and glycine peaks are separated from proline peaks which would have been overlapping in the 1D ^{1}H spectrum. This also demonstrates the sensitivity of the detector, with approximately 200 ng of each amino acid present in the sample.

The HSQC spectrum of a 3 mM solution of ^{13}C-labelled ubiquitin using the micro-detector at 7 T (Figure 9.5B) is comparable to that of a 600 μl sample in a state-of-the-art cryoprobe at 14 T (Figure 9.5A). While the stripline spectrum is less resolved, it was obtained from approximately 50 μg (6 nmol) of protein. The unexpected line is caused by the solvent and could be removed using a solvent supression method. Scaling

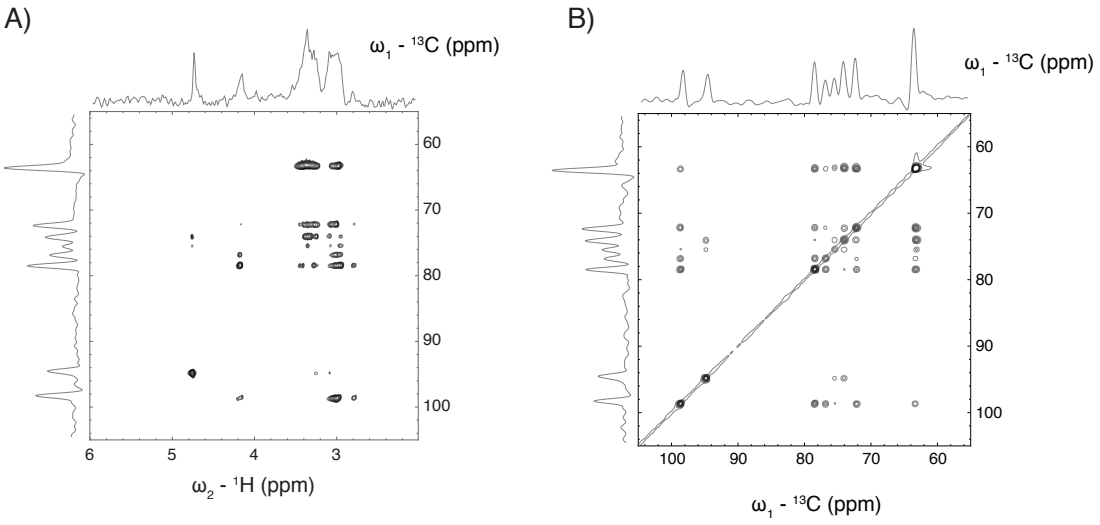

Figure 9.3: A) HMQC-TOCSY spectrum of 200 mM unlabelled glucose in D_2O. B) ^{13}C TOCSY of 200 mM unlabelled glucose in D_2O.

the detector design to also function at 600 MHz should cause an improvement in both resolution and sensitivity. This result demonstrates the feasibility of high-quality protein NMR spectroscopy in a microfluidic system. A commercial MicroCryoProbe is able to obtain a spectrum from approximately 35 nmol of protein (VpR247) in 35 μl in 2 hours of experiment time[162] so the detector demonstrated in this work really is competitive with commercially available probes.

The ability to perform protein NMR spectroscopy on a microfluidic system open a range of experimental applications, such as protein binding studies. Frequently this is performed by taking a sample of pure protein, a sample of completely bound protein and swapping aliquots of these samples to produce an array of different concentrations. These are studied by NMR spectroscopy and useful information such as the binding constant can be calculated. By performing this experiment on a microfluidic chip, the amount of expensive, labelled sample can be reduced.

In this case the sample chamber of the chip was filled by syringe pumps containing the appropriate quantities of calmodulin (CaM) protein and corresponding substrate eukaryotic elongation factor-2 kinase (pep2) to study the changes in the HSQC spectrum with different concentrations of pep2.

Figure 9.6 shows the methyl group region of the CaM HSQC spectrum. The resolution in this experiment is not sufficient to quantify the rate of binding, however clear differences

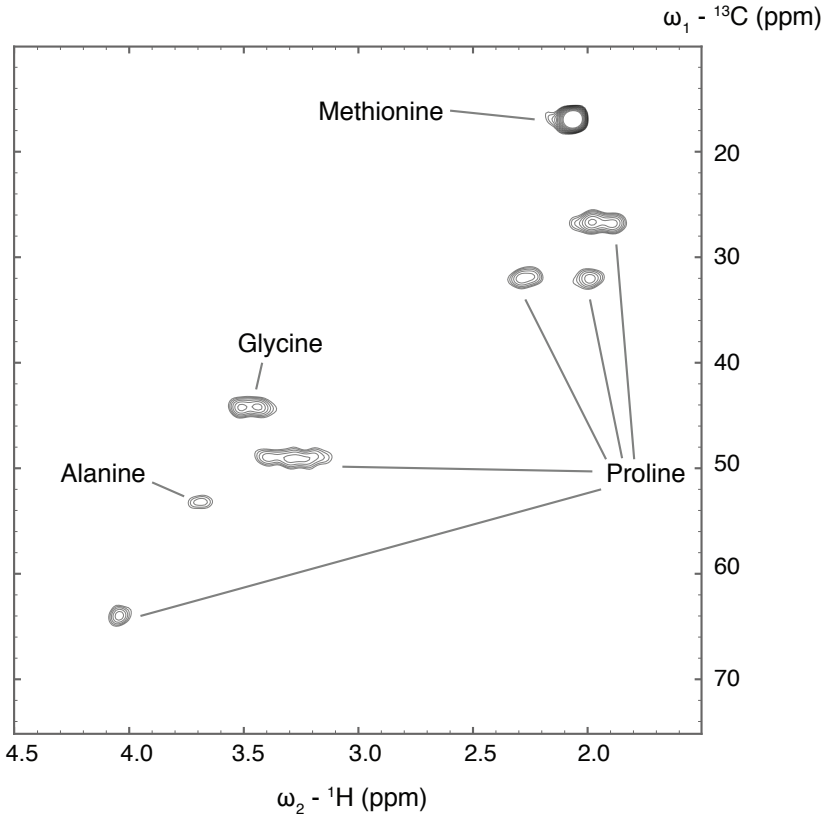

Figure 9.4: HSQC of 1 mM solution of glycine-2-^{13}C-^{15}N, alanine-2-^{13}C, methionine-(methyl-^{13}C), and proline-$^{13}C_5$-^{15}N in D_2O.

can be observed between the two pure CaM and the CaM:pep2 complex particularly in the isoleucine sites that are labelled. By taking this experiment to a higher field, such as 14 T, both resolution and sensitivity would be improved making these experiments more informative.

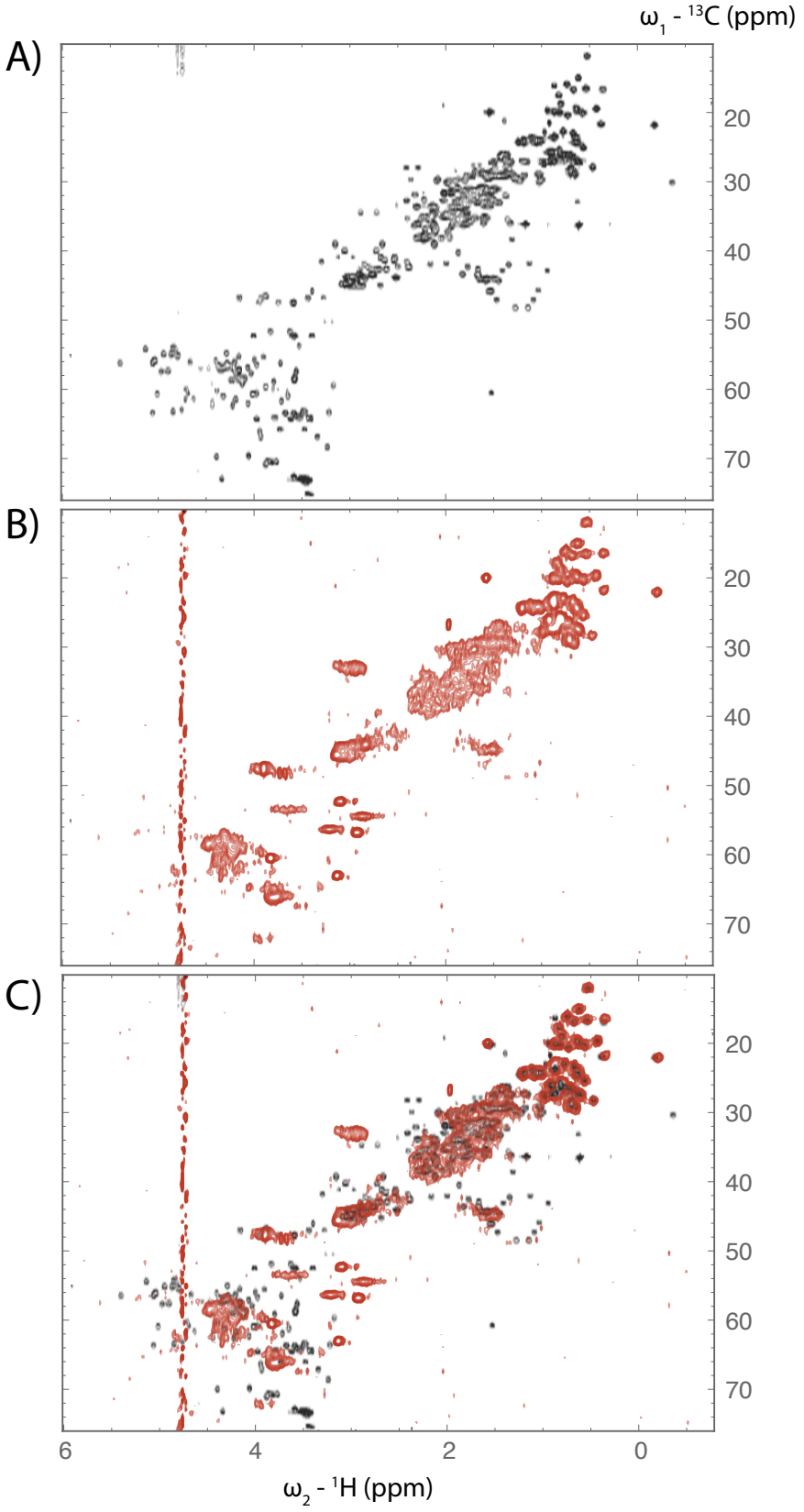

Figure 9.5: Comparison of stripline HSQC spectrum with spectrum taken using a state-of-the-art cryoprbe. A) ^{1}H-^{13}C-HSQC spectrum of a ubiquitin standard sample obtained at 600 MHz with cryoprobe. B) ^{1}H-^{13}C-HSQC spectrum using the double stripline detector of 3 mM ubiquitin in D_2O measured at 300 MHz. C) Overlay of cryoprobe spectrum (black) and stripline spectrum (red).

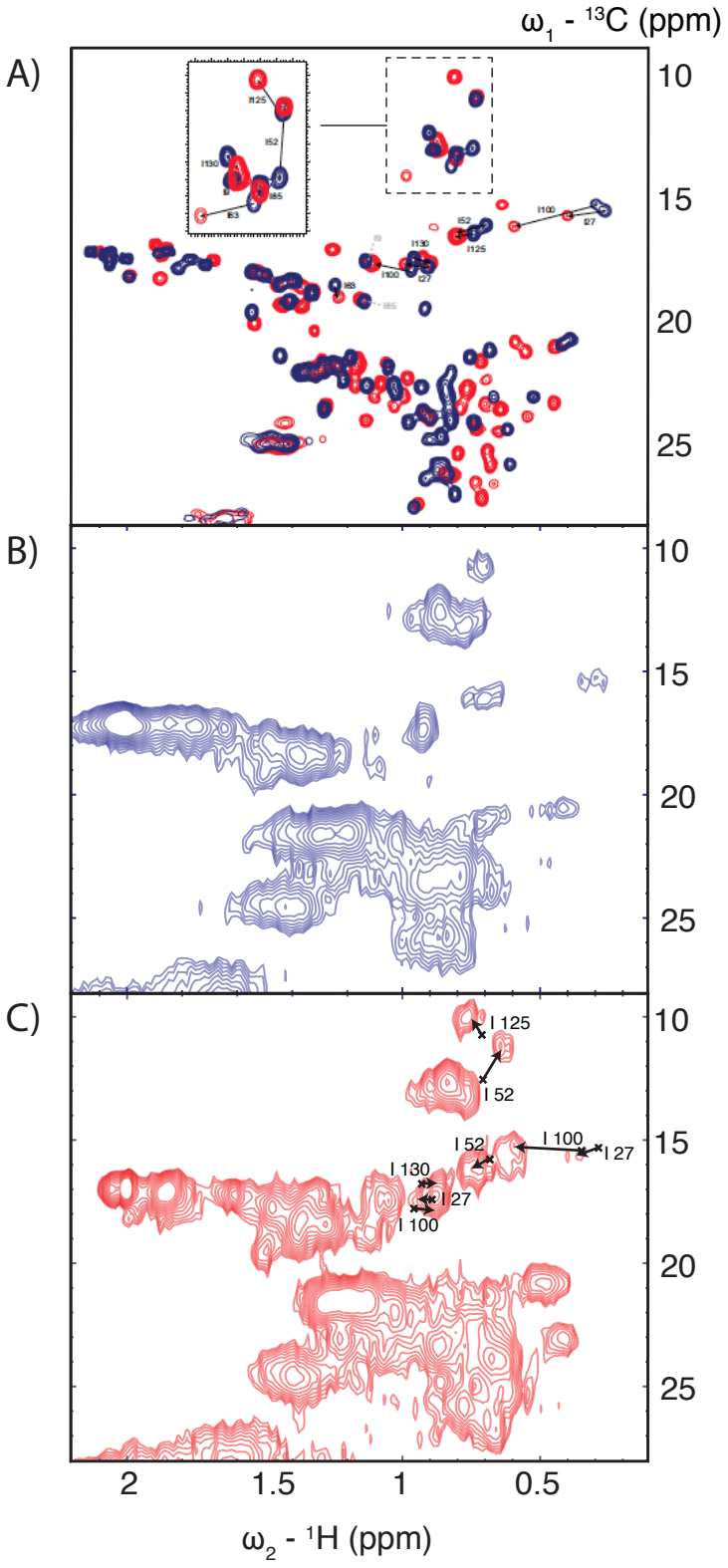

Figure 9.6: Comparison of ^{1}H-^{13}C spectra in a commercial cryoprobe and using the stripline probe A) HSQC spectra taken from Hooper.[9] Obtained at 700 MHz using a cryoprobe of 400 μl of 0.1 mM CaM (blue)and CaM:pep2 complex (red) Changes in isoleucine methyl group resonances are indicated. B) HSQC spectrum obtained at 300 MHz using the stripline detector of 2 μl of 2 mM CaM. C) HSQC spectrum obtained at 300 MHz using the stripline detector of 2 μl of 2 mM CaM:pep2 complex, with the expected changes in isoleucine methyl group peaks indicated.

Chapter 10

Conclusions

We have optimised and demonstrated a new design of double micro-stripline detector that is compatible with functional microfluidic LoC devices, allowing non-invasive, sensitive observation of a 2 μl sample of sub-mM concentration. Its performance compares favourably with micro-NMR systems described by other authors. The optimisation has taken into account both the shape of the sample chamber and the RF resonator. Details of the geometry can make a big difference to the sensitivity of the probe. Different performance criteria, such as sensitivity and RF homogeneity, compete with each other, and a compromise must be chosen that fits the intended applications. While the present work has proved the principle of non-invasive NMR detection inside LoC devices with high sensitivity and resolution, the chip we have used is still rather primitive, and does not yet implement any active fluidic components such as continuous flow perfusion. Extensions of the current design are being developed in our group to allow active perfusion, controlled gas exchange and growth of cell populations on chip. Also, the probe will be fitted with an active temperature control system, in order to ensure optimum growth conditions during NMR measurements.

A method of simulating both planar microcoils and a double micro-stripline detector has been demonstrated using finite element analysis. This allows accurate predictions of the resonance frequency, and associated B_1 field to be generated within just a few minutes of computational time. Planar microcoils can provide very good sensitivity, but the B_1 resolution is limited by the geometry. The fact that inductively coupled coil frequency is largely dependent on the geometry of the coil and is difficult to tune to

the desired frequency is a major drawback. Difficulties in production by lithographic methods due to the small feature size mean that accurate manufacture of these coils to the specification required is challenging. For these reasons this design was not pursued.

It is possible that the geometry of the double stripline design could be further optimised. Our optimisation took into account the length and width of the sample chamber, the length and width of the constriction in the striplines, and the end capacitance. Optimisation of the sample chamber thickness, as well as the gap between the two conducting plates may yield a small improvement in sensitivity. These factors were not taken into account in this work due to manufacturing limitations.

The double micro-stripline detector demonstrated is capable of studying biologically relevant concentrations of sample within a 2 μl volume. Previously developed NMR micro-detectors have demonstrated enhanced limits of detection by going to extremely small volumes. However the concentrations of sample required in these small volumes is much greater. For example an extremely sensitive solenoid detector has been shown to have a nLOD of 0.1 nmol $s^{1/2}$ within a 100 pl volume. The cLOD for this detector is therefore 1000 mM $s^{1/2}$. Many metabolites are present in concentrations of less than 1 mM and it important to be able to detect these concentrations within a relatively short period of time as this is a dynamic system. The optimised double micro-stripline detector from this work has an nLOD of 1.57 nmol $s^{1/2}$ in a 2 μl sample, corresponding to a cLOD of 0.8 mM $s^{1/2}$. It is predicted that if this detector was used at a frequency of 600 MHz that less than 0.1 nmol of sample could be detected in less than 20 minutes experiment time. This mass sensitivity is comparable with that of a commercial cryoprobe.[7]

As well as the high-sensitivity demonstrated in this work, the B_0 homogeneity from using this design allows NMR spectra of complicated mixtures to be practical. Linewidths of less than 2 Hz are usually obtained after shimming meaning that the peaks in metabolomic spectra are distinguishable. By adapting the probe to work at higher frequencies it is expected that resolution can be improved still further.

The sensitivity obtained in this work puts the prospects of micro-NMR spectroscopy for metabolomics in perspective. It has been argued that single-cell metabolomics would provide a substantial gain in insight, since it would allow to elucidate the metabolic *heterogeneity* of a cell population.[163,111] The volume of a typical MCF-7 cell is of the order of 50 pl, or 5×10^{-5} μl. Detecting concentrations of 0.1 mM in approximately 10 minutes

experimental time in such a small volume would require a nLOD of 1.25×10^{-4} nmol $s^{1/2}$. Given the favourable scaling of mass sensitivity with detector volume, one might hope that an optimised design might offer such a high sensitivity. However, from Figure 7.5, it is clear that even with the scaling taken into account, this would represent an improvement of four orders of magnitude over the best existing detectors, which is unlikely to be possible. It should be noted, however, that hyperpolarisation techniques potentially offer a factor of 10^4 improvement in sensitivity,[164] and could therefore bring NMR metabolomic observation of single cells within reach. However, hyperpolarisation schemes tend to be molecule-specific, and would be unlikely to apply across a wide range of different metabolic species.

While the present work has proved the principle of NMR metabolomics in LoC devices, the chip we have used is still rather primitive, and does not yet implement any active fluidic components such as continuous flow perfusion, time-modulated injection of drugs, etc. Extensions of the current design are being developed in our group to allow active perfusion, controlled gas exchange, and controlled exposure of the cell population of xenobiotic drugs. Also, the probe will be fitted with an active temperature control system, in order to ensure optimum growth conditions during NMR measurements.

Additional information can be gained using a two-channel probe. Using a circuit that is optimised for the higher frequency mode sensitivity of the probe is maintained, whilst allowing heteronuclear experiments to be performed. This allows complex spectra from mixtures of a large molecules to be interpreted. This means that more information can be gathered from spectra that would have a number of overlapping peaks in a simple 1D experiment such as those found in metabolomics. The principle of studying protein structure changes using small quantities of expensive isotopically-labelled sample is demonstrated. While the present work has shown the feasibility of examining such samples on a chip, extending this principle to a probe operating at a higher field would offer further improvements in both sensitivity and resolution. Although there are some improvements that can be made to the design, the probe is competitive with commercially available MicroCryoProbes. These can obtain high quality 2D spectra from approximately 35 nmol of protein in 2 hours experiment time. Although the spectra shown here aren't currently as highly resolved, they are taken using smaller samples of protein (for example 4 nmol calmodulin). This could potentially be very useful in reducing the amount of isotopically labelled protein that is required for structural or binding studies.

References

[1] J. A. Rogers, R. J. Jackman, G. M. Whitesides, D. L. Olson, and J. V. Sweedler, "Using microcontact printing to fabricate microcoils on capillaries for high resolution proton nuclear magnetic resonance on nanoliter volumes," *Appl. Phys. Lett.*, vol. 70, no. 18, p. 2464, 1997.

[2] H. Ryan, S.-H. Song, A. Zaß, J. Korvink, and M. Utz, "Contactless NMR spectroscopy on a chip.," *Anal. Chem.*, vol. 84, no. 8, pp. 3696–702, 2012.

[3] N. Spengler, A. Moazenzadeh, R. C. Meier, V. Badilita, J. G. Korvink, and U. Wallrabe, "Micro-fabricated Helmholtz coil featuring disposable microfluidic sample inserts for applications in nuclear magnetic resonance," *J. Micromechanics Microengineering*, vol. 24, no. 3, p. 034004, 2014.

[4] A. P. M. Kentgens, J. Bart, P. J. M. van Bentum, A. Brinkmann, E. R. H. van Eck, J. G. E. Gardeniers, J. W. G. Janssen, P. Knijn, S. Vasa, and M. H. W. Verkuijlen, "High-resolution liquid- and solid-state nuclear magnetic resonance of nanoliter sample volumes using microcoil detectors," *J. Chem. Phys.*, vol. 128, no. 5, p. 052202, 2008.

[5] V. Badilita, R. C. Meier, N. Spengler, U. Wallrabe, M. Utz, and J. G. Korvink, "Microscale nuclear magnetic resonance: a tool for soft matter research," *Soft Matter*, vol. 8, no. 41, p. 10583, 2012.

[6] R. C. Meier, J. Höfflin, V. Badilita, U. Wallrabe, and J. G. Korvink, "Microfluidic integration of wirebonded microcoils for on-chip applications in nuclear magnetic resonance," *J. Micromechanics Microengineering*, vol. 24, no. 4, p. 045021, 2014.

[7] T. W.-M. Fan and A. N. Lane, "Applications of NMR spectroscopy to systems biochemistry," *Prog. Nucl. Magn. Reson. Spectrosc.*, vol. 92, pp. 18–53, 2016.

[8] J. Mispelter, M. Lupu, and A. Briguet, *NMR Probeheads for Biophysical and Biomedical Experiments*. Imperial College Press, first edit ed., 2006.

[9] K. Hooper, *Structural studies on the interaction between eukaryotic elongation factor 2 kinase (eEF2K) and calmodulin (CaM)*. PhD thesis, University of Southampton, 2015.

[10] G. Finch, A. Yilmaz, and M. Utz, "An optimised detector for in-situ high-resolution NMR in microfluidic devices.," *J. Magn. Reson.*, vol. 262, pp. 73–80, 2016.

[11] K. W. Jordan, J. Nordenstam, G. Y. Lauwers, D. A. Rothenberger, K. Alavi, M. Garwood, and L. L. Cheng, "Metabolomic characterization of human rectal adenocarcinoma with intact tissue magnetic resonance spectroscopy.," *Dis. Colon Rectum*, vol. 52, no. 3, pp. 520–5, 2009.

[12] J. M. Perkel, "Life Science Technologies: MicrofluidicsBringing New Things to Life Science," *Science (80-.).*, vol. 322, no. 5903, 2007.

[13] C. Rivet, H. Lee, A. Hirsch, S. Hamilton, and H. Lu, "Microfluidics for medical diagnostics and biosensors," *Chem. Eng. Sci.*, vol. 66, no. 7, pp. 1490–1507, 2011.

[14] K. M. Horsman, J. M. Bienvenue, K. R. Blasier, and J. P. Landers, "Forensic DNA Analysis on Microfluidic Devices: A Review," *J. Forensic Sci.*, vol. 52, no. 4, pp. 784–799, 2007.

[15] C. D. Chin, V. Linder, and S. K. Sia, "Commercialization of microfluidic point-of-care diagnostic devices," *Lab Chip*, vol. 12, no. 12, p. 2118, 2012.

[16] J. El-Ali, P. K. Sorger, and K. F. Jensen, "Cells on chips.," *Nature*, vol. 442, no. 7101, pp. 403–11, 2006.

[17] H. Andersson and A. van den Berg, "Microfluidic devices for cellomics: a review," *Sensors Actuators B Chem.*, vol. 92, no. 3, pp. 315–325, 2003.

[18] H. Kimura, T. Yamamoto, H. Sakai, Y. Sakai, and T. Fujii, "An integrated microfluidic system for long-term perfusion culture and on-line monitoring of intestinal tissue models.," *Lab Chip*, vol. 8, no. 5, pp. 741–6, 2008.

[19] J. Clausell-Tormos, D. Lieber, J.-C. Baret, A. El-Harrak, O. J. Miller, L. Frenz, J. Blouwolff, K. J. Humphry, S. Köster, H. Duan, C. Holtze, D. A. Weitz, A. D. Griffiths, and C. A. Merten, "Droplet-based microfluidic platforms for the encapsulation and screening of Mammalian cells and multicellular organisms.," *Chem. Biol.*, vol. 15, no. 5, pp. 427–37, 2008.

[20] T. Takebe, K. Sekine, M. Enomura, H. Koike, M. Kimura, T. Ogaeri, R.-R. Zhang, Y. Ueno, Y.-W. Zheng, N. Koike, S. Aoyama, Y. Adachi, and H. Taniguchi, "Vascularized and functional human liver from an iPSC-derived organ bud transplant," *Nature*, vol. 499, no. 7459, pp. 481–484, 2013.

[21] D. Rugar, R. Budakian, H. J. Mamin, and B. W. Chui, "Single spin detection by magnetic resonance force microscopy," *Nature*, vol. 430, no. 6997, pp. 329–332, 2004.

[22] F. Bloch, "Nuclear Induction," *Phys. Rev.*, vol. 70, no. 7-8, pp. 460–474, 1946.

[23] E. M. Purcell, H. C. Torrey, and R. V. Pound, "Resonance Absorption by Nuclear Magnetic Moments in a Solid," *Phys. Rev.*, vol. 69, no. 1-2, pp. 37–38, 1946.

[24] G. Bodenhausen and D. J. Ruben, "Natural abundance nitrogen-15 NMR by enhanced heteronuclear spectroscopy," *Chem. Phys. Lett.*, vol. 69, no. 1, pp. 185–189, 1980.

[25] G. A. Morris and R. Freeman, "Enhancement of nuclear magnetic resonance signals by polarization transfer," *J. Am. Chem. Soc.*, vol. 101, no. 3, pp. 760–762, 1979.

[26] D. Hoult and R. Richards, "The signal-to-noise ratio of the nuclear magnetic resonance experiment," *J. Magn. Reson.*, vol. 24, no. 1, pp. 71–85, 1976.

[27] M. H. Levitt, *Spin dynamics : basics of nuclear magnetic resonance*. Chichester, England: Wiley, 2nd ed., 2008.

[28] X.-H. Zhu, H. Merkle, J.-H. Kwag, K. Ugurbil, and W. Chen, "17O relaxation time and NMR sensitivity of cerebral water and their field dependence," *Magn. Reson. Med.*, vol. 45, no. 4, pp. 543–549, 2001.

[29] H. Wen, A. S. Chesnick, and R. S. Balaban, "The design and test of a new volume coil for high field imaging.," *Magn. Reson. Med.*, vol. 32, no. 4, pp. 492–8, 1994.

[30] A. Webb, "Increasing the Sensitivity of Magnetic Resonance Spectroscopy and Imaging," *Anal. Chem.*, vol. 84, no. 1, pp. 9–16, 2012.

[31] K. Golman, O. Axelsson, H. Jóhannesson, S. Månsson, C. Olofsson, and J. Petersson, "Parahydrogen-induced polarization in imaging: Subsecond 13 C angiography," *Magn. Reson. Med.*, vol. 46, no. 1, pp. 1–5, 2001.

[32] M. Haake, J. Natterer, and J. Bargon, "Efficient NMR Pulse Sequences to Transfer the Parahydrogen-Induced Polarization to Hetero Nuclei," *J. Am. Chem. Soc.*, vol. 118, no. 36, pp. 8688–8691, 1996.

[33] J. Brossel and A. Kastler, "La Detection De La Resonance Magnetique Des Niveaux Excites-Leffect De Depolarisation Des Radiations De Resonance Optique Et De Fluorescence," *Comptes Rendus Hebd. Des Seances L Acad. Des Sci.*, vol. 229, no. 23, pp. 1213–1215, 1949.

[34] A. Abragam and M. Goldman, "Principles of dynamic nuclear polarisation," *Reports Prog. Phys.*, vol. 41, no. 3, pp. 395–467, 1978.

[35] M. Goldman, *Spin temperature and nuclear magnetic resonance in solids*. Clarendon Press Oxford, 1970.

[36] V.-V. Telkki, V. V. Zhivonitko, S. Ahola, K. V. Kovtunov, J. Jokisaari, and I. V. Koptyug, "Microfluidic Gas-Flow Imaging Utilizing Parahydrogen-Induced Polarization and Remote-Detection NMR," *Angew. Chemie Int. Ed.*, vol. 49, no. 45, pp. 8363–8366, 2010.

[37] P. Styles, N. Soffe, C. Scott, D. Crag, F. Row, D. White, and P. White, "A high-resolution NMR probe in which the coil and preamplifier are cooled with liquid helium," *J. Magn. Reson.*, vol. 60, no. 3, pp. 397–404, 1984.

[38] C. Koo, R. Godley, M. McDougall, S. Wright, and A. Han, "A Microfluidically Cryo-cooled Spiral Microcoil with Inductive Coupling for MR Microscopy.," *IEEE Trans. Biomed. Eng.*, vol. 61, no. 1, pp. 76–84, 2013.

[39] J. Stocker, T. Peck, A. Webb, M. Feng, and R. Magin, "Nanoliter volume, high-resolution NMR microspectroscopy using a 60-μm planar microcoil," *IEEE Trans. Biomed. Eng.*, vol. 44, no. 11, pp. 1122–1127, 1997.

[40] T. Peck, R. Magin, and P. Lauterbur, "Design and Analysis of Microcoils for NMR Microscopy," *J. Magn. Reson. Ser. B*, vol. 108, no. 2, pp. 114–124, 1995.

[41] D. L. Olson, T. L. Peck, A. G. Webb, R. L. Magin, and J. V. Sweedler, "High-Resolution Microcoil 1H-NMR for Mass-Limited, Nanoliter-Volume Samples," *Science (80-.).*, vol. 270, no. 5244, pp. 1967–1970, 1995.

[42] E. Harel, C. Hilty, K. Koen, E. E. McDonnell, and A. Pines, "Time-of-Flight Flow Imaging of Two-Component Flow inside a Microfluidic Chip," *Phys. Rev. Lett.*, vol. 98, no. 1, p. 017601, 2007.

[43] V. Malba, R. Maxwell, L. B. Evans, A. F. Bernhardt, M. Cosman, and K. Yan, "Laser-Lathe Lithography - a Novel Method for Manufacturing Nuclear Magnetic resonance Microcoils," *Biomed. Microdevices*, vol. 5, no. 1, pp. 21–27, 2003.

[44] R. W. Wiseman, T. S. Moerland, and M. J. Kushmerick, "Biological applications for small solenoids: NMR spectroscopy of microliter volumes at high fields," *NMR Biomed.*, vol. 6, no. 2, pp. 153–156, 1993.

[45] Y. Li, A. M. Wolters, P. V. Malawey, J. V. Sweedler, and A. G. Webb, "Multiple solenoidal microcoil probes for high-sensitivity, high-throughput nuclear magnetic resonance spectroscopy," *Anal. Chem.*, vol. 71, no. 21, pp. 4815–4820, 1999.

[46] L. O. Sillerud, A. F. McDowell, N. L. Adolphi, R. E. Serda, D. P. Adams, M. J. Vasile, and T. M. Alam, "1H NMR Detection of superparamagnetic nanoparticles at 1T using a microcoil and novel tuning circuit.," *J. Magn. Reson.*, vol. 181, no. 2, pp. 181–90, 2006.

[47] V. Badilita, K. Kratt, N. Baxan, M. Mohmmadzadeh, T. Burger, H. Weber, D. V. Elverfeldt, J. Hennig, J. G. Korvink, and U. Wallrabe, "On-chip three dimensional microcoils for MRI at the microscale.," *Lab Chip*, vol. 10, no. 11, pp. 1387–90, 2010.

[48] J. Spadea and S. Wright, "Optimization of printed coil arrays for microscopic imaging and spectroscopy," in *Proc. 19th Annu. Int. Conf. IEEE Eng. Med. Biol. Soc. 'Magnificent Milestones Emerg. Oppor. Med. Eng. (Cat. No.97CH36136)*, vol. 1, pp. 464–466, IEEE, 1997.

[49] S. Eroglu, G. Friedman, and R. Magin, "Estimate of losses and signal-to-noise ratio in planar inductive micro-coil detectors used for NMR," *IEEE Trans. Magn.*, vol. 37, no. 4, pp. 2787–2789, 2001.

[50] D. Issadore, C. Min, M. Liong, J. Chung, R. Weissleder, and H. Lee, "Miniature magnetic resonance system for point-of-care diagnostics," *Lab Chip*, vol. 11, no. 13, pp. 2282–2287, 2011.

[51] K. Ehrmann, K. Pataky, M. Stettler, F. M. Wurm, J. Brugger, P.-A. Besse, and R. Popovic, "NMR spectroscopy and perfusion of mammalian cells using surface microprobes.," *Lab Chip*, vol. 7, no. 3, pp. 381–3, 2007.

[52] Y. Maguire, I. L. Chuang, S. Zhang, and N. Gershenfeld, "Ultra-small-sample molecular structure detection using microslot waveguide nuclear spin resonance.," *Proc. Natl. Acad. Sci. U. S. A.*, vol. 104, no. 22, pp. 9198–203, 2007.

[53] P. J. M. van Bentum, J. W. G. Janssen, A. P. M. Kentgens, J. Bart, and J. G. E. Gardeniers, "Stripline probes for nuclear magnetic resonance.," *J. Magn. Reson.*, vol. 189, no. 1, pp. 104–13, 2007.

[54] J. Bart, J. W. G. Janssen, P. J. M. van Bentum, A. P. M. Kentgens, and J. G. E. Gardeniers, "Optimization of stripline-based microfluidic chips for high-resolution NMR.," *J. Magn. Reson.*, vol. 201, no. 2, pp. 175–85, 2009.

[55] X. Zhang, K. Ugurbil, and W. Chen, "Microstrip RF surface coil design for extremely high-field MRI and spectroscopy," *Magn. Reson. Med.*, vol. 46, no. 3, pp. 443–450, 2001.

[56] J. D. Trumbull, I. K. Glasgow, D. J. Beebe, and R. L. Magin, "Integrating microfabricated fluidic systems and NMR spectroscopy.," *IEEE Trans. Biomed. Eng.*, vol. 47, no. 1, pp. 3–7, 2000.

[57] R. R. A. Syms, M. M. Ahmad, I. R. Young, D. J. Gilderdale, and D. J. Collins, "Microengineered needle micro-coils for magnetic resonance spectroscopy," *J. Micromechanics Microengineering*, vol. 16, no. 12, pp. 2755–2764, 2006.

[58] K. Yamauchi, J. Janssen, and A. Kentgens, "Implementing solenoid microcoils for wide-line solid-state NMR," *J. Magn. Reson.*, vol. 167, no. 1, pp. 87–96, 2004.

[59] P. Styles, N. Soffe, C. Scott, D. Crag, F. Row, D. White, and P. White, "A high-resolution NMR probe in which the coil and preamplifier are cooled with liquid helium," *J. Magn. Reson.*, vol. 60, no. 3, pp. 397–404, 1984.

[60] D. L. Olson, T. L. Peck, A. G. Webb, R. L. Magin, and J. V. Sweedler, "High-Resolution Microcoil 1H-NMR for Mass-Limited, Nanoliter-Volume Samples," *Science (80-.).*, vol. 270, no. 5244, pp. 1967–1970, 1995.

[61] C. Massin, F. Vincent, A. Homsy, K. Ehrmann, G. Boero, P.-a. Besse, A. Daridon, E. Verpoorte, N. de Rooij, and R. Popovic, "Planar microcoil-based microfluidic NMR probes," *J. Magn. Reson.*, vol. 164, no. 2, pp. 242–255, 2003.

[62] L. Ciobanu, D. A. Seeber, and C. H. Pennington, "3D MR microscopy with resolution 3.7 l m by 3.3 l m by 3.3 l m," *J. Magn. Reson.*, vol. 158, no. 1-2, pp. 178–182, 2002.

[63] H. Wensink, F. Benito-Lopez, D. C. Hermes, W. Verboom, H. J. G. E. Gardeniers, D. N. Reinhoudt, and A. van den Berg, "Measuring reaction kinetics in a lab-on-a-chip by microcoil NMR," *Lab Chip*, vol. 5, no. 3, p. 280, 2005.

[64] K. Ehrmann, M. Gersbach, P. Pascoal, F. Vincent, C. Massin, D. Stamou, P.-A. Besse, H. Vogel, and R. S. Popovic, "Sample patterning on NMR surface microcoils.," *J. Magn. Reson.*, vol. 178, no. 1, pp. 96–105, 2006.

[65] O. G. Gruschke, N. Baxan, L. Clad, K. Kratt, D. von Elverfeldt, A. Peter, J. Hennig, V. Badilita, U. Wallrabe, and J. G. Korvink, "Lab on a chip phased-array MR multi-platform analysis system.," *Lab Chip*, vol. 12, no. 3, pp. 495–502, 2012.

[66] L. Renaud, M. Armenean, L. Berry, P. Kleimann, P. Morin, M. Pitaval, J. O'Brien, M. Brunet, and H. Saint-Jalmes, "Implantable planar rf microcoils for NMR microspectroscopy," *Sensors Actuators A Phys.*, vol. 99, no. 3, pp. 244–248, 2002.

[67] A. G. Goloshevsky, J. H. Walton, M. V. Shutov, J. S. de Ropp, S. D. Collins, and M. J. McCarthy, "Development of low field nuclear magnetic resonance microcoils," *Rev. Sci. Instrum.*, vol. 76, no. 2, p. 024101, 2005.

[68] Y. Maguire, I. L. Chuang, S. Zhang, and N. Gershenfeld, "Ultra-small-sample molecular structure detection using microslot waveguide nuclear spin resonance.," *Proc. Natl. Acad. Sci. U. S. A.*, vol. 104, no. 22, pp. 9198–203, 2007.

[69] D. A. Seeber, R. L. Cooper, L. Ciobanu, and C. H. Pennington, "Design and testing of high sensitivity microreceiver coil apparatus for nuclear magnetic resonance and imaging," *Rev. Sci. Instrum.*, vol. 72, no. 4, p. 2171, 2001.

[70] H. G. Krojanski, J. Lambert, Y. Gerikalan, D. Suter, and R. Hergenröder, "Microslot NMR probe for metabolomics studies.," *Anal. Chem.*, vol. 80, no. 22, pp. 8668–72, 2008.

[71] S. Terry, J. Jerman, and J. Angell, "A gas chromatographic air analyzer fabricated on a silicon wafer," *IEEE Trans. Electron Devices*, vol. 26, no. 12, pp. 1880–1886, 1979.

[72] A. Manz, N. Graber, and H. Widmer, "Miniaturized total chemical analysis systems: A novel concept for chemical sensing," *Sensors Actuators B Chem.*, vol. 1, no. 1-6, pp. 244–248, 1990.

[73] M. A. Northrup, M. T. Ching, R. M. White, and R. T. Watson, "DNA amplification with a microfabricated reaction chamber," in *Transducers*, vol. 93, pp. 924–926, 1993.

[74] L. Bousse, R. McReynolds, G. Kirk, T. Dawes, P. Lam, W. Bemiss, and J. Parce, "Micromachined multichannel systems for the measurement of cellular metabolism," *Sensors Actuators B Chem.*, vol. 20, no. 2-3, pp. 145–150, 1994.

[75] D. Sobek, A. Young, M. Gray, and S. Senturia, "A microfabricated flow chamber for optical measurements in fluids," in *Proc. IEEE Micro Electro Mech. Syst.*, pp. 219–224, IEEE, 1993.

[76] M. J. Madou, *Fundamentals of microfabrication: the science of miniaturization*. CRC press, 2002.

[77] P. Rai-Choudhury, *Handbook of microlithography, micromachining, and microfabrication: microlithography*, vol. 1. Iet, 1997.

[78] Y. Zhang, P. Zuo, and B.-C. Ye, "A low-cost and simple paper-based microfluidic device for simultaneous multiplex determination of different types of chemical contaminants in food," *Biosens. Bioelectron.*, vol. 68, pp. 14–19, 2015.

[79] G. Kotzar, M. Freas, P. Abel, A. Fleischman, S. Roy, C. Zorman, J. M. Moran, and J. Melzak, "Evaluation of MEMS materials of construction for implantable medical devices.," *Biomaterials*, vol. 23, no. 13, pp. 2737–50, 2002.

[80] G. M. Whitesides, "The origins and the future of microfluidics," *Nature*, vol. 442, no. 7101, pp. 368–373, 2006.

[81] D. C. Duffy, J. C. McDonald, O. J. A. Schueller, and G. M. Whitesides, "Rapid prototyping of microfluidic systems in poly (dimethylsiloxane)," *Anal. Chem.*, vol. 70, no. 23, pp. 4974–4984, 1998.

[82] M. K. Chaudhury and G. M. Whitesides, "Direct measurement of interfacial interactions between semispherical lenses and flat sheets of poly (dimethylsiloxane) and their chemical derivatives," *Langmuir*, vol. 7, no. 5, pp. 1013–1025, 1991.

[83] E. Berthier, J. Warrick, H. Yu, and D. J. Beebe, "Managing evaporation for more robust microscale assays Part 1. Volume loss in high throughput assays," *Lab Chip*, vol. 8, no. 6, pp. 852–859, 2008.

[84] M. Ni, W. H. Tong, D. Choudhury, N. A. A. Rahim, C. Iliescu, and H. Yu, "Cell culture on MEMS platforms: a review.," *Int. J. Mol. Sci.*, vol. 10, no. 12, pp. 5411–41, 2009.

[85] S. Ibrahim, D. A. Higgins, and T. Ito, "Direct-Write Multiphoton Photolithography: A Systematic Study of the Etching Behaviors in Various Commercial Polymers," *Langmuir*, vol. 23, no. 24, pp. 12406–12412, 2007.

[86] M. C. Wapler, J. Leupold, I. Dragonu, D. Von Elverfeld, M. Zaitsev, and U. Wallrabe, "Magnetic properties of materials for MR engineering, micro-MR and beyond," *J. Magn. Reson.*, vol. 242, pp. 233–242, 2014.

[87] X. Zhang and A. G. Webb, "Magnetic Resonance Microimaging and Numerical Simulations of Velocity Fields Inside Enlarged Flow Cells Used for Coupled NMR Microseparations," *Anal. Chem.*, vol. 77, no. 5, pp. 1338–1344, 2005.

[88] E. K. Sackmann, A. L. Fulton, and D. J. Beebe, "The present and future role of microfluidics in biomedical research.," *Nature*, vol. 507, no. 7491, pp. 181–9, 2014.

[89] K. Hosokawa and M. Maeda, "A Microfluidic Device for Mixing of Capillary-Driven Liquids," *IEEJ Trans. Sensors Micromachines*, vol. 123, no. 1, pp. 23–24, 2003.

[90] J. Ducrée, S. Haeberle, S. Lutz, S. Pausch, F. von Stetten, and R. Zengerle, "The centrifugal microfluidic Bio-Disk platform," *J. Micromechanics Microengineering*, vol. 17, no. 7, p. S103, 2007.

[91] H. Andersson, W. van der Wijngaart, P. Nilsson, P. Enoksson, and G. Stemme, "A valve-less diffuser micropump for microfluidic analytical systems," *Sensors Actuators B Chem.*, vol. 72, no. 3, pp. 259–265, 2001.

[92] J. Y. Baek, J. Y. Park, J. I. Ju, T. S. Lee, and S. H. Lee, "A pneumatically controllable flexible and polymeric microfluidic valve fabricated via in situ development," *J. Micromechanics Microengineering*, vol. 15, no. 5, pp. 1015–1020, 2005.

[93] D. Eicher and C. A. Merten, "Microfluidic devices for diagnostic applications.," *Expert Rev. Mol. Diagn.*, vol. 11, no. 5, pp. 505–19, 2011.

[94] F. A. Gomez, "The future of microfluidic point-of-care diagnostic devices," *Bioanalysis*, vol. 5, no. 1, pp. 1–3, 2013.

[95] D. English and B. R. Andersen, "Single-step separation of red blood cells, granulocytes and mononuclear leukocytes on discontinuous density gradients of Ficoll-Hypaque," *J. Immunol. Methods*, vol. 5, no. 3, pp. 249–252, 1974.

[96] S. M. Berry, L. N. Strotman, J. D. Kueck, E. T. Alarid, and D. J. Beebe, "Purification of cell subpopulations via immiscible filtration assisted by surface tension (IFAST)," *Biomed. Microdevices*, vol. 13, no. 6, pp. 1033–1042, 2011.

[97] C. D. Chin, T. Laksanasopin, Y. K. Cheung, D. Steinmiller, V. Linder, H. Parsa, J. Wang, H. Moore, R. Rouse, G. Umviligihozo, and Others, "Microfluidics-based diagnostics of infectious diseases in the developing world," *Nat. Med.*, vol. 17, no. 8, pp. 1015–1019, 2011.

[98] D. Huh, B. D. Matthews, A. Mammoto, M. Montoya-Zavala, H. Y. Hsin, and D. E. Ingber, "Reconstituting organ-level lung functions on a chip," *Science (80-.).*, vol. 328, no. 5986, pp. 1662–1668, 2010.

[99] K.-J. Jang and K.-Y. Suh, "A multi-layer microfluidic device for efficient culture and analysis of renal tubular cells," *Lab Chip*, vol. 10, no. 1, pp. 36–42, 2010.

[100] C. Yi, Q. Zhang, C.-W. Li, J. Yang, J. Zhao, and M. Yang, "Optical and electrochemical detection techniques for cell-based microfluidic systems," *Anal. Bioanal. Chem.*, vol. 384, no. 6, pp. 1259–1268, 2006.

[101] B. Huang, H. Wu, D. Bhaya, A. Grossman, S. Granier, B. K. Kobilka, and R. N. Zare, "Counting low-copy number proteins in a single cell.," *Science*, vol. 315, no. 5808, pp. 81–4, 2007.

[102] N. V. Tolan, L. I. Genes, W. Subasinghe, M. Raththagala, and D. M. Spence, "Personalized metabolic assessment of erythrocytes using microfluidic delivery to an array of luminescent wells.," *Anal. Chem.*, vol. 81, no. 8, pp. 3102–8, 2009.

[103] M. Li, J. Xu, M. Romero-Gonzalez, S. A. Banwart, and W. E. Huang, "Single cell Raman spectroscopy for cell sorting and imaging.," *Curr. Opin. Biotechnol.*, vol. 23, no. 1, pp. 56–63, 2012.

[104] Y. Zhu and Q. Fang, "Analytical detection techniques for droplet microfluidics–a review.," *Anal. Chim. Acta*, vol. 787, pp. 24–35, 2013.

[105] C. A. Baker, C. T. Duong, A. Grimley, and M. G. Roper, "Recent advances in microfluidic detection systems.," *Bioanalysis*, vol. 1, no. 5, pp. 967–75, 2009.

[106] Y. Chen and M. D. Barkley, "Toward Understanding Tryptophan Fluorescence in Proteins ," *Biochemistry*, vol. 37, no. 28, pp. 9976–9982, 1998.

[107] S. Weiss, "Fluorescence Spectroscopy of Single Biomolecules," *Science (80-.).*, vol. 283, no. 5408, 1999.

[108] S. Nie and S. R. Emory, "Probing Single Molecules and Single Nanoparticles by Surface-Enhanced Raman Scattering," *Science (80-.).*, vol. 275, no. 5303, 1997.

[109] L. Tong, M. Righini, M. U. Gonzalez, R. Quidant, and M. Käll, "Optical aggregation of metal nanoparticles in a microfluidic channel for surface-enhanced Raman scattering analysis," *Lab Chip*, vol. 9, no. 2, pp. 193–195, 2009.

[110] E. Galopin, M. Beaugeois, B. Pinchemel, J.-C. Camart, M. Bouazaoui, and V. Thomy, "SPR biosensing coupled to a digital microfluidic microstreaming system," *Biosens. Bioelectron.*, vol. 23, no. 5, pp. 746–750, 2007.

[111] A. J. Ibáñez, S. R. Fagerer, A. M. Schmidt, P. L. Urban, K. Jefimovs, P. Geiger, R. Dechant, M. Heinemann, and R. Zenobi, "Mass spectrometry-based metabolomics of single yeast cells.," *Proc. Natl. Acad. Sci. U. S. A.*, vol. 110, no. 22, pp. 8790–4, 2013.

[112] D. E. Warschawski, A. A. Arnold, M. Beaugrand, A. Gravel, É. Chartrand, and I. Marcotte, "Choosing membrane mimetics for NMR structural studies of transmembrane proteins," *Biochim. Biophys. Acta - Biomembr.*, vol. 1808, no. 8, pp. 1957–1974, 2011.

[113] N. Wu, A. Webb, T. L. Peck, and J. V. Sweedler, "Online NMR detection of amino acids and peptides in microbore LC," *Anal. Chem.*, vol. 67, no. 18, pp. 3101–3107, 1995.

[114] G. Schlotterbeck, A. Ross, R. Hochstrasser, H. Senn, T. Kühn, D. Marek, and O. Schett, "High-Resolution Capillary Tube NMR. A Miniaturized 5-μL High-Sensitivity TXI Probe for Mass-Limited Samples, Off-Line LC NMR, and HT NMR," *Anal. Chem.*, vol. 74, no. 17, pp. 4464–4471, 2002.

[115] N. J. C. Bailey and I. R. Marshall, "Development of ultrahigh-throughput NMR spectroscopic analysis utilizing capillary flow NMR technology," *Anal. Chem.*, vol. 77, no. 13, pp. 3947–3953, 2005.

[116] N. Wu, T. L. Peck, A. G. Webb, R. L. Magin, and J. V. Sweedler, "Nanoliter Volume Sample cells for 1H NMR: Application to Online Detection in Capillary Electrophoresis," *J. Am. Chem. Soc.*, vol. 116, no. 17, pp. 7929–7930, 1994.

[117] D. L. Olson, M. E. Lacey, A. G. Webb, and J. V. Sweedler, "Nanoliter-volume 1H NMR detection using periodic stopped-flow capillary electrophoresis," *Anal. Chem.*, vol. 71, no. 15, pp. 3070–3076, 1999.

[118] C. Hilty, E. E. McDonnell, J. Granwehr, K. L. Pierce, S.-I. Han, and A. Pines, "Microfluidic gas-flow profiling using remote-detection NMR.," *Proc. Natl. Acad. Sci. U. S. A.*, vol. 102, no. 42, pp. 14960–3, 2005.

[119] C. Chen, L. Deng, S. Wei, G. A. Nagana Gowda, H. Gu, E. G. Chiorean, M. Abu Zaid, M. L. Harrison, J. F. Pekny, P. J. Loehrer, D. Zhang, M. Zhang, and D. Raftery, "Exploring Metabolic Profile Differences between Colorectal Polyp

Patients and Controls Using Seemingly Unrelated Regression," *J. Proteome Res.*, vol. 14, no. 6, pp. 2492–2499, 2015.

[120] T. Gebregiworgis, H. H. Nielsen, C. Massilamany, A. Gangaplara, J. Reddy, Z. Illes, and R. Powers, "A Urinary Metabolic Signature for Multiple Sclerosis and Neuromyelitis Optica," *J. Proteome Res.*, vol. 15, no. 2, pp. 659–666, 2016.

[121] J. M. Cevallos-Cevallos, J. I. Reyes-De-Corcuera, E. Etxeberria, M. D. Danyluk, and G. E. Rodrick, "Metabolomic analysis in food science: a review," *Trends Food Sci. Technol.*, vol. 20, no. 11, pp. 557–566, 2009.

[122] A. Edison, R. Hall, C. Junot, P. Karp, I. Kurland, R. Mistrik, L. Reed, K. Saito, R. Salek, C. Steinbeck, L. Sumner, and M. Viant, "The Time Is Right to Focus on Model Organism Metabolomes," *Metabolites*, vol. 6, no. 1, p. 8, 2016.

[123] P. Forgue, S. Halouska, M. Werth, K. Xu, S. Harris, and R. Powers, "NMR Metabolic Profiling of Aspergillus n idulans to Monitor Drug and Protein Activity," *J. Proteome Res.*, vol. 5, no. 8, pp. 1916–1923, 2006.

[124] S. Tiziani, Y. Kang, J. S. Choi, W. Roberts, and G. Paternostro, "Metabolomic high-content nuclear magnetic resonance-based drug screening of a kinase inhibitor library," *Nat. Commun.*, vol. 2, p. 545, 2011.

[125] J. L. Markley, R. Brüschweiler, A. S. Edison, H. R. Eghbalnia, R. Powers, D. Raftery, and D. S. Wishart, "The future of NMR-based metabolomics," *Curr. Opin. Biotechnol.*, vol. 43, pp. 34–40, 2017.

[126] S. Maher, F. P. M. Jjunju, and S. Taylor, "Colloquium : 100 years of mass spectrometry: Perspectives and future trends," *Rev. Mod. Phys.*, vol. 87, no. 1, pp. 113–135, 2015.

[127] C. Teague, E. Holmes, E. Maibaum, J. Nicholson, H. Tang, Q. Chan, P. Elliott, and I. Wilson, "Ethyl glucoside in human urine following dietary exposure: detection by 1H NMR spectroscopy as a result of metabonomic screening of humans," *Analyst*, vol. 129, no. 3, p. 259, 2004.

[128] P. Khandelwal, C. E. Beyer, Q. Lin, P. McGonigle, L. E. Schechter, and A. C. Bach, "Nanoprobe NMR spectroscopy and in vivo microdialysis: new analytical

methods to study brain neurochemistry," *J. Neurosci. Methods*, vol. 133, no. 1, pp. 181–189, 2004.

[129] E. W. K. Young and D. J. Beebe, "Fundamentals of microfluidic cell culture in controlled microenvironments.," *Chem. Soc. Rev.*, vol. 39, no. 3, pp. 1036–48, 2010.

[130] H. Becker and U. Heim, "Hot embossing as a method for the fabrication of polymer high aspect ratio structures," *Sensors Actuators A Phys.*, vol. 83, no. 1, pp. 130–135, 2000.

[131] S. Leidich, M. Braun, T. Gessner, and T. Riemer, "Silicon cylinder spiral coil for nuclear magnetic resonance spectroscopy of nanoliter samples," *Concepts Magn. Reson. Part B Magn. Reson. Eng.*, vol. 35B, no. 1, pp. 11–22, 2009.

[132] D. Mager, A. Peter, L. D. Tin, E. Fischer, P. J. Smith, J. Hennig, and J. G. Korvink, "An MRI receiver coil produced by inkjet printing directly on to a flexible substrate.," *IEEE Trans. Med. Imaging*, vol. 29, no. 2, pp. 482–7, 2010.

[133] H. Wensink, F. Benito-Lopez, D. C. Hermes, W. Verboom, H. J. G. E. Gardeniers, D. N. Reinhoudt, and A. van den Berg, "Measuring reaction kinetics in a lab-on-a-chip by microcoil NMR.," *Lab Chip*, vol. 5, no. 3, pp. 280–4, 2005.

[134] C. Massin, G. Boero, F. Vincent, J. Abenhaim, P.-A. Besse, and R. Popovic, "High-Q factor RF planar microcoils for micro-scale NMR spectroscopy," *Sensors Actuators A Phys.*, vol. 97-98, pp. 280–288, 2002.

[135] D. Beebe, J. Trumbull, and I. Glasgow, "Microfluidics and bioanalysis systems: issues and examples," in *Proc. 20th Annu. Int. Conf. IEEE Eng. Med. Biol. Soc. Vol.20 Biomed. Eng. Towar. Year 2000 Beyond (Cat. No.98CH36286)*, vol. 4, pp. 1692–1697, IEEE, 1998.

[136] P. J. M. van Bentum, J. W. G. Janssen, and A. P. M. Kentgens, "Towards nuclear magnetic resonance micro-spectroscopy and micro-imaging.," *Analyst*, vol. 129, no. 9, pp. 793–803, 2004.

[137] J. Bart, A. J. Kolkman, A. J. Oosthoek-de Vries, K. Koch, P. J. Nieuwland, H. J. W. G. Janssen, J. P. J. M. van Bentum, K. A. M. Ampt, F. P. J. T. Rutjes, S. S.

Wijmenga, H. J. G. E. Gardeniers, and A. P. M. Kentgens, "A microfluidic high-resolution NMR flow probe.," *J. Am. Chem. Soc.*, vol. 131, no. 14, pp. 5014–5, 2009.

[138] K. Jasiński, A. Młynarczyk, P. Latta, V. Volotovskyy, W. P. Węglarz, and B. Tomanek, "A volume microstrip RF coil for MRI microscopy.," *Magn. Reson. Imaging*, vol. 30, no. 1, pp. 70–7, 2012.

[139] H. G. Krojanski, J. Lambert, Y. Gerikalan, D. Suter, and R. Hergenröder, "Microslot NMR probe for metabolomics studies.," *Anal. Chem.*, vol. 80, no. 22, pp. 8668–72, 2008.

[140] G. E. Owen, *Introduction to Electromagnetic Theory*. Courier Dover Publications, 2003.

[141] D. M. Pozar, *Microwave Engineering*. Wiley, Hoboken, New Jersey, fourth edi ed., 2012.

[142] A. Yilmaz and M. Utz, "Characterisation of oxygen permeation into a microfluidic device for cell culture by in situ NMR spectroscopy," *Lab Chip*, vol. 16, no. 11, pp. 2079–2085, 2016.

[143] J. A. Aguilar, M. Nilsson, G. Bodenhausen, and G. A. Morris, "Spin echo NMR spectra without J modulation," *Chem. Commun.*, vol. 48, no. 6, pp. 811–813, 2012.

[144] H. Tang, Y. Wang, J. K. Nicholson, and J. C. Lindon, "Use of relaxation-edited one-dimensional and two dimensional nuclear magnetic resonance spectroscopy to improve detection of small metabolites in blood plasma," *Anal. Biochem.*, vol. 325, no. 2, pp. 260–272, 2004.

[145] A. D. Bax, "A spatially selective composite 90 radiofrequency pulse," *J. Magn. Reson.*, vol. 65, no. 1, pp. 142–145, 1985.

[146] D. A. Seeber, R. L. Cooper, L. Ciobanu, and C. H. Pennington, "Design and testing of high sensitivity microreceiver coil apparatus for nuclear magnetic resonance and imaging," *Rev. Sci. Instrum.*, vol. 72, no. 4, p. 2171, 2001.

[147] O. Warburg, "On the Origin of Cancer Cells," *Science (80-.).*, vol. 123, no. 3191, pp. 309–314, 1956.

[148] M. G. Vander Heiden, L. C. Cantley, and C. B. Thompson, "Understanding the Warburg effect: the metabolic requirements of cell proliferation.," *Science*, vol. 324, no. 5930, pp. 1029–33, 2009.

[149] I. A. Lewis, M. E. Campanella, J. L. Markley, and P. S. Low, "Role of band 3 in regulating metabolic flux of red blood cells.," *Proc. Natl. Acad. Sci. U. S. A.*, vol. 106, no. 44, pp. 18515–20, 2009.

[150] M. A. Leontovich, "Approximate boundary conditions for the electromagnetic field on the surface of a good conductor," *Investig. radiowave Propag.*, vol. 2, pp. 5–12, 1948.

[151] S. V. Yuferev and N. Ida, *Surface Impedance Boundary Conditions: A Comprehensive Approach*. CRC Press, 2009.

[152] M. J. D. Powell, "A direct search optimization method that models the objective and constraint functions by linear interpolation," in *Adv. Optim. Numer. Anal.*, pp. 51–67, Springer, 1994.

[153] G. A. Morris, "Sensitivity enhancement in nitrogen-15 NMR: polarization transfer using the INEPT pulse sequence," *J. Am. Chem. Soc.*, vol. 102, no. 1, pp. 428–429, 1980.

[154] V. Belevitch, "Summary of the History of Circuit Theory," *Proc. IRE*, vol. 50, no. 5, pp. 848–855, 1962.

[155] H. Lee, E. Sun, D. Ham, and R. Weissleder, "ChipNMR biosensor for detection and molecular analysis of cells," *Nat. Med.*, vol. 14, no. 8, pp. 869–874, 2008.

[156] Y. Li, T. M. Logan, A. S. Edison, and A. Webb, "Design of small volume HX and triple-resonance probes for improved limits of detection in protein NMR experiments," *J. Magn. Reson.*, vol. 164, no. 1, pp. 128–135, 2003.

[157] R. M. Fratila, M. V. Gomez, S. Sýkora, and A. H. Velders, "Multinuclear nanoliter one-dimensional and two-dimensional NMR spectroscopy with a single non-resonant microcoil," *Nat. Commun.*, vol. 5, 2014.

[158] N. Spengler, J. Höfflin, A. Moazenzadeh, D. Mager, N. MacKinnon, V. Badilita, U. Wallrabe, and J. G. Korvink, "Heteronuclear Micro-Helmholtz Coil Facilitates micrometre-Range Spatial and Sub-Hz Spectral Resolution NMR of nL-Volume Samples on Customisable Microfluidic Chips," *PLoS One*, vol. 11, no. 1, p. e0146384, 2016.

[159] A. Bax, R. H. Griffey, and B. L. Hawkins, "Correlation of proton and nitrogen-15 chemical shifts by multiple quantum NMR," *J. Magn. Reson.*, vol. 55, no. 2, pp. 301–315, 1983.

[160] N. Trbovic, S. Smirnov, F. Zhang, and R. Brüschweiler, "Covariance NMR spectroscopy by singular value decomposition.," *J. Magn. Reson.*, vol. 171, no. 2, pp. 277–83, 2004.

[161] V. H. Pomin, "Unravelling Glycobiology by NMR Spectroscopy," in *Glycosylation*, ch. 4, pp. 63–98, InTech, 2012.

[162] P. Rossi, G. V. T. Swapna, Y. J. Huang, J. M. Aramini, C. Anklin, K. Conover, K. Hamilton, R. Xiao, T. B. Acton, A. Ertekin, J. K. Everett, and G. T. Montelione, "A microscale protein NMR sample screening pipeline," *J. Biomol. NMR*, vol. 46, pp. 11–22, jan 2010.

[163] R. Zenobi, "Single-cell metabolomics: analytical and biological perspectives.," *Science*, vol. 342, no. 6163, p. 1243259, 2013.

[164] S. Meier, P. R. Jensen, M. Karlsson, and M. H. Lerche, "Hyperpolarized NMR probes for biological assays.," *Sensors (Basel).*, vol. 14, no. 1, pp. 1576–97, 2014.